NASA
TP
2127
c.1

NASA
Technical
Paper
2127

June 1983

TECH LIBRARY KAFB, NM
0067651

Effects of Flow Separation and Cove Leakage on Pressure and Heat-Transfer Distributions Along a Wing-Cove-Elevon Configuration at Mach 6.9

William D. Deveikis

LOAN COPY: RETURN TO
AFWL TECHNICAL LIBRARY
KIRTLAND AFB, N.M.

NASA

25th Anniversary
1958-1983

TECH LIBRARY KAFB, NM

0067651

NASA Technical Paper 2127

1983

Effects of Flow Separation and Cove Leakage on Pressure and Heat-Transfer Distributions Along a Wing-Cove-Elevon Configuration at Mach 6.9

William D. Deveikis
Langley Research Center
Hampton, Virginia

National Aeronautics
and Space Administration

**Scientific and Technical
Information Branch**

SUMMARY

An experimental aerodynamic-heating investigation was conducted at an average free-stream Mach number of 6.9 to determine effects of boundary-layer flow separation on the aerothermal environment in a simulated wing-elevon cove. The model used was a full-scale heat-sink representation of a section on the windward surface of the Space Shuttle orbiter at the wing-elevon juncture. A ramp was attached to the elevon to provide the flow deflection angles required for boundary-layer flow separation. External and internal pressure and cold-wall heating-rate distributions were obtained for quasi-laminar separation, transitional separation, turbulent separation, and attached flow. Test variables were cove seal leak area (0, 13, 50, and 100 percent of the cove entrance area), ramp angle (15°, 25°, 30°, and 35°), and free-stream unit Reynolds number (0.35×10^6, 1.00×10^6, and 1.38×10^6 per foot). Wing angle of attack was 5° (flow compression); average total temperature for all tests was 3360°R, and wall-to-total-temperature ratio for the external flow was about 0.17. Free-stream dynamic pressure ranged from 2 to 9 psi. The cove entrance was located 4 ft downstream from the leading edge of the test apparatus. Cove span was 41.25 in., and cove width where walls were parallel was 0.5 in.

Cove environment was most severe for transitional and turbulent separation, as evidenced by (1) cove pressures that matched or exceeded separated-flow wing pressures up to 3.6 times the attached-flow wing pressure, (2) cove seal differential-pressure loading that was equivalent to separated-flow wing pressure for leaks up to 50 percent, (3) heating rates in the cove and at the elevon bulkhead behind the seal that at least equaled turbulent separated-flow wing heating rates up to 7.3 times laminar attached-flow values, and (4) stream equilibrium temperatures in the cove and at the bulkhead that were 66 percent and 36 percent of total temperature, respectively, at maximum leakage. For quasi-laminar separation, cove pressures matched separated-flow wing pressures, which were up to 20 percent greater than attached-flow values; cove heating rates decreased from separated-flow wing values at the cove entrance, which were as much as one order of magnitude less than for transitional or turbulent separation. For transitional and turbulent separation, increasing the amount of cove leakage progressively increased heating rates in the cove to values that exceeded the turbulent heating rates on the wing. However, when the boundary-layer suction effect of the leaking cove was sufficient to reduce the extent of separation significantly, a further increase in cove leakage reduced cove heating rates to those for laminar attached flow. Where the cove walls were parallel, calculated heating-rate distributions obtained from a mathematical model that assumes laminar developing channel flow agreed with experimentally obtained distributions within root-mean-square differences that varied between 11 and 36 percent for leak areas of 50 and 100 percent.

INTRODUCTION

Ingestion of hot boundary-layer gas into the spanwise clearance, or cove, between the wing and control surfaces is an important factor that must be considered in the design of shuttle-type winged reentry vehicles. On the current Space Shuttle orbiter, ingestion is impeded by means of a spring-loaded polyimide rub seal located near the elevon hinge axis. Otherwise, as illustrated in figure 1, differential pressure between the windward and leeward surfaces would drive part of the boundary layer through the cove where it would contact the interior aluminum load-bearing structure which is not thermally protected. The severity of reentry heating on the wing near the cove entrance was demonstrated on the second flight of the Space Shuttle (STS-2) by steady-state temperatures of approximately 2100°R for several hundred seconds. Those temperatures, recorded by onboard development flight instrumentation (DFI), occurred at approximately 60 and 95 percent of the span near the outboard ends of both elevons (see orbiter sketch in fig. 1). Moreover, during the first flight (STS-1), telemetry data, transmitted after peak reentry heating, indicated a wall temperature descending from 2100°R in the cove (triangle on cross-sectional sketch in fig. 1) at 90 percent of the span (ref. 1). The DFI and telemetry data were sensed by thermocouples within the thermal protection system (TPS) tiles in thermal contact with the surface coating. Certainly, in event of a cove seal failure, exposure to that level of heating would be disastrous for the interior aluminum elevon structure. Indeed, STS-1 postflight inspection revealed thermally damaged insulation in the cove that required replacement by a material capable of withstanding higher temperatures.

Concern over cove heating problems anticipated prior to STS-1 led to experimental aerodynamic-heating investigations at the Langley Research Center to define the nature of cove flow with emphasis on thermal response of an unsealed cove. For this work, a full-scale heat-sink representation of a section on the windward surface of the Space Shuttle orbiter at the wing-elevon juncture was exposed to the hypersonic aerothermal environment produced in the Langley 8-Foot High-Temperature Tunnel. The initial investigation (ref. 2) focused on effects of turbulent attached flow. Its results described a fairly tolerable cove heating environment at Mach 6.9 regardless of leak size, but suggested that convective heating in the cove may increase with time. However, pressures and cold-wall heating rates significantly increased in the cove and at the elevon bulkhead behind the seal when the turbulent boundary layer was forced to separate ahead of the cove entrance. These increases resulted from ingestion of more fluid mass than was available when flow was attached. Although wing flow separation from the windward surface is not anticipated on Shuttle flights, it was of interest to explore its effects further and to form a data base for future analytical work on cove-flow definition. Consequently, the present investigation was initiated to define cove response to flow separation as a function of cove seal leak area, flow deflection angle, and free-stream unit Reynolds number. The bulk of the investigation was conducted for separation of an initially attached laminar boundary layer, although a few tests were also conducted to induce separation of an initially attached turbulent boundary layer. For these tests, flow was deflected at angles sufficient to force separation by means of a ramp mounted on the elevon of the existing model.

Pressure and cold-wall heating-rate distributions were obtained along the wing, cove, and ramp surfaces at a wing pitch of 5° (flow compression) and ramp deflections of 15°, 25°, 30°, and 35° for cove seal leak areas of 0, 13, 50, and 100 percent of the cove entrance area (20.625 in^2). Stream equilibrium temperature distributions were also obtained in the cove and in front of the elevon bulkhead. Free-stream unit Reynolds numbers were nominally 0.35×10^6, 1.00×10^6, and 1.38×10^6 per foot. Average free-stream Mach number for all tests was 6.9, and average total temperature for all tests was 3360°R. Wall-to-total-temperature ratio was about 0.17, and free-stream dynamic pressure ranged from 2 to 9 psi. The effects of external flow conditions, ramp angle, free-stream unit Reynolds number, and cove seal leak area on pressures and cold-wall heating rates in the cove are discussed. Cove data are also compared with values calculated from a heat-transfer relationship based on a mathematical model from reference 3 that assumes laminar developing channel flow.

SYMBOLS

A_e	area of cove entrance, 20.625 in^2
A_l	area of cove seal leak, in^2
c_p	specific heat of combustion-products test medium at constant pressure
D_h	hydraulic diameter, based on cove cross section where walls are parallel, 0.50 in.
g	gravitational constant, 32.2 ft/sec^2
h	local aerodynamic heat-transfer coefficient, Btu/ft^2-sec-°R
k	thermal conductivity of combustion-products test medium, Btu/ft-sec-°R
k_w	thermal conductivity of model wall material, Btu/ft-sec-°R
L	cove length (inset, fig. 24), in.
M	Mach number
$\dot{m}$	mass-flow rate, lbm/sec
N_{St}	Stanton number, $\frac{h}{\rho v c_p}$
N_{Nu}	Nusselt number, $\frac{hx}{k}$
p	static pressure, psia
$\bar{p}$	average cove pressure (p_{15} through p_{22}, table I), psia
Δp	differential pressure ($p_{22} - p_{44}$, table I), psi
N_{Pr}	Prandtl number, $\frac{c_p \mu}{k}$
q	dynamic pressure, psi
$\dot{q}$	heat-transfer rate per unit area, Btu/ft^2-sec
R	perfect gas constant
N_{Re}	Reynolds number
r	cove radius, 6.50 in.
s	surface distance referenced from a location on wing (table I), in.
s'	surface distance referenced from a location on elevon leading edge (table I), in.

T	temperature, $^{\circ}$R
t	time, sec
v	velocity, ft/sec
x	surface distance in the cove referenced from cove entrance (inset, fig. 23), in.
α	wing angle of attack in compression direction, deg
γ	ratio of specific heats of combustion-products test medium
δ	flow deflection angle relative to wing surface (ramp plus elevon deflection, fig. 4), deg
μ	absolute viscosity of combustion-products test medium
ρ	mass density of combustion-products test medium, lbm/ft^3
ρ_w	mass density of model wall material, lbm/ft^3
τ	model wall thickness, in.

Superscript:

$*$	*conditions at Eckert's reference temperature*

Subscripts:

aw	adiabatic wall
c	cove
g	gas
ℓ	local free-stream conditions just outside boundary layer
ref	reference location on wing (table I)
t	total condition in combustor
tot	total condition in cove (table IV)
w	model wall
a,b,c,...,g	bead thermocouple locations (fig. 7)
1,2,3,...,51	orifice and wall thermocouple locations (table I and fig. 3)
∞	undisturbed free-stream conditions

Abbreviations:

Rt	location of reattachment
S	location of flow separation
Tr	location of boundary-layer transition

MODEL, FACILITY, AND TESTS

Model

External configuration.- The model for the present investigation is shown installed in a large sting-mounted test bed in figure 2. Except for external modifications that were made to satisfy test requirements to provide (1) laminar flow over the wing and (2) flow deflection angles that would force flow separation off the wing, the apparatus is essentially the same as that used in the investigation of cove heating reported in reference 2. Laminar flow was maintained by using a blunted leading-edge piece and a smooth nickel wing plate that replaced a surface formerly covered with ceramic tiles. The range of available flow deflection angles was extended by mounting a nickel rotatable ramp atop the existing rotatable elevon. Aerodynamic fences that extended from the leading edge were used to contain the flow over the wing and ramp surfaces.

Model assembly.- Internal components of the assembled model are illustrated in figure 3. These consisted of a wing-cove housing, a rub plate, a seal, and an elevon with ramp, placed within a large opening in the test bed. They are the same components used in the investigation reported in reference 2. As in that investigation, the elevon sidewalls were hinged to the aerodynamic fences to allow elevon rotation. Elevon deflection was varied using a dual air motor drive system located inside the test bed. The sidewalls of the elevon and wing-cove housing and the side edges of the wing and ramp plates were sealed against the fences. Thus, flow along the wing surface was allowed to ingress only at the cove entrance, and the flow along the curved leading edge of the elevon and up the ramp could not leak into the cavity behind the cove seal to influence internal pressure distribution. Flow that was admitted into the cove by a leaking seal vented to low-pressure regions at the base of the elevon and ramp as illustrated by the cross-sectional view in figure 4. During tests at zero elevon deflection, the internal flow vented through a gap between the ramp and closure plate at the base of the ramp and past a gap between the trailing edge of the elevon and the test bed.

As indicated in figure 4, the test bed was approximately 118 in. long, 55.4 in. wide, and 12 in. deep. The leading-edge piece was machined from solid copper and was blunted to a radius of 0.38 in. (fig. 4(a)). The choice of leading-edge radius was guided by results, reported in reference 4, from calibration tests of a flat plate mounted in this test bed. Those results indicated that laminar flow could be maintained to the cove entrance with a leading-edge radius of that size at a nominal free-stream Mach number of 7 and nominal free-stream unit Reynolds numbers from 0.4×10^6 to 1.5×10^6 per foot. The cove entrance was located 47.75 in. from the leading edge and was unswept with respect to the longitudinal axis of the test bed and, hence, to the tunnel stream (fig. 4(d)). Cove span between fences was 41.25 in., and ramp length was 12 in. The short ramp length precluded tunnel flow breakdown at high ramp angles, but the closure plate (figs. 3 and 4(a)) behind the ramp shielded instrumentation under the ramp from base heating. The fences extended from the leading-edge piece to the base of the elevon and to a maximum height above the test surface of 11 in. (fig. 4(a)). Flow disturbance over the test surfaces from the fences was minimized by means of a 30° bevel on the outboard surface of each fence (fig. 4(b)) to allow formation of an attached shock wave away from the wing surface.

Wing surface fabrication and installation.- The wing plate was fabricated from 0.25-in.-thick nickel 201 finished to a surface roughness of 125 μin., rms. Besides providing surface smoothness, nickel external test surfaces offered thermal and structural advantages in the hypersonic aerothermal environment of the test facility as well as convenience for installing surface instrumentation. A semicylindrical nickel rod with radius of 0.25 in. welded to the downstream edge of the wing plate duplicated the rounded lip at the cove entrance used in the investigation reported in reference 2. Upstream of this rounded lip, there was a 0.25-in.-thick airspace between the wing plate and test bed. Thus, direct contact between the wing plate and test bed was avoided. These details are shown as an insert in figure 4(c). The airspace vented at the juncture of the leading-edge piece and the wing plate to preclude trapping atmospheric pressure under the plate during tunnel startup.

The wing plate was bolted to the test bed and wing-cove housing at 41 threaded attachment fittings that were welded to its back surface. The fittings were distributed in a manner that cleared the streamwise centerline for instrumentation by 4 in. One attachment near the centerline and close to the cove entrance was anchored, whereas all other attachments floated to allow in-plane thermal growth both laterally and upstream. The heavy copper leading-edge piece offered no resistance to upstream movement of the wing plate because it, too, was bolted to the back surface of the wing plate; a tongue-and-groove arrangement between the leading-edge piece and test bed, shown simplified in figures 3 and 4(a), allowed the leading-edge piece and wing plate to move freely as a unit. As indicated in figure 4(d), except for a spanwise butt joint between the leading-edge piece and wing plate, the wing surface was continuous from the leading edge to the cove entrance. Gap width and surface flushness across the joint were held within a tolerance of ±0.002 in. to minimize flow disturbance there. Streamwise surface waviness of the wing plate varied within ±0.005 in. along the centerline. However, as viewed from downstream, there was a surface depression of 0.030 in. both in the upstream right quadrant and in the downstream left quadrant.

Ramp fabrication and installation.- Like the wing plate, the ramp surface was fabricated from 0.25-in.-thick nickel 201 and was finished to a surface roughness of 125 μin., rms. A 0.56-in.-diameter nickel rod welded to the upstream edge of the ramp formed a hinge that mated with a concave surface in the downstream edge of a curved nickel plate on the leading edge of the elevon. This detail can be seen in the cross-sectional views in figure 5. The ramp plate was fastened to a steel support framework of streamwise stiffeners using flat-head machine screws through the ramp plate, but the heat-transfer path between these two components was interrupted by using high-temperature insulating tape under the ramp. The downstream end of the ramp assembly was supported by six turnbuckles that were fastened to the elevon as shown in figure 5(a). By adjusting the turnbuckles, the ramp angle relative to the elevon could be varied from 15° to 30°. When the desired ramp angle was set, the turnbuckles were locked, and the hinged end was also locked to the curved plate on the elevon by using machine screws at four places. Maximum deflection of the elevon alone was approximately 19° relative to the wing surface.

Internal configuration.- Dimensionally, the wing, cove, and elevon arrangement shown in figure 5 approximated that of the Space Shuttle orbiter. The wing-cove wall, the elevon leading-edge surface, and the rub surface were concentric about the elevon hinge axis at radii of 6.50 in., 6.00 in., and 3.38 in., respectively (fig. 5(b)). Thus, the concave wing-cove wall and the convex elevon wall formed a 0.5-in.-wide curved channel whose length varied with elevon deflection. The cove flow path then turned sharply toward the seal, and in that region, the channel width varied. The method of sealing the cove shown in figure 5(a) was based on an early Shuttle orbiter design wherein the seal was flex-hinge supported from the elevon and wiped against the cylindrical rub surface. The rub surface was a machined stainless-steel plate and represented the rub tube shown at the orbiter elevon hinge axis in figure 1. The seal used in the present model was a 0.375-in.-thick machined cast-iron bar. Its contact with the rub surface for zero leak was set by adjusting 10 compression screws distributed along the seal (fig. 5(a)). Full-span leaks up to 0.5 in. high were set by removing shims under the rub plate, as illustrated in figure 6. Leak gap height was maintained by means of thin spacers placed at 1/3-span intervals.

Instrumentation.- There were 93 number 30-gage wire stainless-steel sheathed chromel-alumel thermocouples and 58 pressure orifices distributed throughout the model. Most sensors were distributed on or near the centerline, as indicated in figure 7. Most thermocouples on the wing and ramp surfaces were on the centerline, but five were placed along each of two parallel lines 12.3 in. from the centerline, as shown in figure 3. Wing thermocouples were never closer than 4 in. to attachment fittings, and ramp thermocouples were 1.3 in. from streamwise stiffeners on the ramp support framework. Corresponding wing and ramp pressure orifices were located approximately 1 in. outboard of each line of thermocouples. In the cove, wall thermocouples and pressure orifices were spaced at 10° intervals where channel walls were parallel. Wall thermocouples and pressure orifices were also distributed spanwise in the cove, on the rub surface, and along the elevon bulkhead downstream from the seal (see table I). The sensors on the bulkhead were located to receive the pressure and heating from impingement of cove flow past the leaking seal. A pitot pressure probe was placed ahead of the cove seal near location e shown in figure 7. Other pressure orifices were located under the elevon and ramp and at the base of the elevon, ramp, and test bed. Six unshielded beaded thermocouples, 0.033 in. in diameter, were distributed along the centerline of the cove channel 0.25 in. from the wing cove wall (locations a through f in fig. 7), and five were distributed spanwise along the bulkhead 0.06 in. from the surface (location g in fig. 7). These thermocouples were intended only to indicate cove stream total temperature response to test conditions. Miniature probes for accurate measurements of total temperature in the cove stream were not available for the present tests.

For wing and ramp wall temperature measurements, thermocouple wires were individually spot-welded to the back surface of the 0.25-in.-thick nickel plate. In the aluminum cove wall, thermocouple wires were individually spot-welded to the back face of 0.030-in.-thick stainless-steel discs 0.56 in. in diameter that were bonded with silicone rubber (RTV 560) to counterbored holes in the cove wall. Thus, the silicone rubber interrupted the heat conduction path between the disc and cove wall. In the rub plate, thermocouple wires were individually spot-welded to the back face of 0.030-in.-thick sections at the end of holes 0.5 in. in diameter bored from the back surface of the rub plate. At the bulkhead, which consisted of a 0.030-in.-thick stainless-steel sheet fastened to the elevon structure (fig. 5(a)), thermocouple wires were individually spot-welded to its back surface. The wall thermocouples provided data from which cold-wall heating rates were evaluated. Pressures were obtained from the output of strain-gage transducers mounted inside the various model components and connected to 0.060-in.-inside-diameter stainless-steel orifice tubing less than 2 ft. in length for quick response. Table I lists surface distances from the leading edge of the wing or the ramp to centerline surface instrumentation.

Facility

The tests were conducted in the Langley 8-Foot High-Temperature Tunnel. This facility, schematically illustrated in figure 8, is a hypersonic blowdown wind tunnel that operates at a nominal Mach number of 7, at dynamic pressures between 2 and 10 psi, and at total temperatures between 2500°R and 3600°R for free-stream unit Reynolds numbers between 0.3×10^6 and 3.0×10^6 per foot. The test medium is the combustion products of methane and air, which are produced in a high-pressure combustor, expanded through an axisymmetric contoured nozzle, 8 ft in diameter at its exit, and diffused and pumped from the test section to the atmosphere by means of a single-stage annular air ejector. In the test section, the stream is a free jet 14 ft long with a uniform test core approximately 4 ft in diameter. During tunnel startup, models are stored in the pod below the test stream until the desired hypersonic flow conditions are established; the model is then inserted rapidly into the stream by means of a hydraulically actuated elevator and is withdrawn prior to termination of tunnel flow. In the present tests, the test bed reached the stream centerline 1 sec after entering the stream. More detailed information on this facility is reported in reference 5.

Tests

During the present investigation, the untripped blunt leading edge was used in 32 tests, and the sharp leading edge with a boundary-layer trip was used in 1 test. The tests were conducted according to the schedule and test conditions listed in table II. All tests were conducted with the wing surface pitched to an angle of attack of 5° (flow compression) and with the model at ambient temperature prior to insertion into the stream. After insertion, the model remained on the tunnel stream centerline less than 20 sec. Full-span cove seal leaks of 0, 13, 50, and 100 percent of cove entrance area (20.625 in^2) were investigated at the leak gap heights indicated in figure 6 for ramp angles δ of 25°, 30°, and 35° relative to the wing surface. For these tests, the elevon (see fig. 4 for definition of ramp and elevon) was deflected 10°; thus, the cove channel configuration remained constant as ramp angle varied, and sensors at station 20 aligned with those at station 26 (table I). The 13-percent leak was also tested at a ramp angle δ of 15°, at which the elevon deflection angle was zero. Therefore, the cove channel configuration at $\delta = 15^\circ$ differed from that at the other ramp angles, and sensors at station 19 aligned with those at station 26 (table I). The ramp angles for this investigation were not intended to simulate a flight condition but only to ensure that the boundary layer would separate. These model configurations were tested at average free-stream unit Reynolds numbers of 0.35×10^6 and 1.00×10^6 per foot. The last five tests using the blunt leading edge (table II) were conducted for selected leak gaps and ramp angles at a free-stream unit Reynolds number of 1.38×10^6 per foot. Average free-stream dynamic pressures corresponding to the three Reynolds numbers were 2.72, 6.21, and 8.88 psi. Average free-stream Mach number from all tests was 6.9. Based on flat-plate calibration results for a blunt leading edge in reference 4, nominal local Mach number just outside the boundary layer on the wing at the cove entrance was 2.85. Average total temperature from all tests was 3360°R. These free-stream conditions simulated true pressures and aerodynamic heating at altitudes between 87 000 and 120 000 feet at $M_\infty = 6.9$. The test using the sharp leading edge (test 33, table II) was conducted for a sealed cove and ramp angle of $\delta = 35^\circ$ at a free-stream unit Reynolds number of 1.40×10^6. Local Mach number on the wing at the cove entrance was 6.1 for that test.

Data Reduction and Analysis

Data reduction.- Outputs from pressure transducers and thermocouples were recorded on magnetic tape by means of an analog-to-digital data recording system at a rate of 20 samples per second. All data were reduced to engineering quantities at the Langley Central Digital Data Recording Subsystem. Free-stream conditions in the tunnel test section were determined from reference measurements in the combustor (fig. 8) by using results from tunnel stream survey tests such as those presented in reference 4. Computed quantities reported herein are based on the thermal, transport, and flow properties of the combustion-products test medium as reported in reference 6 for an average ratio of specific heats for all tests of 1.38. All tabulated and plotted pressure and heating-rate data herein are normalized with respect to wing surface reference conditions for laminar attached flow nearest the cove entrance (station 14, table I). For tests that resulted in separated flow, the reference pressure was taken from tests in which the flow remained attached at nearly the same free-stream unit Reynolds number. The reference heating rate was calculated from laminar flow theory (to be discussed) at station 14 and was based on the reference pressure. Pressure and heating-rate distributions on the wing, on the ramp, and in the cove were interpreted by comparing them with calculated distributions for attached laminar and turbulent flows.

Data presented herein from the beaded thermocouples in the cove are uncorrected for errors from effects of velocity, thermal conduction, and thermal radiation. Such corrections were not applied because they were considered insufficient to merit application. For example, measured steady-state temperature of the thermocouple beads was within 2 percent of the estimated adiabatic-wall temperature based on a maximum cove stream Mach number of 0.88 as determined from the ratio of measured cove static to total pressure. Correction for thermal conduction along the thermocouple wires was not applied because the exposed wires and the bead were both heated by the cove flow. Therefore, the thermal gradient between bead and wires was very small. Corrections for effects of thermal radiation decreased from about 10 percent at the cove entrance to about 3 percent near the seal. When these corrections were applied, they did not significantly influence the agreement between predicted cove heating rates and measured values; thus, they were disregarded.

Calculated wing and ramp pressures.- Wing and ramp pressures were calculated using oblique-shock relations from inviscid-flow theory for wedge flow (ref. 7) with real-gas effects of the combustion-products test medium taken into account. The calculations were made for a flat plate at an angle of attack of 5° with a downstream compression ramp. For calculations of wing pressure, the conditions used upstream of the leading-edge shock wave were the free-stream values given in table II. For calculations of ramp pressure, the conditions used upstream of the shock at the juncture of the wing and ramp were the reference Mach number (table II) and the measured pressure on the wing for attached flow at station 14 (table I). The reference Mach number corresponds to conditions outside the entropy layer which results from the normal-shock losses associated with the blunt leading edge.

Experimental cold-wall heating rates.- Cold-wall heating rates were determined from thermocouple data using the thin-wall assumption. This assumption was justified for the nickel wing and ramp plates because the high thermal conductivity of the material compensated for their relatively large thickness of 0.25 in.: $h\tau/k_w << 0.01$ which is characteristic of thermally thin walls. Moreover, transient heat-conduction calculations indicated an error of only 1 percent between front and back surfaces after 1 sec of exposure to laminar and turbulent heating. The estimated error due to lateral conduction for a local spanwise step increase in heating rate of 20 percent was 2.5 percent after 1 sec of exposure. The 20-percent step increase corresponds roughly to the rate of increase per unit length encountered on the model wing surface during transition to turbulent flow. Transient heat-conduction calculations for the stainless-steel discs in the thick aluminum cove wall showed that the heat loss to the surroundings was negligible within the first second of aerodynamic exposure. Consequently, heat-transfer data presented herein were evaluated when the model had been on the tunnel stream centerline for 1 sec and were determined from the one-dimensional heat-balance equation,

$$\dot{q} = \rho_w c_p \tau \frac{dT_w}{dt} \tag{1}$$

Calculated cold-wall heating rates for the wing and ramp.- Cold-wall heating-rate distributions for attached wing and ramp flow were calculated for both laminar and turbulent boundary layers from the relation,

$$\dot{q} = N_{St,\ell}^{*}(\rho v c_p)_{\ell}^{*}(T_{aw} - T_w) \tag{2}$$

where for a laminar boundary layer,

$$N_{St,\ell}^{*} = 0.322\left(N_{Pr,\ell}^{*}\right)^{-2/3}\left(N_{Re,\ell}^{*}\right)^{-1/2} \tag{3}$$

and for a turbulent boundary layer,

$$N_{St,\ell}^{*} = 0.0296\left(N_{Pr,\ell}^{*}\right)^{-2/3}\left(N_{Re,\ell}^{*}\right)^{-1/5} \tag{4}$$

These relations are based on Eckert's reference temperature (ref. 8),

$$T^{*} = T_{\infty} + 0.50(T_w - T_{\infty}) + 0.22(T_{aw} - T_{\infty})$$

and are described in reference 9. For these calculations, wing pressure was assumed constant at the reference pressure, and the local temperature was based on a local Mach number determined from flat-plate calibration results reported in reference 4 for a blunt leading edge. Laminar and turbulent cold-wall heating rates on the ramp were calculated by using the calculated ramp pressure described earlier. Experiment agreed better with calculated ramp values that were based on a virtual origin at the leading edge of the wing rather than at the leading edge of the ramp.

Calculated cold-wall heating rates in the cove.- Calculated cold-wall heating rates were determined for the unsealed cove by applying the one-dimensional mathematical model presented in reference 3. The model is based on the assumption that the flow ingested by the cove is laminar developing channel flow. The computational procedure requires cove mass-flow rate and gas temperature at the cove entrance as input. For the present calculations, mass-flow rates through the cove were determined by using measured cove pressures and the cove gas temperature at the beaded thermocouple just upstream of the leak (location f in fig. 7) in the orifice-flow relations,

$$\dot{m} = 0.578 p_c A_l \left(\frac{\gamma g}{RT_g}\right)^{1/2} \qquad \text{(for sonic conditions at the leak)} \qquad (5)$$

and

$$\dot{m} = 0.6 A_l \left(\frac{2 p_c g \, \Delta p}{RT_g}\right)^{1/2} \qquad \text{(for subsonic conditions at the leak)} \qquad (6)$$

where the constant, 0.6, is the coefficient of discharge for a rectangular orifice (see Marks' Handbook for Mechanical Engineers). Cove mass-flow rates so obtained were applied iteratively to obtain the gas temperature at the cove entrance. Cove Reynolds numbers were then calculated from the relation,

$$N_{Re,c} = \frac{\dot{m} D_h}{A_c \mu_c g} \qquad (7)$$

where $A_c = A_e$, since the cove width is constant. Equation (7) was substituted into the following equation, from reference 3, to evaluate cove Nusselt numbers as

$$N_{Nu,x} = N_{Nu,\infty} + \frac{0.036 \dfrac{(N_{Re} N_{Pr})_c}{x/D_h}}{1 + 0.0011 \dfrac{(N_{Re} N_{Pr})_c}{x/D_h}} \qquad (8)$$

As reported in reference 3, the parameter $N_{Nu,\infty}$ is the Nusselt number for fully developed flow between uniformly heated parallel walls and, from reference 9, has a constant value of 8.23. The cove Nusselt numbers were then used to calculate cold-wall heating rates in the cove from the relation,

$$\dot{q} = h_x (T_g - T_w)$$

where

$$h_x = N_{Nu,x}\left(\frac{k_g}{D_h}\right)$$

Results from this procedure and their correlation with experiment are discussed in subsequent sections.

Oil-flow patterns.- Oil-flow patterns were used as an aid for interpreting pressure and heating-rate distributions on the wing and ramp to determine occurrence of flow separation. Prior to each test, a pattern of dots was distributed over the wing, ramp, and inboard surface of each fence using a mixture of oil and lampblack. After each test, the resulting oil-flow patterns were photographed. Typical examples of attached and separated flows indicated by this technique are shown in figure 9, and typical spanwise distributions of pressures and cold-wall heating rates on the wing and ramp are presented in figure 10.

The photographs in figures 9(a) and 9(b) show attached-flow patterns taken from test 24 (table II) for $\delta = 25^\circ$ and $A_l/A_e = 0.50$. In these photographs, the oil streaks trace parallel surface streamlines over the entire wing surface and along the fence up to an oblique oil accumulation line (fig. 9(b)) associated with the deflected ramp. These patterns and the relatively uniform spanwise distributions of attached-flow data of figure 10(a) indicate that the surface flow was two-dimensional. The presence of oil on the surface did not affect the data. Downstream of the oil accumulation line on the fence (fig. 9(b)), the flow direction appears more parallel to that line than to the ramp. The flow pattern in that region is identical to those shown in references 10 and 11 for a swept wing and deflected ramp between adjacent surfaces. According to those references, pressure and thermal loads increase behind the oil accumulation line, and the area of disturbed flow in that region is larger than anticipated from inviscid-flow analyses.

The photographs in figures 9(c) and 9(d) show separated-flow patterns taken from test 15 (table II) for $\delta = 35^\circ$ and $A_l/A_e = 0.13$. In figure 9(c), parallel surface streamlines in the flow direction indicate that flow was attached over approximately one-third of the distance to the cove entrance. Over the remainder of the wing plate, the pattern describes a large reverse-flow region (tails pointing upstream) within which the surface flow circulates in counterrotating directions off the longitudinal centerline; in that region, the boundary layer has separated, and flow within the separated-flow region is three-dimensional. This type of oil-flow pattern was observed in approximately 50 percent of the tests in which separated flow was encountered and is affected by the distance between aerodynamic fences (see refs. 12 and 13). For the present investigation, it was not possible to vary the spacing of the fences to ensure two-dimensional separated flow. However, in practical situations, as in the case of a deflected elevon between a fuselage and tip fin reported in references 10 and 11, three-dimensional flow separation is a real-world phenomenon that can be expected even for small elevon deflections. In figure 9(d), the oil-flow pattern on the fence clearly depicts the recirculating flow under the separated boundary layer across the cove entrance. For this situation, the spanwise distributions of pressures and heating rates over the wing remained relatively uniform (fig. 10(b)), but on the ramp, off-centerline data were higher than centerline values with increasing disparity toward the trailing edge. The centerline data are considered free of extraneous effects. Many oil-flow patterns clearly defined the location of flow separation from the wing as in figure 9(c), however, the spacing and flow of oil dots resulted in a bandwidth of uncertainty in its location of as much as 4 in. (s/r = ±0.3). On the ramp, the determination of flow reattachment was largely speculative. Ramp oil-flow patterns were generally two-dimensional as in figure 9(c), and indications of reverse flow were difficult to detect. Usually, reattachment was taken at the upstream end of long streaks on the ramp. However, inasmuch as the trailing edge of the ramp was first to enter the stream during model insertion, the oil dots on the ramp were disturbed before the flow field over the entire test surface had completely established itself.

RESULTS AND DISCUSSION

Typical External Flow Characteristics

Classification.- Pressures, temperatures, and cold-wall heating rates in the cove are influenced by flow conditions just outside the cove entrance. These external conditions, in turn, are interrelated with cove leak area, ramp angle, and free-stream unit Reynolds number. Therefore, before discussing results pertaining to conditions in the cove, characteristics of the external flow conditions to which the cove was exposed are described. As illustrated in figure 11, a separated boundary layer turns in the compression direction. Consequently, downstream of separation, the flow decelerates, pressure increases, and all the fluid mass between the separating streamline and the dividing streamline enters the cove. For attached flow, pressure at the cove entrance is less than for separated flow, and only a small portion of the boundary layer adjacent to the surface is ingested. For the range of ramp angle, cove seal leak gap, and free-stream conditions of the present investigation, four basic classes of flow were encountered on the wing, as determined from pressure and heating-rate distributions:

1. Laminar and transitional attached flow

2. Quasi-laminar separated flow

3. Transitional separated flow (start of transition downstream of separation)

4. Turbulent separated flow (start of transition upstream of separation)

The three classes of separated flow are based on conventions that were defined by Chapman et al. (ref. 14) from pressure distributions and schlieren photographs and that are well documented (refs. 15 through 21). However, the designation "quasi-laminar separated flow" denotes a departure from the Chapman classification of "purely laminar separated flow." It is coined here to distinguish the shapes of its pressure and heating-rate distributions from the other two classes of separated flow. The rationale for that designation is explained subsequently. The four basic types of flow are described in figure 12 by typical centerline pressure and heating-rate distributions obtained along the wing and ramp from tests listed in table II. Approximate locations of separation from the wing, reattachment to the ramp, and boundary-layer transition are indicated on each plot. These locations were determined either from oil-flow patterns or from distinguishing features of the data distributions. The test data are accompanied by curves calculated from laminar- and turbulent-flow theories for attached flow.

Laminar and transitional attached flow.- The external conditions given by the attached laminar boundary layer are the baseline with which all separated-flow conditions herein are compared. A typical example of pressure and cold-wall heating-rate distributions for laminar attached flow obtained at $N_{Re,\infty} = 0.35 \times 10^6$ per foot is shown in figure 12(a). Wing pressures are essentially uniform up to the cove entrance, and wing heating rates follow the calculated curve for laminar flow. Ramp pressures rise steeply to the inviscid-flow value, and ramp heating rates rise toward the level given by turbulent theory in a manner characteristic of boundary-layer transition. At higher unit Reynolds numbers, the flow over the wing encountered boundary-layer transition. In those instances, the pressure distributions resembled that of figure 12(a), but the heating rates on the wing increased above the laminar level downstream of transition.

Quasi-laminar separated flow.- When a laminar boundary layer separates ahead of a deflected surface, wing pressures rise and heating rates fall from equivalent attached-flow values as in figure 12(b). The location of the deviation of wing pressure and heating rate from attached-flow values identifies the beginning of the shock-wave—boundary-layer interaction induced by the ramp (see fig. 11). Under the separated laminar boundary layer, pressures rise toward a constant plateau level that extends across the cove entrance and up the ramp for a short distance (to the first orifice in this example). For this test, the separated-flow wing pressure at the cove entrance exceeds the attached-flow reference pressure by nearly 20 percent. Inasmuch as there were no oil-flow data for this test, the location of flow separation, labeled "S," was determined from the convention (refs. 17 and 22) that assumes flow separation to occur where the local pressure increases by one-half of the pressure rise to the plateau pressure. On the ramp, pressures rise sharply where the flow reattachment compression fan begins interacting with the separated boundary layer (see fig. 11). The beginning of this interaction is also indicated by a vertical line labeled "Rt." Correspondingly, separated-flow wing heating rates continually fall below attached-flow values and then rise sharply on the ramp toward a constant value near the turbulent level in a manner characteristic of boundary-layer transition.

In this example, the plateau pressure near the cove entrance extends across the cove entrance to the ramp, and so the shape of the pressure distribution conforms to the Chapman convention for "pure laminar" separation (ref. 14). However, the corresponding heating-rate distribution shows a minimum value on the wing just upstream of the cove entrance and, hence, suggests the presence of transition in the separated boundary layer. Obviously, this result violates that convention. Consequently, the type of flow characterized by the distributions in figure 12(b) is designated "quasi-laminar separated flow" for the purpose of this report.

Transitional separated flow.- If the ramp angle is increased for the same cove seal leak area and free-stream unit Reynolds number, the extent of flow separation can increase sufficiently to allow the separated laminar boundary layer to undergo transition to turbulent flow ahead of the cove entrance as in figure 12(c). In reference 14, the designation "transitional" is given to separated flow that is laminar at separation and undergoes transition before reattachment. In this example, the ramp angle was increased from 15° to 30°, and the deviation of wing pressures and heating rates from attached-flow values occurred close to the upstream end of the nickel wing plate. The resulting pressure and heating-rate distributions are characteristic of the situation where transition occurs downstream of separation and ends upstream of reattachment (refs. 14 and 18). Hence, in figure 12(c), wing pressures rise toward a plateau typical of laminar separation (see arrow) followed by another rise extending to the cove entrance. According to references 13 and 14, the pressure rise above the plateau is associated with boundary-layer transition. The plateau to which the pressure appears to be reaching is higher than that in the example of figure 12(b) and is consistent with a documented effect of increasing ramp angle (ref. 21). For this class of separated flow, the wing pressure at the cove entrance is nearly 3 times the attached-flow reference value, and this level extends up the ramp approximately one-fourth of its length (to the second ramp orifice) before rising sharply.

Correspondingly, the wing heating rates fall below laminar attached-flow values, then rise during boundary-layer transition, attain turbulent values where the pressure rise toward the plateau is interrupted, and rise again near the cove entrance. The apparent correlation of pressure rise above the plateau pressure with the end of transition, as determined from the heating-rate distribution, was observed many times, but is at variance with observations reported in reference 14. In that reference, Chapman et al. observed that the pressure rise correlated with the location of transition as determined from shadowgraphs. Nevertheless, the pressure rise above the plateau and the extended influence of separated-boundary-layer pressure up the ramp relative to figure 12(b) are responses to changes in the inviscid flow field associated with a thickening transitional separated boundary layer. The trend of rising heating rates observed near the cove entrance may indicate reattachment of the separating streamline (see fig. 11). On the ramp, the heating rates increase linearly (on a semilogarithmic scale), unlike the rounded distribution in figure 12(b), and rise sharply above the turbulent-flow value at the trailing edge. This result may indicate reattachment of the dividing streamline (see fig. 11).

Turbulent separated flow.- When the free-stream unit Reynolds number was increased to 1.00×10^6 per foot for a ramp angle of 25°, the distributions presented in figure 12(d) were obtained. In this instance, the location of boundary-layer transition, as determined from the heating-rate distribution, is upstream of separation, as determined from oil-flow patterns. Consequently, from reference 14 the designation "turbulent" applies. For this class of separated flow, wing pressures rise above attached-flow values without first showing an initial rise toward a plateau as in the examples of figures 12(b) and 12(c). Likewise, wing heating rates rise to turbulent values without first falling below the laminar attached-flow values and, hence, look somewhat like the distribution given by an attached laminar boundary layer that undergoes transition. On the ramp, the data also appear transitional in nature. The free-stream unit Reynolds number at which this type of flow separation occurred is consistent with reference 19.

Summary of separated-flow events.- During the present investigation, flow separation was encountered in all but seven of the tests. The flow-separation events, compiled from pressure and heating-rate data and classified according to the types shown in figure 12, are summarized in table III. At the lowest free-stream unit Reynolds number, flow separation was either quasi-laminar or transitional. At the higher free-stream unit Reynolds numbers, flow separation was turbulent. The data also show that flow separation can be delayed by decreasing ramp angle, by increasing free-stream unit Reynolds number (which implies reducing altitude), and by increasing cove seal leak area. These effects are discussed in detail in subsequent sections.

Pressure and Heating-Rate Distributions

In the following presentation of results, laminar attached-flow conditions at the cove entrance provide the baseline for ensuing discussions of factors that affected the cove environment. Thus, centerline pressures and heating rates from all tests with the blunt leading edge have been normalized by their respective reference laminar attached-flow values near the cove entrance. These normalized values are displayed in tables IV and V and in figures 13, 14, and 15. The figures are sequenced according to increasing free-stream unit Reynolds number, and the plots for each leak gap are grouped by decreasing order of ramp angle. Each plot is labeled according to one of the four classes of wing flow discussed previously. Data from the wing and its concave cove wall and from the curved elevon surface and the ramp are presented separately as continuous surfaces for convenience in observing the relationship between external (open symbols) and internal (filled symbols) flow conditions. Also given are the conditions sensed at discrete locations such as in the cavity just behind the seal, at the bulkhead, and at the base of the ramp and of the elevon. (Refer to table I and fig. 7 for locations of instrumentation.) The data in these figures are accompanied by calculated conditions on the wing and ramp and in the cove.

On the wing, excellent agreement was obtained between experiment and calculated pressures and laminar cold-wall heating rates where flow was attached (for example, figs. 13(c) and 14(c) at $A_l/A_e \geq 0.50$). For transitional and turbulent separated flows, the agreement with calculated turbulent cold-wall heating rates was usually within 30 percent as in figures 13(a), 13(b), 14(a), and 14(b). Consequently, pressures on the ramp always increased with distance, never peaked, and never reached the calculated inviscid-flow pressure; the heating rates always lay between the calculated curves for laminar and turbulent flows. Thus, the ramp boundary layer always appeared to be in transition. These results are attributed to the relatively short length of the ramp, which precluded development of fully attached flow downstream of the reattachment shock-wave—boundary-layer interaction (fig. 11).

In the cove, pressure and heating-rate distributions (figs. 13, 14, and 15) are similar to those reported in reference 2. Cove pressures are essentially equal on opposite walls, are relatively uniform between the cove entrance and the seal, and are linked directly to the pressure just outside the cove entrance. Thus, for attached-flow conditions on the wing, cove pressures are less than the attached-flow wing pressure as a result of flow expansion around the cove lip (see ref. 2 and figs. 13(c) and 14(c) for $A_l/A_e \geq 0.50$). However, for separated-flow conditions on the wing, cove pressures always exceed the attached-flow wing pressure (inviscid-flow value) and match the separated-flow wing pressure at the cove entrance for $A_l/A_e \leq 0.50$. At the same time, heating rates in the cove decrease with distance from the cove entrance and increase with increasing leak area. In most instances, cove heating rates decline from the value on the wing at the cove entrance. Moreover, the plots in figures 13, 14, and 15 show that the highest cove heating rates are generated when cove pressures are high, as in transitional and turbulent separation. Thus, cove heating is driven by the pressure and boundary-layer state at the cove entrance. Although cove heating rates tend to scatter more with distance from the cove entrance, the data for large leak areas consistently show an increase in heating rate at the sharp turn in the cove ($s/r = 9.8$, station 21 in table I). This local increase in heating apparently results from flow turning.

Cold-wall heating rates for the leaking cove calculated from the method of reference 3 predict the trends of the cove data very well. In general, the root-mean-square difference between experimental and calculated distributions varied between 11 and 36 percent for parallel cove walls as indicated in table VI. However, larger differences between data and prediction were obtained at $A_l/A_e = 0.13$ for $N_{Re,\infty} \geq 1.00 \times 10^6$ per foot. The larger difference shown at $\delta = 15^\circ$ may have resulted from using very low measured heating rates and gas temperatures of questionable accuracy. Moreover, differential pressure across the leak may have been artificially reduced by restricted venting of internal flow at zero elevon deflection required for $\delta = 15^{\circ}$. The larger difference shown at $\delta = 25^{\circ}$ may have occurred because the flow was unstable, but no plausible reason could be found for the larger differences shown at $\delta = 30^{\circ}$.

The plots of figure 13(b) at $A_l/A_e = 1.00$ and figure 14(c) at $A_l/A_e = 0.13$ show two types of external flow instability that were encountered in the present test series. For the test shown in figure 13(b) (test 7 in table II), the laminar boundary layer was attached initially and then separated. The test was repeated (test 8 in table II), and the phenomenon occurred again. In those tests, flow separation was transitional. This type of instability was observed by the author during the investigation reported in reference 23 and probably results from an effect of wall temperature. That is, as wall temperature increases, the boundary layer thickens, and, according to reference 24, the upstream and downstream influence of the ramp then increases to allow a significant increase in extent of flow separation. For the test shown in figure 14(c) (test 23 in table II), the flow separation line oscillated between transitional separation and quasi-laminar separation with the result that conditions on the wing and ramp and in the cove pulsated between the extremes shown. According to reference 18, this type of flow instability accompanies transitional flow separation and is a function of ramp location with respect to boundary-layer transition. Inasmuch as these types of instability could not be attributed to wind-tunnel effects, they have been included as valid test results.

Discussions of effects of ramp angle, free-stream unit Reynolds number, and cove leak area on cove pressures and heating rates follow and are based on the data from figures 13, 14, and 15. A brief discussion is also included on sealed-cove results for a turbulent boundary layer. The presentation of results ends with a detailed discussion of calculated stream temperatures, mass-flow rates, and heating rates in the cove as determined from the channel-flow method of reference 3.

Effect of Ramp Angle

Wing.- The effects of ramp angle on external and internal pressures and cold-wall heating rates are presented in figure 16 for each leak area at $N_{Re,\infty} = 0.35 \times 10^{6}$ per foot for ramp angles between 35° and 15°. Conclusions drawn from these results also apply at the higher free-stream unit Reynolds numbers of the present investigation. These plots show that as ramp angle decreases, the extent of flow separation over the wing diminishes, and the location of boundary-layer transition moves downstream. Consequently, pressures in the separated region decrease, but wing heating rates appear relatively insensitive to ramp angle when separated flow becomes turbulent. When the ramp angle provides quasi-laminar separation from the wing as in figure 16(b), the wing heating rates in the separated region are less than laminar attached-flow heating rates. In this example, wing heating rates near the cove entrance are about one-half the theoretical laminar attached-flow values and are about an order of magnitude less than the turbulent heating rates from transitional separation. When ramp angle is decreased sufficiently, the flow over the wing becomes attached as in figures 16(c) and 16(d). The ramp angle at which the flow becomes attached varies according to the amount of leak. Thus, the ramp angle limit for attached flow is less than 15° for $A_l/A_e = 0.13$ (fig. 16(b)) and is greater than 25° for $A_l/A_e \geq 0.50$ (figs. 16(c) and 16(d)).

Ramp.- The plots in figure 16 show that ramp pressures for quasi-laminar and transitional flow separation are considerably less than ramp pressures for attached flow (compare figs. 16(b), 16(c), and 16(d)). For transitional flow separation, pressures on the downstream portion of the ramp increase as ramp angle decreases for each leak area. Although the scale for pressure used in these plots tends to obscure that observation, it can be verified from the data listed in table IV. This effect probably indicates that fully reattached flow had not developed on the ramp. If the ramp length had been sufficient to allow fully reattached flow, ramp pressures would have decreased as ramp angle decreased. A similar effect was observed at $N_{Re,\infty} = 1.00 \times 10^6$ per foot for $A_l/A_e = 0.13$ (table IV). Thus, it appears that the effectiveness of a short control surface can be altered appreciably by flow separation from the wing.

The heating-rate distributions on the ramp for transitional flow separation show no effect that can be ascribed to ramp angle.

Cove.- At high ramp angles, where the separated flow is turbulent at the cove entrance, cove pressures follow the wing pressure at the cove entrance and decrease as ramp angle is decreased. Correspondingly, the level of cove heating also decreases as ramp angle is decreased but only by about 35 percent as, for example, in figure 16(b). When the ramp angle provides quasi-laminar flow separation as in figure 16(b) for $\delta = 15^\circ$, cove pressures exceed the attached-flow wing pressure but are much less than those under transitional separation for higher ramp angles. Consequently, cove heating rates for quasi-laminar separation are at least one order of magnitude less than those for transitional separation. In this instance, the cove heating rates fall from a value on the wing at the cove entrance that is substantially less than the attached-flow value given by laminar theory. Therefore, this class of separated flow produces the lowest heating rates in the cove among the four classes of external flow encountered in the present investigation. When the ramp angle is decreased sufficiently to provide attached flow along the wing as in figures 16(c) and 16(d), flow expands around the rounded cove lip so that the cove pressures are less than wing pressure at the cove entrance. In this instance, cove heating rates fall from the laminar attached-flow value on the wing at the cove entrance. Hence, the level of heating in the upstream portion of the cove is higher than that for quasi-laminar separation.

Effect of Free-Stream Unit Reynolds Number

Typical effects of free-stream unit Reynolds number on external and internal pressures and cold-wall heating rates are presented in figure 17 at maximum leak area and a ramp angle of 30°. These plots show a change in boundary-layer flow characteristics from transitional separation to transitional attached flow for an increase in free-stream unit Reynolds number from 0.35×10^6 to 1.38×10^6 per foot. For the increase from $N_{Re,\infty} = 0.35 \times 10^6$ to 1.00×10^6 per foot, the extent of separation diminished as shown by the downstream movement in the locations of separation and boundary-layer transition. This result is consistent with a documented effect of increasing free-stream unit Reynolds number for transitional separation (ref. 19). For the increase to $N_{Re,\infty} = 1.38 \times 10^6$ per foot, the resulting attached boundary layer experienced the onset of transition without developing fully turbulent flow at the cove entrance as shown by the rising heating rates on the wing. These distributions show that for separated flow that remains turbulent at the cove entrance, increasing the free-stream unit Reynolds number increases pressures and heating rates on the wing, on the ramp, and in the cove. By increasing unit Reynolds number sufficiently, the boundary layer becomes attached with the result that cove heating rates are decreased by more than an order of magnitude relative to those produced under transitional separation.

Effect of Cove Leak Area

Pressures and heating rates.- The effects of cove leak area on external and internal pressures and on cold-wall heating rates are illustrated in order of decreasing ramp angle in figure 18 for a free-stream unit Reynolds number of 0.35×10^6 per foot. Conclusions drawn from these results regarding the cove environment also apply at the higher unit Reynolds numbers of the present investigation.

At ramp angles of 35° and 30° (figs. 18(a) and 18(b)), the external distributions are characteristic of transitional separated flow with separation occurring a considerable distance upstream of the cove entrance. In these examples, separated-flow wing pressure and cold-wall heating rate near the cove entrance exceed attached-flow reference values by factors of about 3 and 5, respectively (and by as much as 3.6 and 7.3, respectively, at the higher unit Reynolds numbers (see tables IV and V)). As indicated, the estimated locations of flow separation and boundary-layer transition do not appear to be significantly affected by the suction effect caused by the leaking cove and show no orderly change with leak area. At $\delta = 35^\circ$, separated-flow wing pressures toward the cove entrance change only slightly with leak area, but at $\delta = 30^\circ$, the suction effect is sufficient to produce a noticeable decrease in those pressures as leak area increases. In the cove, pressures obtained at $\delta = 35^\circ$ and 30° match or exceed separated-flow wing pressure at the cove entrance for A_l/A_e up to 0.50. Hence, the flow direction across the cove entrance either remained unchanged or turned in the compression direction at those leak areas. However, at $A_l/A_e = 1.00$, cove pressures are much less than the separated-flow wing pressure at the cove entrance (but are greater than attached-flow reference pressures) and, therefore, indicate that the flow expanded around the cove lip at the entrance. This effect at maximum leak area also occurred at $N_{Re,\infty} = 1.00 \times 10^6$ per foot as shown in figure 14. When this effect occurred, flow conditions at the leak were subsonic as given by downstream-to-upstream pressure ratios across the seal, $p_{44}/\bar{p} > 0.537$ (see table IV). Thus, the flow process in the cove differs from that at smaller leak areas as indicated by the relatively nonuniform pressure distributions and the sharp local rise in pressure at the turn in the cove path ($s/r = 9.8$, station 21 in table I). This increase and the accompanying increase in heating rates there reflect an exchange of energy as the cove flow decelerates in the turn. Downstream of the seal, as indicated by the filled symbols in figures 18(a) and 18(b), static pressure in the cavity and pressure at the bulkhead (stations 44 and 45, respectively, in table I) increase as leak area increases. At the same time, the cove heating rates near the entrance, near the seal, and, most importantly, at the bulkhead increase to levels that approach and sometimes exceed the turbulent separated-flow heating rates on the wing. Thus, at ramp angles of 35° and 30°, the cove aerothermal environment becomes increasingly severe with increasing leak area.

In contrast to the foregoing, the distributions for the ramp angle of 25° (fig. 18(c)) show that flow separation is transitional only for A_l/A_e up to 0.13. For $A_l/A_e = 0.50$ and 1.00, the distributions are characteristic of laminar attached flow. Consequently, cove pressures are less than attached-flow wing pressures as a result of flow expansion at the cove lip, and cove heating rates decrease from laminar attached-flow values. The decrease in the level of cove heating from that generated by transitional separation at $A_l/A_e = 0.13$ to that for laminar attached flow is as much as an order of magnitude. Moreover, at maximum leak, the cove heating rates (triangles) are less than those for the sealed cove (circles) which had been exposed to transitional separation. Similar results were obtained at this ramp angle for $N_{Re,\infty} = 1.00 \times 10^6$ per foot (fig. 14(c)). Thus, at a ramp angle of 25°, the cove aerothermal environment generated by transitional separation can be relieved by increasing the leak area. In this instance, boundary-layer bleed by suction into the cove was sufficient to prevent both separation and boundary-layer transition. This stabilizing effect of suction on the boundary layer is discussed by Schlichting (ref. 25, pp. 269 and 423).

For quasi-laminar separated flow, as in figure 13(d), the extent of separation is relatively small. Consequently, the suction effect of increasing the leak area would be expected to result in laminar attached flow. In that event, the level of cove heating would be somewhat greater than for quasi-laminar separation because the level of cove heating at the cove entrance would be greater relative to the separated-flow heating there.

Cove and bulkhead pressures.- Details of the cove environment not conveniently discerned in figure 18 are summarized in figure 19. In this figure, normalized pressures, normalized cold-wall heating rates, and temperature ratios from the beaded thermocouples in the cove and at the bulkhead are plotted as a function of leak area ratio for a free-stream unit Reynolds number of 0.35×10^6 per foot. In figure 19(a), data are presented for a ramp angle of 30° to demonstrate effects that occur when the external flow encounters transitional separation at all leak areas. In figure 19(b), data are presented at a ramp angle of 25° to demonstrate the effects that occur when the external flow becomes attached.

In the upper plots of figure 19, average cone pressure between p_{15} and p_{22} (table I, circles), bulkhead pressure (triangles), and differential pressure across the seal (p_{22}-p_{44} in table I, diamonds) are compared with the measured wing pressure nearest the cove entrance (dashes). For transitional separation, the following effects of increasing leak area are observed:

1. Average cove pressure (circles) decreases from values that exceed the separated-flow wing pressure at the cove entrance (dashes) for $A_l/A_e \leq 0.13$ to a value that matches the separated-flow wing pressure at $A_l/A_e = 0.50$ to less than separated-flow wing pressure at $A_l/A_e = 1.00$. In all cases, the average cove pressure exceeds the reference attached-flow wing pressure by at least a factor of 2.

2. Differential pressure across the seal (diamonds) decreases from a level equivalent to the separated-flow wing pressure to free-stream static pressure as A_l/A_e increases from 0 to 1.

3. The pressure at the bulkhead (triangles) increases from a value about equivalent to free-stream static pressure at $A_l/A_e = 0$ to the average cove pressure for $A_l/A_e = 1.00$.

When the external flow becomes attached ($A_l/A_e \geq 0.50$, fig. 19(b)), pressures in the cove (filled circles) and at the bulkhead (filled triangles) are less than the attached-flow reference pressure (dashes), and differential pressure across the seal (filled diamonds) approaches zero.

Cove and bulkhead heating rates.- In the center plots of figure 19, normalized cold-wall heating rates in the cove near the entrance, near the seal, and at the bulkhead are compared with the measured wing heating rate nearest the cove entrance. For transitional separation, the following effects of increasing leak area are observed:

1. The cove heating rate near the entrance (circles, station 15 in table I) increases to the turbulent heating rate on the wing (dashes, $q_{14}/q_{ref} = 4$) for $A_l/A_e \geq 0.50$. It exceeds the reference laminar attached-flow value by at least a factor of 2 for all values of A_l/A_e.

2. The cove heating rate at the seal (diamonds, station 24 in table I) increases to 75 percent of the turbulent heating rate on the wing as A_l/A_e increases to 1.00. It approaches the reference laminar attached-flow value at $A_l/A_e = 0.13$ and exceeds the reference value by about a factor 3 at $A_l/A_e = 1.00$.

3. Bulkhead heating rate (triangles) increases to within two-thirds of the turbulent heating rate on the wing (dashes) as A_l/A_e increases from 0 to 0.50 and is within 90 percent of that value at $A_l/A_e = 1.00$. (At the free-stream unit Reynolds number of 1.00×10^6 per foot, the bulkhead heating rate exceeded the turbulent heating rate on the wing at $A_l/A_e = 1.00$ (see table V).) For $A_l/A_e \geq 0.50$, the bulkhead heating rate exceeds the reference laminar attached-flow value by more than a factor of 3. When the external flow becomes attached ($A_l/A_e \geq 0.50$, fig. 19(b)), cove and bulkhead heating rates (filled symbols) are less than the reference laminar attached-flow value.

Temperatures in the cove stream.- In the lower plots of figure 19, steady-state temperatures given by the beaded thermocouples in the cove stream and near steady-state values at the bulkhead are presented referenced to free-stream total temperature. (Normalized bead temperatures from all tests are listed in table VII.) As with the cove heating rates discussed earlier, the bead temperatures increase with leak area and decrease with distance from the cove entrance. For transitional separation and for $A_l/A_e = 1.00$, the bead temperatures attained 66 percent of total temperature near the entrance, 46 percent near the seal, and 36 percent at the bulkhead. (At the higher free-stream unit Reynolds number, these temperatures were 73, 60, and 50 percent, respectively; see table VII.) It is evident that for transitional (and turbulent) separation, high gas temperatures are generated in the high-pressure environment just outside the cove entrance. Thus, under these separated-flow conditions, more energy is available which supplies more mass flow through the cove as leak area increases and, hence, delivers more heating to the cove walls than under attached-flow conditions.

Since there is no heat loss by radiation in the cove and no conduction at the wall, the bead temperatures shown in figure 19(a) are the maximum values that the structure would experience. These temperatures and corresponding cove heating rates suggest that prolonged exposure to these conditions could be hazardous to unprotected interior load-bearing structures made of aluminum alloy. By contrast, the bead temperatures shown in figure 19(b) for laminar attached flow (filled symbols) are between 30 and 40 percent of total temperature near the entrance, are 20 percent near the seal, and are 15 percent at the bulkhead. Thus the cove environment is considerably less hostile for laminar attached flow than for transitional or turbulent separation.

The cove stream temperatures and cove heating rates presented herein comprise the basic information needed for designing thermal protection of the cove. From the foregoing test results, a viable thermal protection concept for flight at a Mach number of 7 may be a hot structure that would allow cove bleed but would not allow the ingested flow to impinge on the internal structure. For a Shuttle type reentry mission, cove stream temperatures and heating rates would be required over the reentry trajectory to verify the concept.

Turbulent Flow

Results from an attempt to force a turbulent boundary layer to separate are shown in figure 20. The test was conducted with a sealed cove for a wing angle of attack of 5° and ramp angle of 35° at $N_{Re,\infty} = 1.40 \times 10^6$ per foot. For this test, the blunt leading edge was replaced by a sharp leading edge equipped with a boundary-layer trip of 0.094-in.-diameter spheres spaced across the width of the test bed just upstream of the nickel wing plate. As indicated, wing pressures appear uniform, and wing heating rates follow the calculated curve for turbulent flow. Thus, the wing data indicate that the boundary layer was attached. Moreover, in contrast to the results obtained with the blunt leading edge, ramp pressures and heating rates peaked. That observation and the good agreement between experiment and theoretical values, especially with the calculated turbulent heating rates based on virtual origin at the ramp leading edge, indicate fully developed attached flow over most of the ramp. However, pressures in the cove, more than twice the wing pressures, indicate that the flow compressed across the cove entrance. Oil-flow patterns on the fences, shown in figure 21, revealed that the flow just above the wing surface began turning outboard over the cove entrance. In the cove, heating rates decreased from the entrance to the seal by more than two orders of magnitude (fig. 20). Moreover, these heating rates are less than those for the sealed cove obtained at the lower $N_{Re,\infty}$ of 1.00×10^6 per foot for turbulent separation (compare tests 14 and 33, table V). Thus, it appears that turbulent separation generates more thermal loading in the cove than turbulent attached flow. For the small extent of flow separation indicated for this test, a leaking cove would probably cause the flow to expand at the cove entrance.

Calculated Gas Temperatures, Mass-Flow Rates, and Heating Rates in the Cove

The purpose of the following discussion is to demonstrate applicability of the one-dimensional mathematical model of reference 3 to predict the cold-wall heating rates in the cove plotted in figures 13, 14, and 15. Inasmuch as the computational procedure requires a value of the gas temperature at the cove entrance as input, the equilibrium temperatures from the unshielded thermocouples (fig. 7) were used for that purpose. Typical responses of those thermocouples are shown uncorrected for losses from conduction and radiation in figure 22 for $A_l/A_e = 0.13$, 0.50, and 1.00 at $\delta = 30^\circ$ and $N_{Re,\infty} = 0.35 \times 10^6$ per foot (tests 5, 6, and 7, table II). The plots in figures 22(a) and 22(b) show responses to transitional separated flow, and the plots in figure 22(c) show responses to flow that was attached for approximately 9 sec and then abruptly separated. Unsteady variations in bead temperature shown at the cove entrance (location a, inset) follow variations in tunnel free-stream total temperature from probes located in the combustor (fig. 8). The drop in temperature shown at about 8 sec in figure 22(b) reflects an anomalous variation in total temperature that occurred during that test.

Distributions of equilibrium temperatures from the transitional separation data of figures 22(a) and 22(b) and from the attached-flow portion of the data in figure 22(c) are plotted in figure 23. When the equilibrium temperature at the cove entrance (location a, inset; $x/L = 0$) was specified as the entrance gas temperature in the computational procedure of reference 3, the resulting calculated gas-temperature distributions (solid curves) underpredicted the measured values by about 10 percent. By varying the entrance gas-temperature input until the calculated gas temperature near the leak agreed with the measured equilibrium temperature at location f (inset; $x/L = 0.97$), the dashed curves were obtained. Curves obtained in this manner were used in the procedure for obtaining the calculated cove heating rate distributions shown in figures 13, 14, and 15. All calculated curves in figure 23 were contributed by L. Roane Hunt, author of the procedure.

The test data at the cove entrance in figure 23 for $A_l/A_e = 0.13$ and 0.50 (transitional separation) show that the measured equilibrium temperature at the cove entrance increases with increasing leak area. However, the calculated entrance values from the dashed curves do not change with leak area and are nearly 70 percent of total temperature. Calculated entrance gas temperatures for $\delta = 35^{\circ}$ yielded similar results at about 75 percent of total temperature. Thus, the one-dimensional theory of reference 3 seems to suggest that for transitional separation that becomes turbulent at the cove entrance, the entrance gas temperature is independent of leak area. A mathematical model that completely defines the incoming flow field at the cove entrance is required to verify this postulation.

The calculated entrance gas temperatures for the examples shown in figure 23 exceed the measured entrance values for transitional separated flow by up to 19 percent and for laminar attached flow ($A_l/A_e = 1.00$) by about 10 percent. Some of the difference between calculated and measured values obviously results from thermal losses by radiation which, as stated earlier in this report, amounted to about 10 percent at the entrance. The discrepancy may also lay in the choice of origin as the entrance to the cove, inasmuch as a significant gradient in Nusselt number occurs over the entry length (see eq. (8)). Another reason for the discrepancy may be that the thermocouple was unable to sense the true incoming flow temperature where it was located; that is, the bead may have been located within a flow eddy rather than in the incoming flow down the ramp.

Samples of cold-wall heating-rate distributions obtained from the method of reference 3 using entrance gas temperatures given by the dashed curves in figure 23 are presented in figure 24 for tests 5, 6, and 7 (table II). Where the cove walls are parallel (x/L up to 0.6), the root-mean-square difference between experiment and calculated distributions is about 14 percent for tests 5 and 6 (transitional separation) and about 20 percent for test 7 (attached flow). Thus, the one-dimensional mathematical model of reference 3 appears well suited for estimating cold-wall heating rates in an unsealed wing-elevon cove for either separated or attached flow at the cove entrance.

The measured cove gas temperatures at location f in figure 23 were used in orifice-flow relations (eqs. (5) and (6)) to evaluate cove mass-flow rate from every test for $A_l/A_e > 0$. Resulting variations of gas temperature at the entrance and near the leak are plotted as a function of cove mass-flow rate in figure 25 and show very good correlation. These variations show rising cove gas temperatures with increasing mass-flow rate along separate, fairly linear curves for transitional and turbulent separation and for attached flow. As indicated by the curves obtained from the method of least squares (solid lines), the gas temperatures for attached flow rise more slowly with mass flow than those for transitional and turbulent separation.

The data in figure 25(a) show that the gas temperature at the cove entrance increases more slowly with mass flow than those near the leak (fig. 25(b)). The curves obtained from the method of reference 3 (dashed lines) using entrance gas temperatures given by the dashed curves of figure 23 as input suggest that the entrance gas temperature is virtually invariant with cove mass-flow rate.

CONCLUSIONS

The effects of ingesting various amounts of mass from separated and attached boundary layers into a wing-elevon cove were determined as a function of cove leak area and free-stream unit Reynolds number from wind-tunnel tests at an average free-stream Mach number of 6.9. The model used was a 41.25-in.-wide, full-scale, heat-sink representation of a section of the cove region between the wing and elevon on the windward surface of the Space Shuttle orbiter. Tests were conducted in the Langley 8-Foot High-Temperature Tunnel. Cove leakage was controlled by adjusting the height of a gap up to 0.5 in. under a seal located near the elevon hinge line for nominal leak areas of 0, 13, 50, and 100 percent of cove entrance area of 20.625 in^2. The wing surface was pitched 5° (flow compression), and a ramp on top of the elevon provided flow-deflection angles of 15°, 25°, 30°, and 35° downstream of the unswept cove entrance. Pressure and cold-wall heating-rate distributions were obtained on the wing and ramp surfaces and on cove walls. Nominal free-stream unit Reynolds numbers were 0.35×10^6, 1.00×10^6, and 1.38×10^6 per foot, and average total temperature from all tests was 3360°R. Duration of model exposure to the tunnel flow was no more than 20 sec.

At the low free-stream unit Reynolds number and at ramp angles between 35° and 25°, separated flow underwent transition to turbulence at the cove entrance. By holding any two of the three variables (ramp angle, Reynolds number, and leak area) constant while varying the third, flow separation over the wing and ramp was eliminated by decreasing ramp angle, by increasing free-stream unit Reynolds number, or by increasing cove leakage. For a separated region that undergoes transition (i.e., transitional separation) on the wing, pressure and cold-wall heating rate at the cove entrance (for $T_w/T_t \approx 0.17$) can exceed laminar attached-flow values by factors up to 3.6 and 7.3, respectively. For quasi-laminar separated flow on the wing, pressure at the cove entrance exceeds attached-flow pressure, whereas wing cold-wall heating rates decrease from attached-flow values. Consequently, the character of the cove aerothermal environment varies widely according to the flow conditions at the cove entrance. The following conclusions are drawn concerning cove response to these external flow conditions:

1. Cove heating is driven by the pressure and boundary-layer state at the cove entrance.

2. Cove pressures are essentially equal on opposite walls and are relatively uniform regardless of whether wing flow is attached or separated. Cove heating rates decrease with distance from the cove entrance but increase with increasing leak area.

3. At high ramp angles, the separated flow remains turbulent at the cove entrance regardless of leak area ($\delta = 35^\circ$), and increasing cove leakage progressively increases cove heating rates. In this situation, cove pressures exceed or match

separated-flow wing pressure at the cove entrance, and the cove walls and the bulkhead behind the seal become exposed to heating that may exceed separated-flow wing heating rates. At maximum leakage, cove stream temperatures can reach 73 percent of total temperature near the entrance, 60 percent near the seal, and 50 percent at the bulkhead.

4. At lower ramp angles ($\delta \leq 30^{\circ}$), increasing cove leakage can reduce heating in the cove for transitional separation to that for laminar attached flow. In this situation, cove pressures and heating rates are less than attached-flow wing values at the cove entrance, and cove heating rates at maximum leakage can be less than sealed-cove heating rates for separated flow.

5. If the locations of boundary-layer transition and flow separation are close, the flow in the separated region is unsteady. Therefore, the location of separation can oscillate, in which event the cove environment pulsates between the extremes given by transitional separation and either quasi-laminar separation or laminar attached flow.

6. For a leaking cove, the ramp angle limit for attached flow increases as leak area increases.

7. Cove stream temperatures are proportional to cove mass-flow rate and vary along different curves for separated and attached flows for all leak areas and free-stream unit Reynolds numbers.

8. For parallel cove walls, a one-dimensional mathematical model that assumes laminar developing flow can predict cove heating-rate distributions within a range of root-mean-square differences with experiment between 11 and 36 percent using measured cove stream equilibrium temperatures.

9. Present test results indicate that a viable thermal protection concept for flight at a Mach number of 7 may be a hot structure that would allow cove bleed.

Langley Research Center
National Aeronautics and Space Administration
Hampton, VA 23665
April 12, 1983

REFERENCES

1. Dotts, R. L.; Battley, H. H.; Hughes, J. Thomas; and Neuenschwander, W. E.: Space Shuttle Orbiter - Reusable Surface Insulation Subsystem Thermal Performance. AIAA-82-0005, Jan. 1982.

2. Deveikis, William D.; and Bartlett, Whitney: Pressure and Heat-Transfer Distributions in a Simulated Wing-Elevon Cove With Variable Leakage at a Free-Stream Mach Number of 6.9. NASA TM-74095, 1978.

3. Hunt, L. Roane: Aerothermal Analysis of a Wing-Elevon Cove With Variable Leakage. NASA TP-1703, 1980.

4. Deveikis, William D.; and Hunt, L. Roane: Loading and Heating of a Large Flat Plate at Mach 7 in the Langley 8-Foot High-Temperature Structures Tunnel. NASA TN D-7275, 1973.

5. Deveikis, William D.; Bruce, Walter E., Jr.; and Karns, John R.: Techniques for Aerothermal Tests of Large, Flightweight Thermal Protection Panels in a Mach 7 Wind Tunnel. NASA TM X-71983, 1974.

6. Leyhe, E. W.; and Howell, R. R.: Calculation Procedure for Thermodynamic, Transport, and Flow Properties of the Combustion Products of a Hydrocarbon Fuel Mixture Burned in Air With Results for Ethylene-Air and Methane-Air Mixtures. NASA TN D-914, 1962.

7. Ames Research Staff: Equations, Tables, and Charts for Compressible Flow. NACA Rep. 1135, 1953. (Supersedes NACA TN 1428.)

8. Eckert, Ernst R. G.: Survey on Heat Transfer at High Speeds. ARL 189, U.S. Air Force, Dec. 1961. (Available from DTIC as AD 274 109.)

9. Kays, W. M.: Convective Heat and Mass Transfer. McGraw-Hill Book Co., Inc., c.1966.

10. Johnson, Charles B.; and Kaufman, Louis G., II: High Speed Interference Heating Loads and Pressure Distributions Resulting From Elevon Deflections. AIAA Paper 79-0145, Jan. 1979.

11. Kaufman, Louis G., II; and Johnson, Charles B.: Pressure and Thermal Distributions on Wings and Adjacent Surfaces Induced by Elevon Deflections at Mach 6. NASA TP-1356, 1979.

12. Holden, Michael S.: A Study of Flow Separation in Regions of Shock Wave-Boundary Layer Interaction in Hypersonic Flow. AIAA Paper 78-1169, July 1978.

13. Settles, Gary S.; Fitzpatrick, Thomas J.; and Bogdonoff, Seymour M.: A Detailed Study of Attached and Separated Compression Corner Flowfields in High Reynolds Number Supersonic Flow. AIAA Paper 78-1167, July 1978.

14. Chapman, Dean R.; Kuehn, Donald M.; and Larson, Howard K.: Investigation of Separated Flows in Supersonic and Subsonic Streams With Emphasis on the Effect of Transition. NACA Rep. 1356, 1958.

15. Crawford, Davis H.: The Effect of Air Bleed on the Heat Transfer and Pressure Distribution on 30° Conical Flares at a Mach Number of 6.8. NASA TM X-439, 1961.

16. Dearing, J. David; and Hamilton, H. Harris: Heat-Transfer and Pressure Distributions Inside the Hinge-Line Gap of a Wedge-Flap Combination at Mach Number 10.4. NASA TN D-4911, 1968.

17. Hamilton, H. Harris; and Dearing, J. David: Effect of Hinge-Line Bleed on Heat Transfer and Pressure Distribution Over a Wedge-Flap Combination at Mach 10.4. NASA TN D-4686, 1968.

18. Holloway, Paul F.; Sterrett, James R.; and Creekmore, Helen S.: An Investigation of Heat Transfer Within Regions of Separated Flow at a Mach Number of 6.0. NASA TN D-3074, 1965.

19. Johnson, Charles B.: Pressure and Flow-Field Study at Mach Number 8 of Flow Separation on a Flat Plate With Deflected Trailing-Edge Flap. NASA TN D-4308, 1968.

20. Johnson, Charles B.: Heat-Transfer Measurements at Mach 8 on a Flat Plate With Deflected Trailing-Edge Flap With Effects of Transition Included. NASA TN D-5899, 1970.

21. Putnam, Lawrence E.: Investigation of Effects of Ramp Span and Deflection Angle on Laminar Boundary-Layer Separation at Mach 10.03. NASA TN D-2833, 1965.

22. Cooke, J. C.: Separated Supersonic Flow. Tech. Note No. Aero.2879, British R.A.E., Mar. 1963.

23. Deveikis, William D.; and Sawyer, James Wayne: Aerodynamic Characteristics of Tension Shell Shapes at Mach 3.0. NASA TN D-3633, 1966.

24. Needham, D. A.; and Stollery, J. L.: Hypersonic Studies of Incipient Separation and Separated Flows. Separated Flows, Pt. I, AGARD CP No. 4, May 1966, pp. 89-119.

25. Schlichting, Herman (J. Kestin, transl.): Boundary Layer Theory, Fourth ed. McGraw-Hill Book Co., Inc., c.1960.

TABLE I.- LOCATION OF INSTRUMENTATION ON CENTERLINE

[See fig. 7]

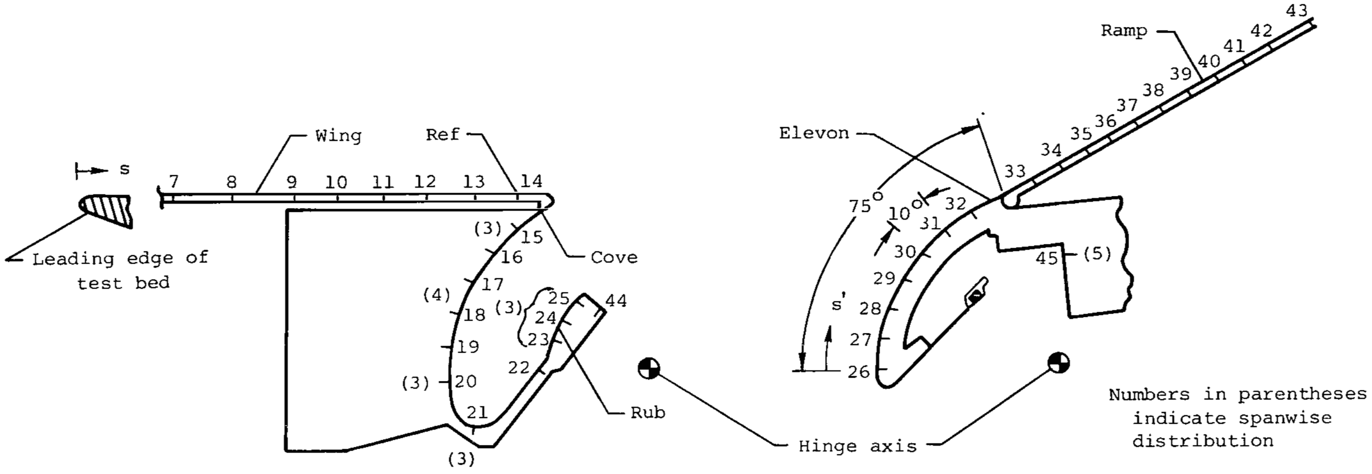

Numbers in parentheses indicate spanwise distribution

Wing, cove, and rub surfaces			Elevon and ramp surfaces		
Orifice and thermocouple	s, in.	Wall thickness, in.	Orifice and thermocouple	s', in.	Wall thickness, in.
1	10.19	0.250	[b]26	0	0.125
2	14.19		[b]27	1.03	
3	18.19		[b]28	2.05	
4	22.19		[b]29	3.07	
5	26.19		[b]30	4.13	
6	30.19		[b]31	5.16	
7	34.19		32	6.15	
8	36.19		33	8.59	.250
9	38.19		[a]34	9.59	
10	40.19		35	10.59	
11	41.69		[a]36	11.59	
12	43.19		37	12.59	
13	44.69		[a]38	13.59	
14 (ref.)	46.19		39	14.59	
15	48.88	.032	[a]40	15.59	
16	50.08		41	16.59	
17	51.31		[a]42	17.59	
18	52.48		43	19.34	
19	53.68				
20	54.88				
21	56.66				
22	59.69				
[a]23	60.61	.030			
24	61.44	.032			
[a]25	62.25	.029			

[a] Thermocouple only.
[b] Orifice only.

TABLE II.- TEST CONDITIONS

Test	Cove leak gap height, in.	A_l, in^2	A_l/A_e	α, deg	δ, deg	T_t, °R	p_∞, psia	q_∞, psi	M_∞	$N_{Re,\infty}$, ft^{-1}	M_{ref}	q_{ref}, psi	T_∞, °R	Leading edge
1	0.063	2.60	0.13	5	35	3375	0.063	2.86	7.09	0.33 × 10^6	6.02	4.12	380	Blunt
2	.250	10.31	.50		35	3400	.064	2.96	7.10	.33	6.05	4.16	380	
3	.500	20.63	1.00		35	3400	.064	2.83	7.11	.33	6.06	4.17	380	
4	0	0	0		30	3500	.065	2.65	7.18	.33	6.18	4.34	385	
5	.063	2.60	.13			3350	.064	2.90	7.06	.33	6.02	4.11	378	
6	.250	10.31	.50			3550	.058	2.18	7.23	.33	6.04	4.15	385	
7	.500	20.63	1.00			3325	.065	3.14	7.00	.32	6.02	4.12	380	
8	.500	20.63	1.00			3340	.066	2.98	7.03	.32	6.03	4.12	380	
9	0	0	0		25	3307	.064	2.15	7.05	.42	6.01	4.10	353	
10	.063	2.60	.13			3325	.066	3.28	6.93	.41	5.94	4.00	372	
11	.250	10.31	.50			3550	.058	2.16	7.23	.33	6.04	4.15	385	
12	.500	20.63	1.00			3500	.061	2.18	7.18	.33	6.06	4.17	385	
13	.063	2.60	.13		15	3275	.065	3.09	6.98	.41	6.01	4.10	375	
14	0	0	0	5	35	3255	0.201	6.22	6.80	1.01 × 10^6	5.98	10.80	397	Blunt
15	.063	2.60	.13			3275	.202	6.15	6.79	1.00	5.92	11.11	400	
16	.250	10.31	.50			3400	.195	6.34	6.90	.93	5.99	11.24	410	
17	.500	20.63	1.00			3410	.192	6.10	6.92	.94	5.99	11.24	406	
18	0	0	0		30	3310	.199	6.36	6.83	1.01	5.84	11.76	400	
19	.063	2.60	.13			3325	.198	6.49	6.83	.91	5.83	11.74	420	
20	.250	10.31	.50			3450	.193	6.31	6.94	.93	5.99	11.47	410	
21	.500	20.63	1.00			3275	.202	5.98	6.78	1.00	5.91	11.08	400	
22	0	0	0		25	3317	.198	6.31	6.84	1.01	5.84	11.78	400	
23	.063	2.60	.13			3550	.189	6.02	7.02	.94	6.03	11.60	415	
24	.250	10.31	.50			3300	.200	6.22	6.83	1.01	5.85	11.79	398	
25	.500	20.63	1.00			3250	.204	6.12	6.78	1.00	5.92	11.12	399	
26	0	0	0		15	3260	.202	6.27	6.81	1.02	5.99	10.87	397	
27	.063	2.60	.13		15	3375	.196	6.14	6.89	1.01	5.91	10.93	405	
28	0.063	2.60	0.13	5	30	3350	0.291	8.67	6.78	1.35 × 10^6	6.01	15.10	418	Blunt
29	.250	10.31	.50		30	3425	.286	9.10	6.83	1.36	6.14	14.34	420	
30	.500	20.63	1.00		30	3350	.290	8.63	6.78	1.35	6.00	15.08	418	
31	0	0	0		25	3254	.294	9.18	6.69	1.43	5.84	15.62	412	
32	.063	2.60	.13		15	3250	.297	8.84	6.69	1.43	5.85	15.70	410	
33	0	0	0	5	35	3264	0.297	9.09	6.70	1.40 × 10^6	5.85	16.38	415	Sharp, tripped

TABLE III.- SUMMARY OF SEPARATED-FLOW EVENTS

$N_{Re,\infty}$, ft^{-1}	Occurrence of separated flow on wing															
	δ = 15°				δ = 25°				δ = 30°				δ = 35°			
	A_l/A_e				A_l/A_e				A_l/A_e				A_l/A_e			
	0	0.13	0.50	1.00	0	0.13	0.50	1.00	0	0.13	0.50	1.00	0	0.13	0.50	1.00
0.35×10^6	▨	╱ L	▨	▨	╱ Tr	╱ Tr			╱ Tr	╱ Tr	╱ Tr	* ╱ Tr	▨	╱ Tr	╱ Tr	╱ Tr
1.00			▨	▨	╱ T	O ╱ T	Tr		╱ T	╱ T	╱ T	╱ T	╱ T	╱ T	╱ T	╱ T
1.38	▨	Tr	▨	▨	╱ T	▨	▨	▨	▨	╱ T	╱ T	Tr	▨	▨	▨	▨

▨ No data

☐ Attached flow

Tr Transitional attached flow

╱ Laminar separation

╱ L Quasi-laminar separation

╱ Tr Transitional separation

╱ T Turbulent separation

* Initially attached flow followed by separation

O Oscillating separation

TABLE IV.- NORMALIZED PRESSURES

Test	A_l/A_e	p_{ref}, psia	Wing														δ, deg	Leading edge
			p_1/p_{ref}	p_2/p_{ref}	p_3/p_{ref}	p_4/p_{ref}	p_5/p_{ref}	p_6/p_{ref}	p_7/p_{ref}	p_8/p_{ref}	p_9/p_{ref}	p_{10}/p_{ref}	p_{11}/p_{ref}	p_{12}/p_{ref}	p_{13}/p_{ref}	p_{14}/p_{ref}		
1	0.13	0.164	0.476	0.467	1.530	1.242	1.883	2.218	2.469	1.418	2.733	2.844	2.896	2.942	3.029	3.046	35	Blunt
2	.50	↓	.905	.709	.907	1.204	2.040	2.022	2.465	2.191	2.787	2.775	2.824	3.112	2.994	3.312	35	↓
3	1.00	↓	1.274	1.447	1.573	1.627	1.882	2.216	2.591	2.699	2.814	2.913	2.937	2.971	3.043	3.070	35	↓
4	0	↓	1.339	1.141	1.201	1.266	1.318	1.713	2.152	2.400	2.645	2.876	2.926	3.109	3.227	3.304	30	↓
5	.13	↓	1.198	1.152	1.290	1.414	1.478	1.633	1.967	2.104	2.290	2.456	2.539	2.625	2.723	2.790	↓	↓
6	.50	↓	1.201	1.095	1.113	1.275	1.384	1.484	1.772	1.796	2.157	2.346	2.456	2.555	2.654	2.727	↓	↓
[a]7	1.00	↓	1.223	1.107	1.072	1.024	1.044	1.001	.983	.961	.989	.991	.993	.972	.989	1.049	↓	↓
7	1.00	↓	1.215	1.100	1.215	1.318	1.402	1.463	1.645	1.775	1.981	2.163	2.281	2.384	2.478	2.547	↓	↓
[a]8	1.00	↓	1.279	1.148	1.090	1.047	1.067	1.015	.987	.983	1.004	1.001	1.006	.986	.989	1.033	↓	↓
8	1.00	↓	1.260	1.148	1.193	1.330	1.412	1.480	1.733	1.917	2.105	2.280	2.404	2.510	2.588	2.653	↓	↓
9	0	↓	.423	1.200	1.176	.499	1.308	1.366	1.420	1.386	1.543	1.751	1.937	2.142	2.006	2.483	25	↓
10	.13	↓	.899	.818	1.079	1.190	1.298	1.356	1.463	1.530	1.743	1.939	2.084	2.212	2.345	2.457	↓	↓
11	.50	↓	1.256	1.118	1.058	1.010	1.022	.974	.965	.918	.978	.970	.969	.939	.946	.978	↓	↓
12	1.00	↓	1.262	1.158	1.104	1.042	1.070	1.029	1.013	.999	1.025	1.023	1.020	.994	.998	1.023	↓	↓
13	.13	↓	1.189	1.075	1.026	.983	.998	.957	.942	.911	1.027	1.082	1.123	1.140	1.176	1.187	15	↓
14	0	0.437	0.991	1.455	1.592	1.652	2.473	2.757	2.937	3.006	3.114	3.218	3.227	3.350	3.383	3.567	35	Blunt
15	.13	.458			1.374	1.864	2.383	2.630	2.845	2.756	3.029	3.107	3.166	3.235	3.305	3.329	↓	↓
16	.50	.452	1.320	1.145	1.285	1.502	2.286	2.659	2.968	2.790	3.189	3.335	3.356	3.422	3.489	3.514	↓	↓
17	1.00	.452	1.233	1.095	1.042	1.037	1.159	1.409	1.874	2.008	2.223	2.371	2.447	2.519	2.572	2.605	↓	↓
18	0	.498	1.154	1.038	.992	1.043	1.223	1.694	2.089	2.212	2.338	2.452	2.521	2.602	2.684	2.740	30	↓
19	.13	.498	1.170	1.052	1.015	1.053	1.228	1.711	2.160	2.149	2.449	2.577	2.651	2.725	2.802	2.859	↓	↓
20	.50	.461	1.273	1.158	1.046	1.101	1.051	1.619	2.059	2.219	2.463	2.643	2.700	2.783	2.854	2.897	↓	↓
21	1.00	.458	1.289	1.175	1.102	1.053	1.164	1.360	1.895	2.061	2.320	2.484	2.582	2.669	2.737	2.783	↓	↓
[b]22	0	.498	1.076	1.152	1.058	.909	1.053	1.134	1.303	1.617	1.883	2.075	2.206	2.406	2.464	2.722	25	↓
[b]23	.13	.461	1.265	1.132	1.074	1.018	1.037	1.049	1.190	1.302	1.576	1.843	2.018	2.164	2.889	2.401	↓	↓
23	.13	.461	1.278	1.147	1.087	1.030	1.043	.980	.976	.950	.978	.979	1.007	1.050	1.116	1.160	↓	↓
24	.50	.498	1.226	1.116	1.072	1.010	1.054	1.004	.910	.996	1.006	1.007	1.015	.991	.990	.996	↓	↓
25	1.00	.458	1.267	1.134	1.090	1.039	1.059	.997	1.004	.987	1.005	1.008	1.013	.987	.989	1.003	↓	↓
26	.13	.437	1.008	1.193	1.130		1.073	1.011	.996	.862	1.021	.961	.983	1.002	1.001	1.196	15	↓
27	.13	.452	1.267	1.133	1.094	1.040	1.063	1.008	1.003	.968	1.009	1.010	1.015	.989	.989	.996	15	↓
28	0.13	0.604	1.352	1.205	1.154	1.182	1.451	2.080	2.531	2.644	2.819	2.956	3.046	3.137	3.222	3.310	30	Blunt
29	.50	.549	1.490	1.299	1.309	1.206	1.378	1.887	2.482	2.530	2.861	2.889	3.054	3.194	3.290	3.364	30	↓
30	1.00	.604	1.316	1.168	1.113	1.054	1.073	1.015	1.006	.957	1.004	1.010	1.016	.984	.993	.998	30	↓
31	0	.662	1.314	1.257	1.105	1.044	1.065	1.078	1.270	1.521	1.773	2.005	2.157	2.336	2.426	2.666	25	↓
32	.13	.663	1.242	1.110	1.075	1.028	1.046	.996	.910	.985	1.004	1.007	1.023	.992	.994	.984	15	↓
33	0	0.737	1.100	0.995	0.981	0.990		0.934		0.836	0.856				0.848	0.937	35	Sharp, tripped

[a] Attached flow.
[b] Oscillating flow separation.

TABLE IV.- Continued

Test	A_l/A_e	p_{ref}, psia	Cove								Rub	$p_{44}/\bar{p}$	Bulkhead	Elevon cavity		Elevon base	Test bed base	δ, deg	p_{tot}/p_{ref}	p_∞/p_{ref}
			p_{15}/p_{ref}	p_{16}/p_{ref}	p_{17}/p_{ref}	p_{18}/p_{ref}	p_{19}/p_{ref}	p_{20}/p_{ref}	p_{21}/p_{ref}	p_{22}/p_{ref}	p_{24}/p_{ref}		p_{45}/p_{ref}	p_{44}/p_{ref}	p_{46}/p_{ref}					
1	0.13	0.164	3.415	3.424	3.426	3.473	3.404	3.456	1.245	3.475	0.474	0.155	0.610	0.537	0.549	0.550	0.305	35	3.480	0.384
2	.50	↓	3.450	3.254	3.354	3.357	3.308	3.280	3.391	3.462	3.082	.267	1.832	.893	.855	.507	.763	35	3.664	.390
3	1.00	↓	2.203	2.130	2.058	2.071	2.081	2.213	2.841	2.270	2.068	.538	2.137	1.132	1.191	1.282	.397	35	3.480	.390
4	0	↓	2.559	3.691	3.675	3.740	3.718	3.743	2.382	3.747	3.862		.611	.425	.397	1.282	.397	30	3.664	.396
5	.13	↓	3.065	3.056	3.085	3.100	3.064	3.112	3.159	3.138	3.052	.139	.611	.441	.488	.733	.317	↓	3.480	.390
6	.50	↓	2.760	2.733	2.725	2.727	2.689	2.761	2.964	2.779	2.419	.316	1.832	.673	.915	.794	3.232	↓	3.480	.354
[a]7	1.00	↓	.735	.715	.699	.704	.704	.739	.851	.752	.707	.825	.611	.606	.610	1.160	.549	↓	.916	.396
7	1.00	↓	1.863	1.810	1.764	1.809	1.801	1.927	2.443	1.952	.715	.616	1.832	1.171	1.280	1.343	.396	↓	2.748	.396
[a]8	1.00	↓	.707	.686	.668	.670	.676	.709	.821	.726	.682		.611	.573	.549	.549	.549	↓	.916	.402
8	1.00	↓	1.903	1.862	1.820	1.860	1.856	1.980	2.510	2.013	1.844	.632	1.832	.688	1.219	1.221	.366	↓	2.748	.402
9	0	↓	2.685	2.751	2.759	2.763	2.361	1.998	1.787	1.568	2.786		.469	.424	.433	.938	.353	25	.463	.390
10	.13	↓	2.734	2.732	2.730	2.744	2.720	2.782	2.814	2.791	2.525	.181	.611	.495	.366	.977	.183	↓	2.442	.402
11	.50	↓	.712	.685	.677	.682	.679	.720	.782	.737	.661	.645	.794	.457	.488	.916	.488	↓	.794	.354
12	1.00	↓	.544	.525	.520	.517	.517	.541	.601	.546	.526	.887	.611	.478	.488	.916	.549	↓	.611	.372
13	.13	↓	1.177	1.152	1.159	1.171	1.148	1.177	1.190	1.182	1.173		1.221	.934	.976	.915	.305	15	1.221	.396
14	0	0.437	3.890	3.986	4.005	3.976	3.998	3.972	4.750	3.632	4.177		0.457	0.432	0.455	1.043	1.653	35	0.460	0.460
15	.13	.458	3.698	3.718	3.716	3.724	3.671	3.719	3.510	3.745	1.986	0.168		.616				↓		.441
16	.50	.452	3.670	3.663	3.633	3.635	3.639	3.659	3.889	3.710	3.294	.278	2.214	1.000	1.106	1.107		↓	3.985	.431
17	1.00	.452	1.814	1.828	1.797	1.841	1.844	2.028	2.720	2.075	1.991	.474	1.882	.929	.901	.700	.288	↓	2.834	.425
18	0	.498	2.912	3.087	3.105	3.117	3.117	3.119	3.008	3.136	3.207		.401	.369	.361	.983	.281	30	3.110	.400
19	.13	.498	3.166	3.182	3.200	3.207	3.207	3.211	3.198	3.225	3.135	.184	.502	.587	.522	.762	1.526	↓	3.170	.398
20	.50	.461	3.008	3.000	2.989	2.993	2.988	3.019	3.214	3.050	2.696	.317	1.951	.966	1.041	1.149	1.627	↓	3.361	.419
21	1.00	.458	1.987	2.056	2.037	2.090	2.097	2.209	2.752	2.292	2.116	.705	2.182	1.481	1.550	1.592	1.637	↓	2.945	.441
22	0	.498	2.673	2.738	2.747	2.750	2.350	1.989	1.778	1.561	2.773		.469	.424	.422	.938	.353	25	3.325	.398
[b]23	.13	.461	2.681	2.677	2.700	2.705	2.695	2.710	2.690	2.725	2.655	.196	.650	.536	.564	.802	1.562	↓	2.710	.406
[b]23	.13	.461	1.208	1.203	1.213	1.217	1.209	1.212	1.153	1.214	1.179	.345	.434	.412	.412	.629	1.562	↓	1.236	.406
24	.50	.498	.609	.601	.603	.604	.601	.610	.612	.606	.553	.716	.502	.553	.452	1.224	1.586	↓	.702	.402
25	1.00	.458	.540	.530	.530	.535	.535	.544	.597	.548	.535	.943	.545	.503	.502	1.134	1.703	↓	.545	.445
26	.13	.437	1.021	1.030	1.033	1.028	1.004	1.040	.821	.790	1.069		.455	.452	.459	.452	.636	15	.436	.462
27	.13	.452	.868	.855	.865	.866	.849	.870	.771	.869	.886		.886	.842	.841	.819	.841	15	.886	.434
28	0.13	0.604	3.647	3.686	3.684	3.679	3.681	3.706	3.702	3.726	3.616	0.178	0.662	0.656	0.646	1.258		30	3.723	0.482
29	.50	.549	3.504	3.519	3.500	3.498	3.484	3.539	3.405	3.568	3.140	.329	2.370	1.138	1.239	1.240		30	3.864	.521
30	1.00	.604	.508	.507	.511	.512	.511	.518	.517	.519	.513	.988	.496	.494	.497	.629		30	.579	.480
31	0	.662	2.591	2.646	2.672	2.633	2.648	2.628	3.516	2.868	2.785		.486	.418	.493	.938	1.356	25	.577	.444
32	.13	.663	.750	.741	.751	.753	.747	.754	.643	.752	.754		.830	.760	.754	.725	2.866	15	.755	.448
33	0	0.737	2.437		2.603	2.531	2.472	2.548	2.528	2.532	2.571		1.034	1.064	1.030	1.341	1.051	35	2.354	0.403

[a] Attached flow.
[b] Oscillating flow separation.

TABLE IV.- Concluded

Test	A_l/A_e	p_{ref}, psia	Elevon curved leading edge							Ramp						Ramp cavity	Ramp base	δ, deg
			p_{26}/p_{ref}	p_{27}/p_{ref}	p_{28}/p_{ref}	p_{29}/p_{ref}	p_{30}/p_{ref}	p_{31}/p_{ref}	p_{32}/p_{ref}	p_{33}/p_{ref}	p_{35}/p_{ref}	p_{37}/p_{ref}	p_{39}/p_{ref}	p_{41}/p_{ref}	p_{43}/p_{ref}			
1	0.13	0.164	3.367	3.437	3.389	3.380	3.385	3.397	3.324	3.194	3.157	3.482	4.213	5.134	6.382	0.550	0.550	35
2	.50		3.318	3.412	3.351	3.359	3.363	3.387	3.401	3.314	2.740	3.862	4.877	6.182	8.314	.855	.794	35
3	1.00		2.015	2.044	2.015	2.000	2.012	2.077	2.573	3.134	3.239	3.737	4.693	5.976	8.017	.916	.916	35
4	0		3.695	3.750	3.686	3.665	3.673	3.657	3.586	3.358	3.594	4.266	5.415	6.936	9.007	.488	.733	30
5	.13		3.073	3.109	3.050	3.054	3.050	3.107	3.035	2.929	2.980	3.465	4.298	5.283	6.409	.550	.666	
6	.50		2.643	2.705	2.666	2.669	2.674	2.703	2.778	2.805	3.073	3.800	4.974	6.485	8.672	.855	.794	
[a]7	1.00		.732	.746	.746	.750	.753	.758	.803	2.188	6.536	11.196	14.049	15.587	16.250	.611	.611	
7	1.00		1.742	1.746	1.711	1.694	1.686	1.734	2.182	2.641	3.079	3.886	5.171	6.712	8.861	1.160	.794	
[a]8	1.00		.697	.713	.703	.712	.716	.720	.769	2.336	6.728	11.408	14.299	15.815	16.561	.550	.550	
8	1.00		1.781	1.790	1.747	1.728	1.720	1.767	2.244	2.806	3.169	3.974	5.240	6.822	9.118	1.099	.794	
9	0		1.649	2.914	2.726	2.799	2.693	2.730	2.568	2.601	2.884	3.800	4.929	6.151	7.152	.425		25
10	.13		2.729	2.758	2.708	2.713	2.718	2.767	2.714	2.563	2.921	3.670	4.675	5.819	7.111	.550	.550	
11	.50		.723	.749	.737	.736	.748	.749	.761	1.839	4.462	6.826	9.186	10.828	11.952	.468	1.404	
12	1.00		.543	.547	.550	.552	.555	.550	.542	2.465	4.701	7.319	9.613	11.094	12.152	.468	1.465	
13	.13		1.166	1.193	1.139	1.177	1.177	1.192	1.199	1.257	1.883	2.689	3.526	4.346	5.259	.916	.794	15
14	0	0.437	3.599	3.919	3.880	3.971	3.879	3.909	3.674	3.685	3.671	3.910	4.537	5.493	6.489	0.425		35
15	.13	.458	3.668	3.734	3.698	3.694	3.703	3.699	3.610	3.422	3.380	3.697	4.325	5.253	6.377			
16	.50	.452	3.552	3.636	3.603	3.599	3.608	3.641	3.676	3.594	3.707	4.192	5.217	6.792	9.442	.930	0.841	
17	1.00	.452	1.725	1.746	1.718	1.669	1.652	1.702	2.609	2.721	3.121	3.844	5.043	6.714	9.140	.686	.598	
18	0	.498	3.107	3.138	3.101	3.080	3.070	3.063	2.980	2.829	2.991	3.369	4.043	4.938	5.797	.441	.602	30
19	.13	.498	3.180	3.221	3.191	3.185	3.178	3.182	3.108	2.915	3.114	3.587	4.405	5.522	6.967	.582	.642	
20	.50	.461	2.917	2.972	2.945	2.938	2.937	2.969	3.017	2.943	3.253	3.899	4.993	6.489	8.678	.997	.781	
21	1.00	.458	2.032	2.051	2.007	1.941	1.902	1.863	2.277	2.867	3.389	4.258	5.710	7.672	10.791	1.462	.873	
22	0	.498	2.894	3.185	2.963	3.014	2.973	2.975	2.816	2.851	3.075	3.751	4.695	5.785	6.710	.425		25
[b]23	.13	.461	2.664	2.694	2.683	2.662	2.660	2.680	2.642	2.483	2.972	3.786	4.962	6.349	7.968	.585	.932	
[b]23	.13	.461	1.199	1.197	1.205	1.184	1.187	1.213	1.202	1.347	4.117	6.760	9.774	11.572	12.581	.455	.976	
24	.50	.498	.595	.604	.601	.600	.596	.596	.602	3.116	5.210	8.517	10.724	11.455	11.810	.452	1.344	
25	1.00	.458	.538	.544	.541	.541	.534	.534	.530	3.050	5.410	8.851	10.707	11.441	11.703	.502	1.440	
26	.13	.437	.826	1.007	1.013	1.019	1.023	1.025	1.002	1.799	2.920	3.865	4.950	5.857	6.644	.457		15
27	.13	.452	.867	.857	.864	.847	.854	.873	.866	2.134	2.882	2.811	4.372	5.153	5.850	.841	.819	15
28	0.13	0.604	3.675	3.714	3.685	3.678	3.675	3.660	3.576	3.408	3.622	3.732	5.055	6.281	7.885	0.645	0.728	30
29	.50	.549	3.438	3.498	3.468	3.461	3.469	3.479	3.502	3.493	3.805	4.137	5.765	7.415	9.836	1.240	.911	30
30	1.00	.604	.512	.513	.512	.510	.507	.505	.479	3.651	5.656	8.518		11.115		.496	.612	30
31	0	.662	2.988	3.113	2.949	3.002	2.940	2.940	2.785	2.827	3.140	3.799	4.829	6.040	7.196	.475		25
32	.13	.663	.753	.757	.749	.732	.752	.754	.736	2.283	2.875	2.800	4.435	5.150	5.716	.755	.725	15
33	0	0.737	0.418	2.768	2.577	2.639	2.607	2.594	2.470	2.973	20.599	19.414	18.626	18.268	16.626	0.777	0.064	35

[a] Attached flow.
[b] Oscillating flow separation.

TABLE V.- NORMALIZED COLD-WALL HEATING RATES

Test	A_l/A_e	$\dot{q}_{ref}$, Btu/ft^2-sec	Wing														δ, deg
			$\dot{q}_1/\dot{q}_{ref}$	$\dot{q}_2/\dot{q}_{ref}$	$\dot{q}_3/\dot{q}_{ref}$	$\dot{q}_4/\dot{q}_{ref}$	$\dot{q}_5/\dot{q}_{ref}$	$\dot{q}_6/\dot{q}_{ref}$	$\dot{q}_7/\dot{q}_{ref}$	$\dot{q}_8/\dot{q}_{ref}$	$\dot{q}_9/\dot{q}_{ref}$	$\dot{q}_{10}/\dot{q}_{ref}$	$\dot{q}_{11}/\dot{q}_{ref}$	$\dot{q}_{12}/\dot{q}_{ref}$	$\dot{q}_{13}/\dot{q}_{ref}$	$\dot{q}_{14}/\dot{q}_{ref}$	
1	0.13	1.008	1.785	0.992	1.289	2.182	2.975	3.173	3.074	3.074	3.074	3.173	3.173	3.272	3.669	4.165	35
2	.50	1.032	1.938	1.357	1.066	2.423	3.682	3.876	3.682	3.682	3.682	3.682	3.779	4.118	4.215	5.039	35
3	1.00	1.032	1.938	.775	.678	2.035	3.392	3.876	3.682	3.585	3.682	3.779	3.876	4.070	4.361	5.136	35
4	0	1.081	1.850	1.711	1.295	1.018	1.110		3.377	3.469	3.515	3.423	3.423	3.423	3.608	4.071	30
5	.13	.982	1.934	1.425	.865	.916	1.629	2.749	3.360	3.360	3.360	3.360	3.360	3.461	3.767	4.072	↓
6	.50	1.079	2.131	1.761	1.390	1.019	.927	2.224	3.243	3.614	3.706	3.706	3.984	3.984	4.262	4.726	
[a]7	1.00	.976	1.844	1.639	1.434	1.332	1.230	1.127	1.127	1.025	1.025	1.025	1.025	.922	.922	.820	
7	1.00	1.002	1.896	1.597	1.098	.798	.898	1.696	2.894	3.293	3.592	3.692	3.792	3.991	4.291	4.989	
[a]8	1.00	1.038	1.926	1.348	.963	.867	1.059	1.059	1.059	.867	.963	.963	.963	.915	.867	.963	
8	1.00	.979	1.838	1.634	1.124	.817	.919	1.685	2.962	3.371	3.677	3.779	3.881	3.983	4.290	4.698	
9	0	.967	2.223	1.789	1.375	.900	.693	.869	1.655	2.068	2.689	2.895	3.071	3.257	3.268	3.671	25
10	.13	1.001	1.698	1.498	1.199	.849	.699	.999	1.698	2.098	2.697	2.997	3.197	3.297	3.496	3.796	↓
11	.50	1.055	2.181	1.802	1.612	1.422	1.328	1.233	1.185	1.138	1.090	1.043	1.043	1.043	1.043	1.043	
12	1.00	1.081	1.942	1.758	1.480	1.388	1.295	1.156	1.110	1.110	1.110	1.064	1.018	.971	.925	.925	
13	.13	.912	2.084	1.645	1.535	1.316	1.206	1.151	1.097	.987	.877	.768	.658	.548	.439	.493	15
14	0	1.553	2.318	1.577	2.575	4.958	5.054	4.829	4.572	4.572	4.591	4.572	4.572	4.861	5.344	5.859	35
15	.13	1.607	2.054	1.494	1.805	4.294	4.792		4.668	4.605	4.605	4.605	4.792	4.917	5.352	5.975	↓
16	.50	1.676	2.148	1.611	1.194	2.984	5.013	5.072	5.072	5.072	5.251	5.072	5.311	5.490	5.968	6.505	
17	1.00	1.683	2.080	1.842	1.604	1.248	1.129		4.337	4.516	4.634	4.753	4.931	4.991	5.347	5.941	
18	0	1.698	1.620	1.414	1.355	1.060	1.767		4.064	4.005	4.094	4.064	3.976	4.035	4.359	4.712	30
19	.13	1.711	2.104	1.870	1.637	1.169	2.338	4.208	4.500	4.676	4.734	4.500	4.910	4.851	5.026	5.669	↓
20	.50	1.743	2.065	1.779	1.492	1.147	1.262	3.213	4.590	4.705	4.762	4.819	4.877	5.020	5.393	6.082	
21	1.00	1.607	1.805	1.618	1.431	1.120	.996	2.489	4.294	4.605	4.854	4.979	5.228	5.415	5.726	6.410	
22	0	1.705	2.112	1.731	1.566	1.349	1.173	.939	3.227	4.165	4.811	4.693	4.987	4.811	4.975	5.415	25
[b]23	.13	1.792	2.065	1.786	1.507	1.395	1.339	1.339	1.563	2.455	3.572	4.074	4.297	4.409	4.632	5.023	↓
[b]23	.13	1.594	2.321	2.008	1.694	1.506	1.380	1.317	1.255	1.192	1.129	1.067	1.004	.816	.753	.816	
24	.50	1.689	1.895	1.717	1.421	1.244	1.303	1.362	1.303	1.421	1.303	1.421	1.421	1.421	1.480	1.717	
25	1.00	1.586	2.144	1.639	1.513	1.324	1.261	1.198	1.198	1.198	1.229	1.229	1.198	1.198	1.166	1.135	
26	.13	1.559	2.630	1.989	1.732	1.450	1.379	1.219	1.219	1.187	1.174	1.123	1.091	1.091	1.039	.937	15
27	.13	1.657	2.173	1.690	1.509	1.268	1.207		1.147	1.087	1.087	1.087	1.087	1.026	1.026	.966	15
28	0.13	1.896	2.109	1.951	1.634	1.424	3.164		5.485	5.537	5.643	5.537	5.801	5.801	6.170	6.750	30
29	.50	1.867	2.143	1.982	1.822	1.554	1.982		5.840	5.840	6.108	6.108	6.322	6.376	6.751	7.340	30
30	1.00	1.896	2.109	1.846	1.582	1.477	1.477		1.582	1.688	1.793	1.899	2.004	2.057	2.109	2.215	30
31	0	2.074	2.218	1.784	1.422	1.254	1.287	1.157	2.387	3.534	4.243	4.580	4.701	4.749	4.966	5.328	25
32	.13	1.915	2.089	1.880	1.671	1.567	1.775		3.133	3.499	4.021	4.125	4.282	4.386	4.491	4.595	15
33	0	1.940	9.280	8.760	7.890	7.010	7.110	6.700	6.440	6.190	6.390	6.080	6.080	6.080	5.980	5.880	35

[a] Attached flow.

[b] Oscillating flow separation.

TABLE V.- Continued

Test	A_l/A_e	$\dot{q}_{ref}$, Btu/ft^2-sec	Cove									Rub		Bulkhead	δ, deg
			$\dot{q}_{15}/\dot{q}_{ref}$	$\dot{q}_{16}/\dot{q}_{ref}$	$\dot{q}_{17}/\dot{q}_{ref}$	$\dot{q}_{18}/\dot{q}_{ref}$	$\dot{q}_{19}/\dot{q}_{ref}$	$\dot{q}_{20}/\dot{q}_{ref}$	$\dot{q}_{21}/\dot{q}_{ref}$	$\dot{q}_{22}/\dot{q}_{ref}$	$\dot{q}_{23}/\dot{q}_{ref}$	$\dot{q}_{24}/\dot{q}_{ref}$	$\dot{q}_{25}/\dot{q}_{ref}$	$\dot{q}_{45}/\dot{q}_{ref}$	
1	0.13	1.008	3.024	2.082	1.884	1.091	1.438	0.942	1.735	0.149	1.091	1.140	0.198	0.297	35
2	.50	1.032	4.845	3.537	3.052	2.035	2.568	1.744	2.956	2.326	3.149	2.568	1.454	3.973	35
3	1.00	1.032	5.524	4.118	3.779	2.132	3.440	2.520	7.026	3.101	2.229	3.682	2.229	5.087	35
4	0	1.081	2.220	1.341	1.110	.648	.601	.416	.463	.046	.139	.046	.046		30
5	.13	.982	2.698	1.833	1.527	.916	1.069	.662	1.273		.865	.916	.204	.356	↓
6	.50	1.079	4.865	3.614	3.243	2.363	2.502	1.946	.510	2.085	2.733	2.363	.046	3.150	↓
[a]7	1.00	.976	1.178	.820	.666	.307	.461	.307	.820	.359	.154	.359	.307	.512	↓
7	1.00	1.002	3.892	2.994	2.744	1.746	2.594	1.796	5.488	2.295	1.696	2.744	1.746	4.041	↓
[a]8	1.00	1.038	1.108	.722	.578	.241	.433	.337	.770	.337	.144	.337	.289	.481	↓
8	1.00	.979	4.596	3.371	3.064	1.736	2.962	2.145	6.230	2.656	2.673	3.013	1.838	4.391	↓
9	0	.967	1.913	1.215	.807	.595	.491	.362	.259	.134	.052	.031	.021		25
10	.13	1.001	2.797	1.898	1.498	.999	1.049	.749	1.199		.749	.849	.200	.400	↓
11	.50	1.055	.853	.522	.427	.284	.284	.237	.095	.190	.190	.237	.028	.332	↓
12	1.00	1.081	.786	.463	.370	.185	.278	.185	.370	.185	.093	.231	.185	.278	↓
13	.13	.912	.329	.186	.164	.110	.055	.055	.143	.274	.110	.055	.110		15
14	0	1.553	3.316	2.356	2.028	1.223	1.417	1.095	1.288	0.567		0.116	0.097		35
15	.13	1.607	4.108	3.112	2.738	1.556	2.023	1.431	1.089	.373	1.867	1.992	.560	0.871	↓
16	.50	1.676	5.968	4.446	4.267	2.238	3.491	2.835	5.013	3.461	5.251	3.640	2.238	6.445	↓
17	1.00	1.683	5.407	4.159	4.159	2.852	3.981	2.763	6.951	3.684	3.565	4.753	2.971	7.724	↓
18	0	1.698	2.091	1.325	1.090	.618	.795	.677	.589	.003	.206	.030	.059		30
19	.13	1.711	4.296	3.098	2.718	1.578	2.046	1.578	2.046	.438	1.461	1.607	.526	.701	↓
20	.50	1.743	4.733	3.672	3.500	1.893	3.098	2.295	3.901	2.639	4.074	2.983	1.779	5.336	↓
21	1.00	1.607	6.535	5.166	5.041	3.018	4.792	3.485	7.468	4.201	3.952	5.446	3.454	6.846	↓
22	0	1.705	3.074	2.006	1.525	.939	.880	.704	.516	.411		.044	.059		25
[b]23	.13	1.792	3.432	2.455	2.009	1.172	1.507	1.172	1.618	.167	1.060	1.116	.558	.670	↓
[b]23	.13	1.594	.471	.314	.282	.125	.188	.094	.314	.063	.125	.188	.125	.157	↓
24	.50	1.689	.474	.326	.237	.207	.296	.178	.089	.148	.148	.207	.148	.503	↓
25	1.00	1.586	.902	.631	.473	.252	.221	.189	.315	.189	.126	.189	.158	.441	↓
26	.13	1.559	.334	.208	.180	.112	.109	.083	.039	.051		.019			15
27	.13	1.657	.211	.121	.091	.060	.060	.030	.091	.030	.060	.060	.121	.030	15
28	0.13	1.896	4.061	2.795	2.505	1.187	1.793	1.318	2.294	0.396	1.846	1.978	0.633	1.055	30
29	.50	1.867	6.697	4.929	4.554	2.384	3.616	2.518	4.500	3.429	6.429	3.991	2.277	6.697	30
30	1.00	1.896	.580	.316	.290	.185	.264	.211	.264	.185	.053	.053	.237	.264	30
31	0	2.074	3.592	2.473	1.914	1.080	1.037	.786	.709	.362		.060	.082		25
32	.13	1.915													15
33	0	1.940	1.860	0.773	0.515	0.387	0.258	0.052	0.026				0.052		35

[a] Attached flow.
[b] Oscillating flow separation.

TABLE V.- Concluded

Test	A_l/A_e	$\dot{q}_{ref}$, Btu/ft^2-sec	Ramp											δ, deg
			$\dot{q}_{33}/\dot{q}_{ref}$	$\dot{q}_{34}/\dot{q}_{ref}$	$\dot{q}_{35}/\dot{q}_{ref}$	$\dot{q}_{36}/\dot{q}_{ref}$	$\dot{q}_{37}/\dot{q}_{ref}$	$\dot{q}_{38}/\dot{q}_{ref}$	$\dot{q}_{39}/\dot{q}_{ref}$	$\dot{q}_{40}/\dot{q}_{ref}$	$\dot{q}_{41}/\dot{q}_{ref}$	$\dot{q}_{42}/\dot{q}_{ref}$	$\dot{q}_{43}/\dot{q}_{ref}$	
1	0.13	1.008	4.462	4.958	5.950	6.941	7.933	8.924	10.908	11.899	13.882	15.866	33.714	35
2	.50	1.032	5.814	6.783	7.752	8.237	10.175	11.628	14.536	16.474	19.381	25.195	32.947	35
3	1.00	1.032	6.783	6.783	6.783	8.721	10.659	12.598	14.536	17.443	21.319	23.257	28.102	35
4	0	1.081	4.626	7.401	20.353	11.101	13.877	15.727	17.577	19.428	21.278	24.053	43.481	30
5	.13	.982	5.090	6.108	7.127	8.145	9.163	10.181	12.217	13.235	15.271	16.289	35.632	↓
6	.50	1.079	7.876	11.119	15.289	16.679	17.605	18.995	21.311	24.555	26.871	28.724	33.357	
[a]7	1.00	.976	7.172	15.369	18.442	20.492	23.565	24.590	26.639	27.664	28.688	29.201	37.909	
7	1.00	1.002	4.989	5.987	6.985	8.981	9.979	10.976	12.972	13.970	15.966	16.964	18.959	
[a]8	1.00	1.038	8.668	14.446	17.336	20.225	23.114	24.077	25.040	26.485	26.966	27.929	34.671	
8	1.00	.979	5.107	6.128	8.171	9.192	10.214	11.235	14.810	16.342	18.385	20.428	22.981	
9	0	.967	4.447	5.687	5.687	8.273	9.824	10.856	12.409	13.443	13.960	15.511		25
10	.13	1.001	3.996	5.994	6.993	8.991	9.990	10.989	12.987	13.986	15.984	16.983	27.971	↓
11	.50	1.055	7.112	11.379	13.276	15.646	18.017	19.913	20.862	22.758	23.706	24.655	27.499	
12	1.00	1.081	7.864	12.027	12.952	14.802	17.577	18.502	20.353	21.278	22.665	24.053	27.754	
13	.13	.912	2.193	4.387	5.483	7.128	8.773	10.967	12.063	13.160	13.708	14.257	14.257	15
14	0	1.553	6.439	7.726	7.726	9.658	11.268	12.234	14.809	16.741	19.316	21.441		35
15	.13	1.607	6.846	8.091	9.335	10.580	11.203	11.825	13.692	15.559	18.049	21.783	40.454	↓
16	.50	1.676	7.161	8.951	9.548	10.742	11.935	14.919	16.709	19.693	22.677	26.257	35.805	
17	1.00	1.683	7.130	8.912	9.209	11.883	14.854	16.042	17.824	20.795	23.766	26.737	32.084	
18	0	1.698	5.301	6.774		8.835	10.602	11.780	13.547	15.609	17.081	19.437	32.984	30
19	.13	1.711	7.014	8.183	9.351	11.105	11.689	13.443	15.781	17.534	18.703	21.625	41.497	↓
20	.50	1.743	6.885	8.606	9.754	10.901	13.196	14.917	16.638	18.933	21.802	25.245	28.687	
21	1.00	1.607	8.091	9.958	11.825	14.314	16.804	19.916	22.405	27.384	29.873	35.475	47.300	
22	0	1.705	6.746	9.093	9.152	12.613	14.373	15.722	17.423	19.535	21.471	24.053		25
[b]23	.13	1.792	6.697	13.394	19.532	21.206	22.323	25.113	26.787	28.461	30.135	31.252	39.064	↓
[b]23	.13	1.594	5.646	7.528	6.274	12.547	15.057	17.566	18.821	20.076	22.585	25.095	37.642	
24	.50	1.689	15.988	17.765	18.357	20.725	21.910	22.502	23.094	24.870	27.239	28.423	34.937	
25	1.00	1.586	14.502	17.654	18.915	20.176	20.176	19.546	19.546	20.807	22.698	23.959	31.525	
26	.13	1.559	7.249	11.868	14.114	14.434	15.717	16.423	17.321	17.963	18.604	19.566		15
27	.13	1.657	8.451	10.262	10.865	11.469	12.073	12.676	13.280	13.884	14.487	15.091	16.298	15
28	0.13	1.896	7.383	8.965	24.259	12.129	14.239	15.821	17.930	20.567	23.204	26.368	37.970	30
29	.50	1.867	8.036	10.179		13.394	15.001	17.144	19.823	21.966	25.181	28.931	33.753	30
30	1.00	1.896	17.403	17.930	22.149	20.040	20.567	21.095	22.149	23.204	24.786	26.105	29.005	30
31	0	2.074	6.509	8.052	8.679	11.572	12.777	14.947	16.634	18.563	20.491	22.179		25
32	.13	1.915	10.444	11.488	9.340	12.533	13.577	14.621	15.144	16.188	16.710	17.232	19.321	15
33	0	1.940	16.490	47.420	84.540		84.540	80.930	77.320	72.160				35

[a] Attached flow.

[b] Oscillating flow separation.

TABLE VI.- ROOT-MEAN-SQUARE DIFFERENCE BETWEEN MEASURED AND CALCULATED COVE HEATING RATES

$N_{Re,\infty}$, ft^{-1}	Root-mean-square difference, percent								
	$\delta = 25^{\circ}$			$\delta = 30^{\circ}$			$\delta = 35^{\circ}$		
	A_l/A_e								
	0.13	0.50	1.00	0.13	0.50	1.00	0.13	0.50	1.00
0.35×10^6	35	[a]11	[a]20	14	14	36 [a]20	28	21	19
1.00	58 [a]46	[a]23	[a]24	140	21	35	34	22	27
1.38				57	20	[a]25			

[a] Attached flow.

Error

An error occurred while processing this page. See the system log for more details.

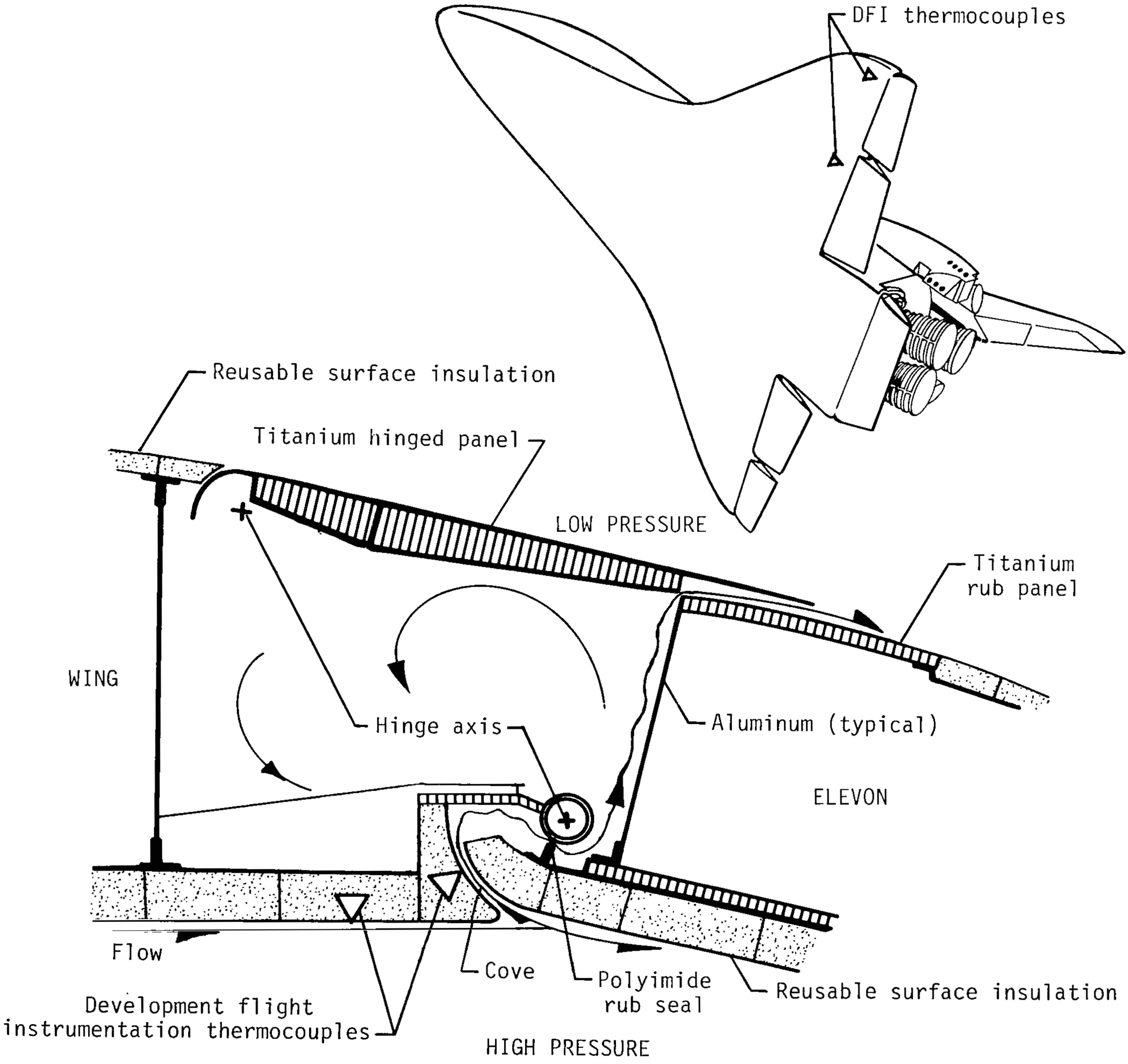

Figure 1.- Cross section of Space Shuttle orbiter structure at wing-elevon juncture.

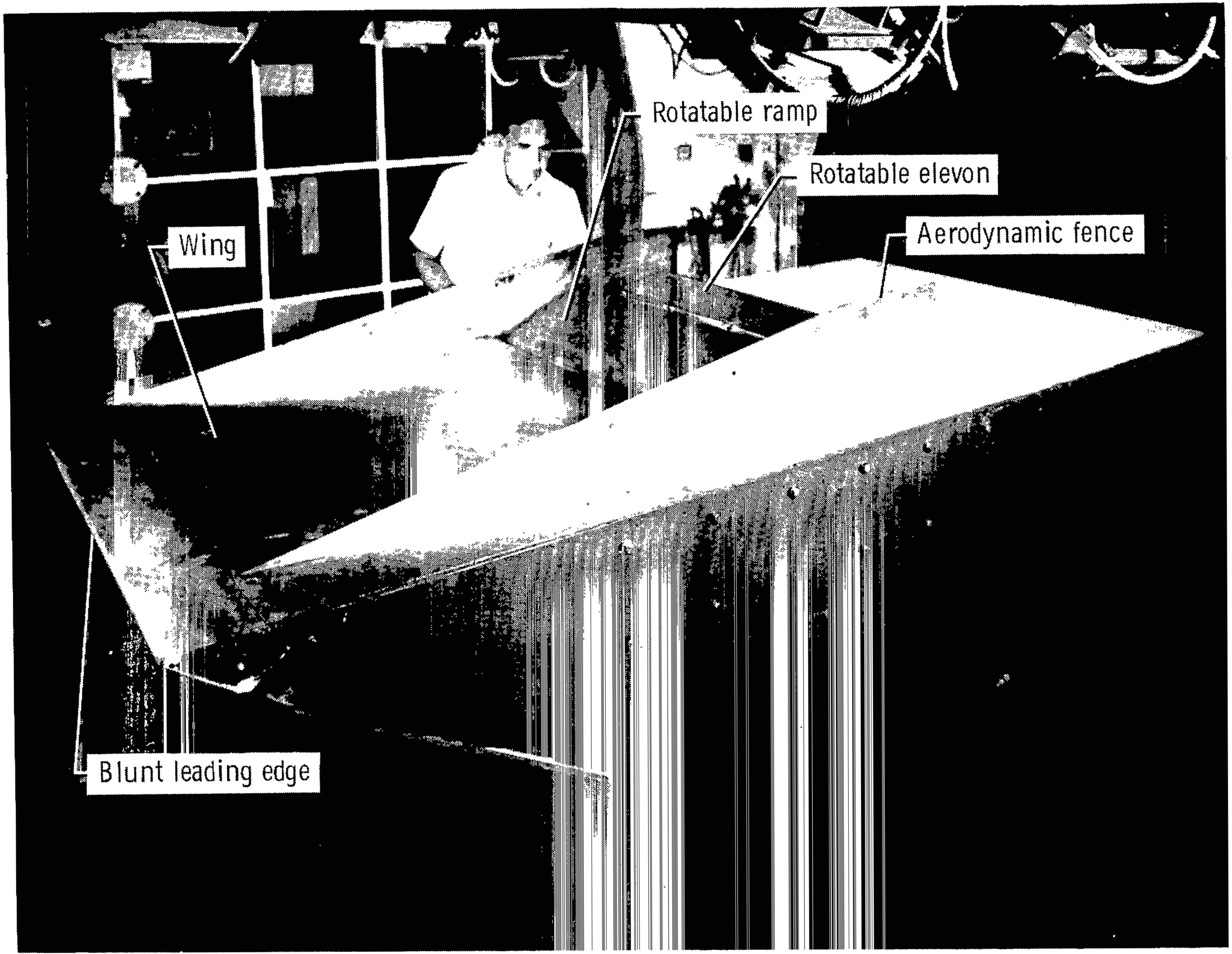

L-80-7504

Figure 2.- Separated-flow test installation.

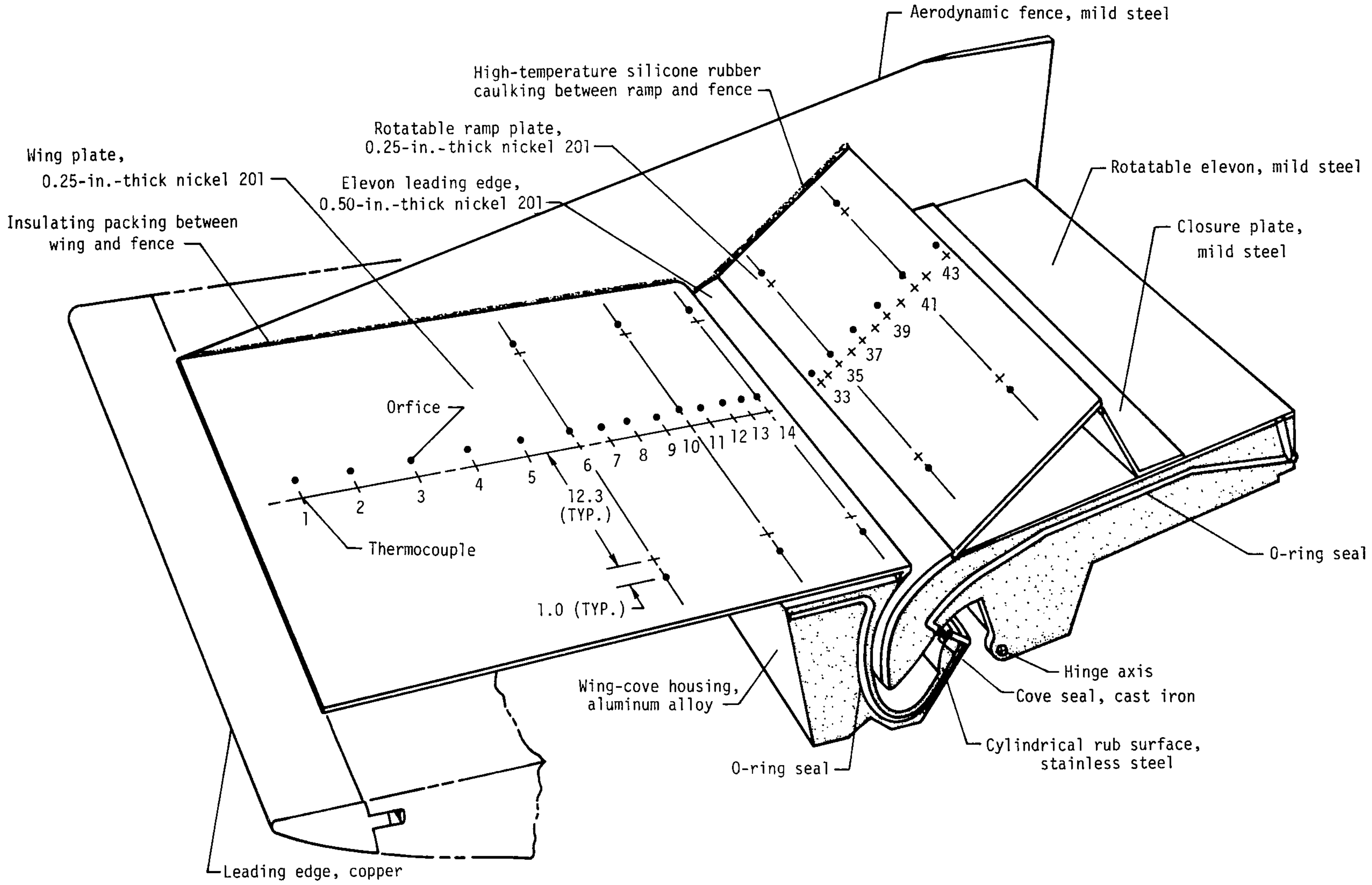

Figure 3.- Illustration of model with one aerodynamic fence removed to show relationship of components and distribution of surface instrumentation.

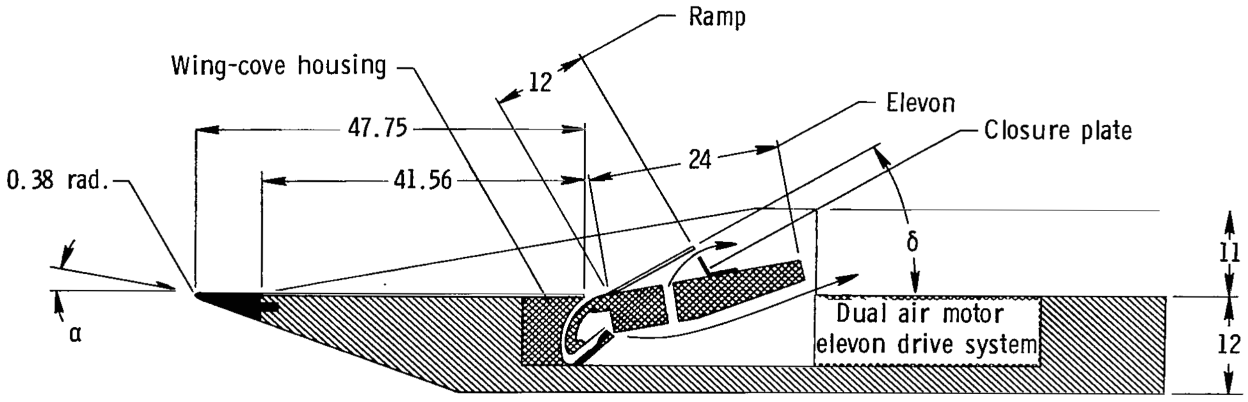

(a) Simplified longitudinal cross section.

(b) Cross section of aerodynamic fence. (c) Detail of wing at cove entrance.

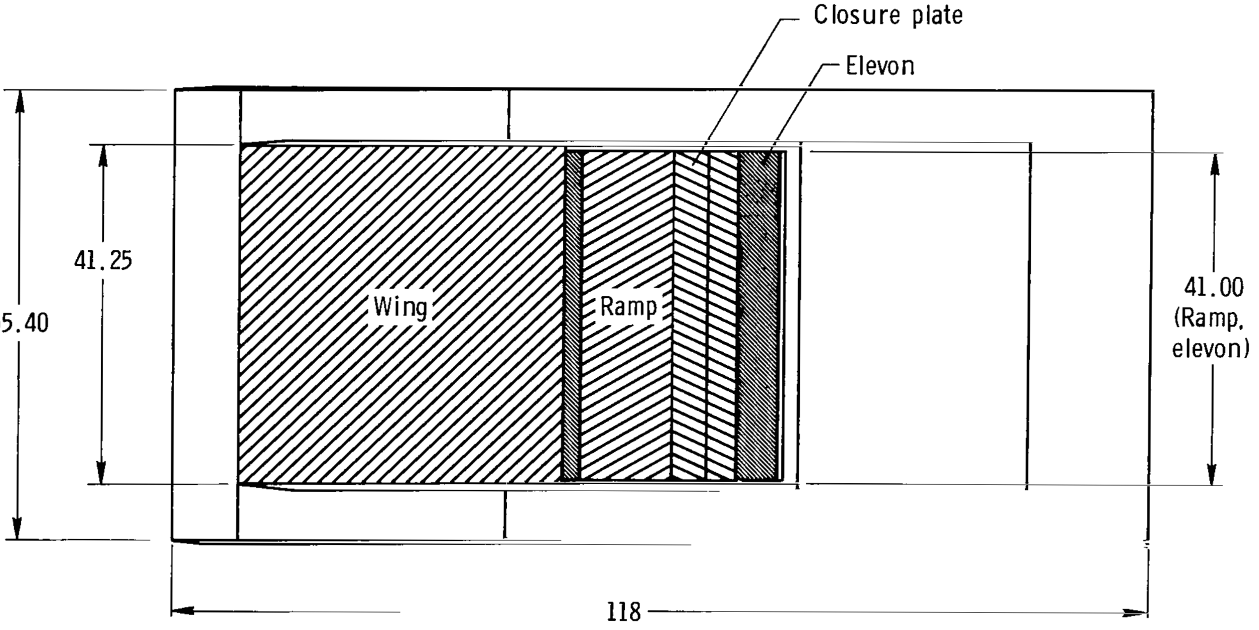

(d) Plan view.

Figure 4.- Details of model and test bed assembly. Linear dimensions are in inches.

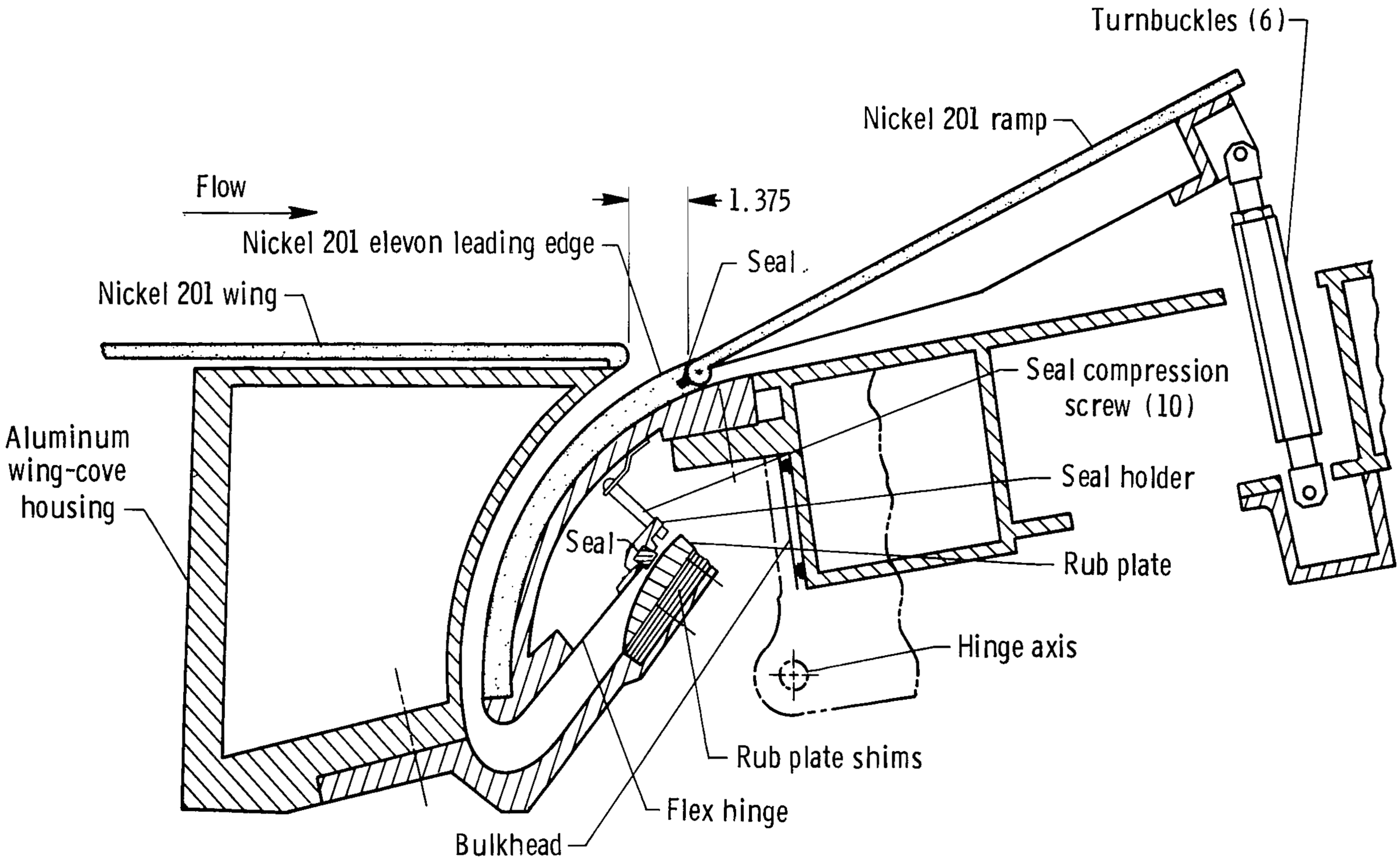

(a) Arrangement of wing-cove housing, elevon, ramp, and seal (elevon deflected 10°).

Figure 5.- Cross section of model at juncture of wing and elevon. Linear dimensions are in inches.

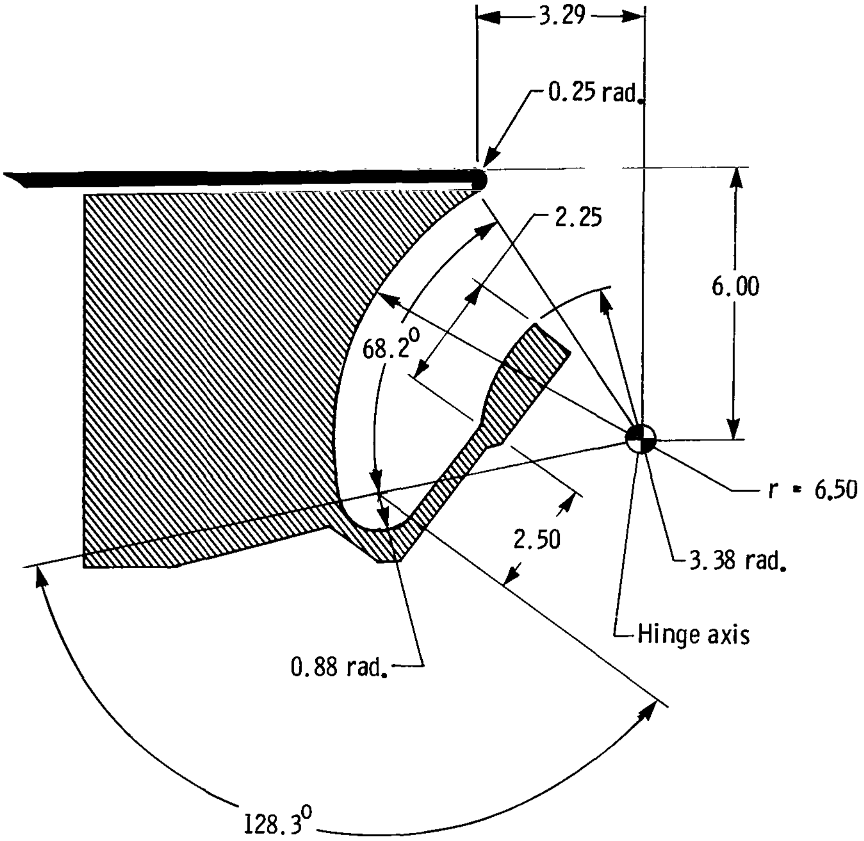

(b) Wing-cove housing.

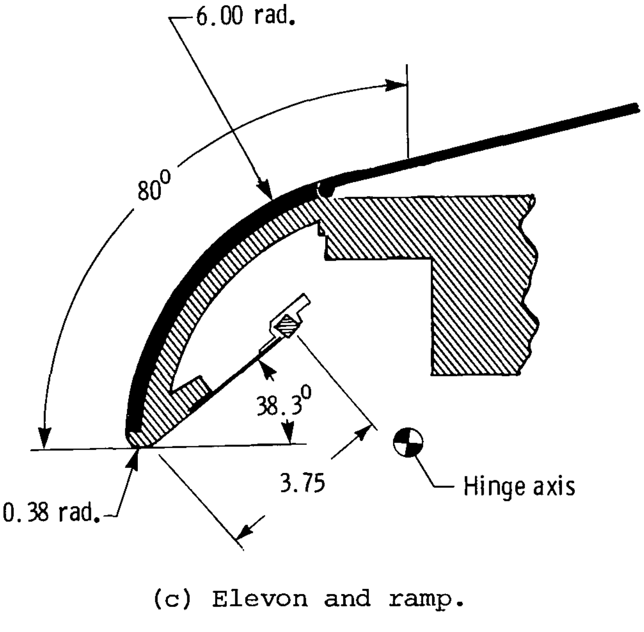

(c) Elevon and ramp.

Figure 5.- Concluded.

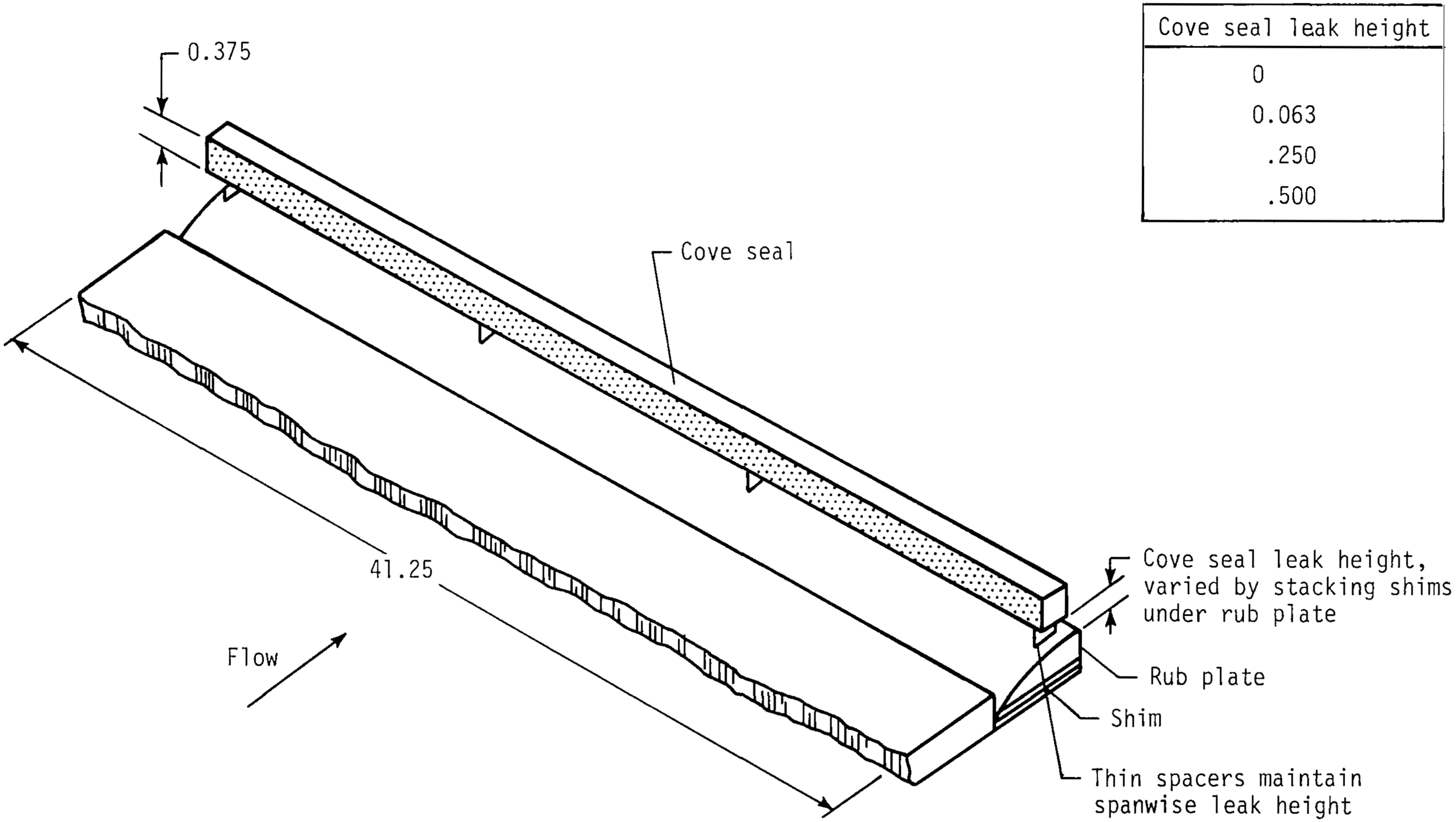

Cove seal leak height
0
0.063
.250
.500

Figure 6.- Seal and rub surface arrangement. Dimensions are in inches.

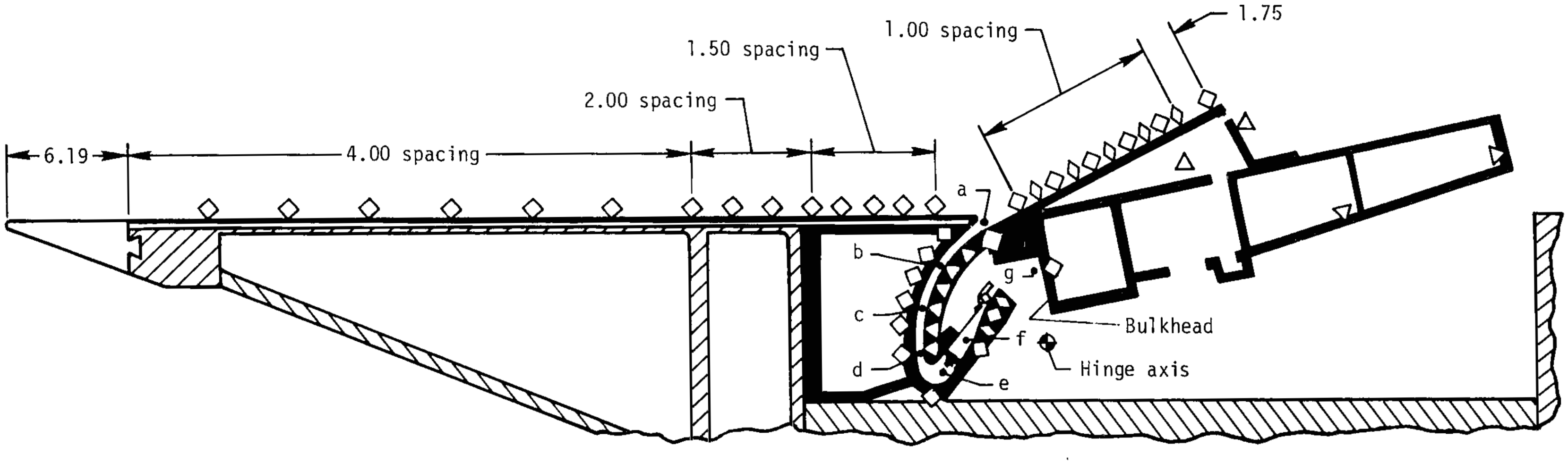

Distance of thermocouple from wall at location-	
a-f	g
0.25	0.06

Symbol	Sensors
•	Cove gas thermocouple (5 spanwise at g)
◀	Pitot pressure probe
◊	Wall thermocouple
◇	Wall thermocouple and static pressure orifice
△	Static pressure orifice

Figure 7.- Cross section of model showing centerline instrumentation distribution. Dimensions are in inches.

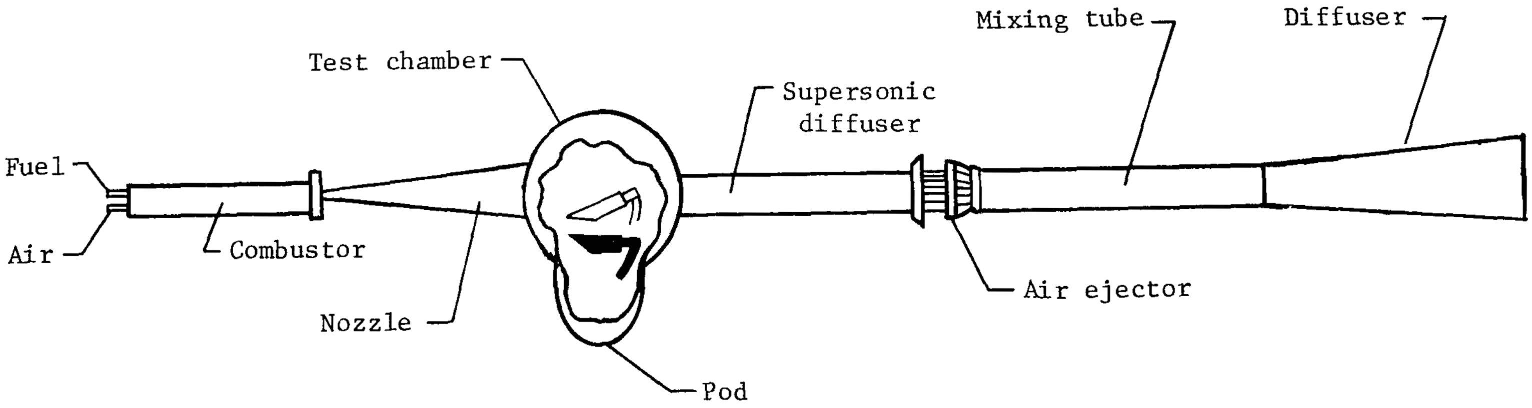

Figure 8.- Schematic of Langley 8-Foot High-Temperature Tunnel.

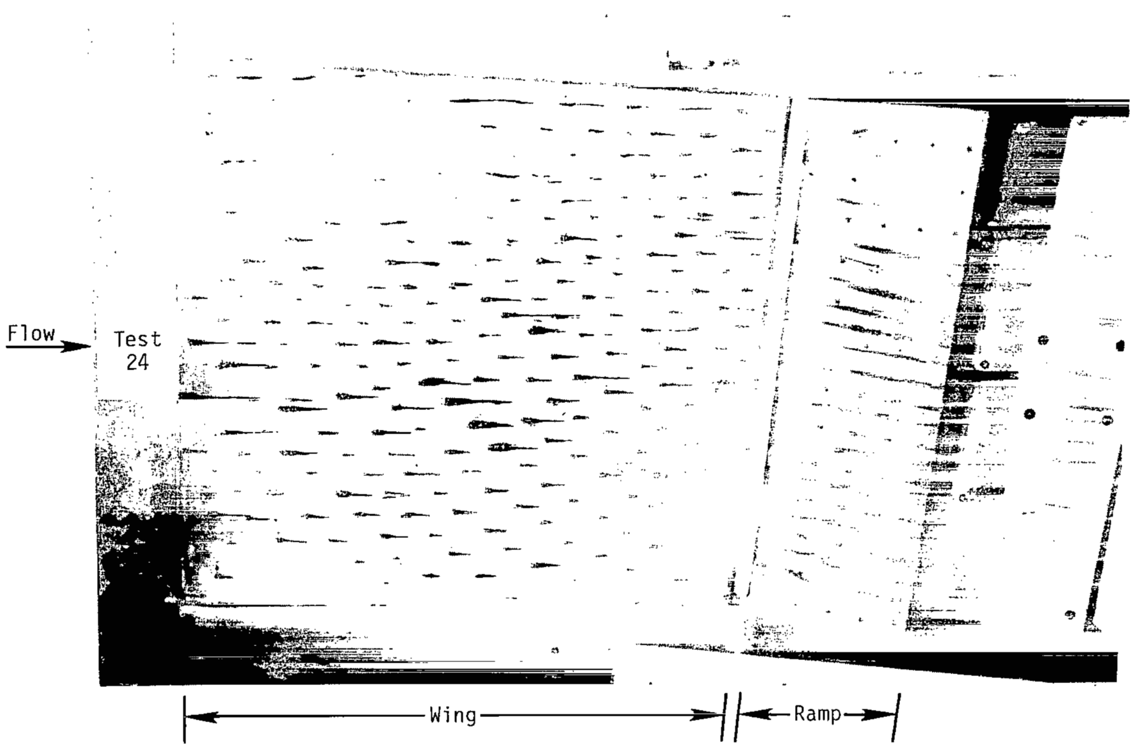

L-80-8703.1

(a) Attached flow on wing and ramp for
$\delta = 25^\circ$ and $A_l/A_e = 0.50$.

Figure 9.- Oil-flow patterns on wing, ramp, and aerodynamic fence.
$\alpha = 5^\circ$; $M_\infty = 6.9$; $N_{Re,\infty} \approx 1.00 \times 10^6 \text{ ft}^{-1}$.

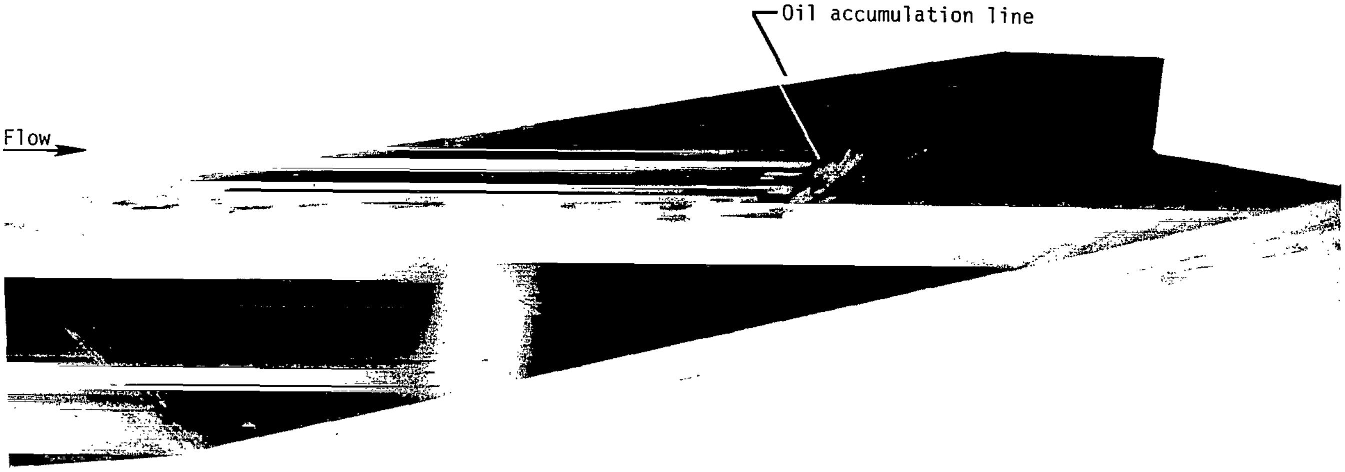

L-80-8795.1

(b) Attached flow on fence for $\delta = 25^\circ$ and $A_l/A_e = 0.50$.

Figure 9.- Continued.

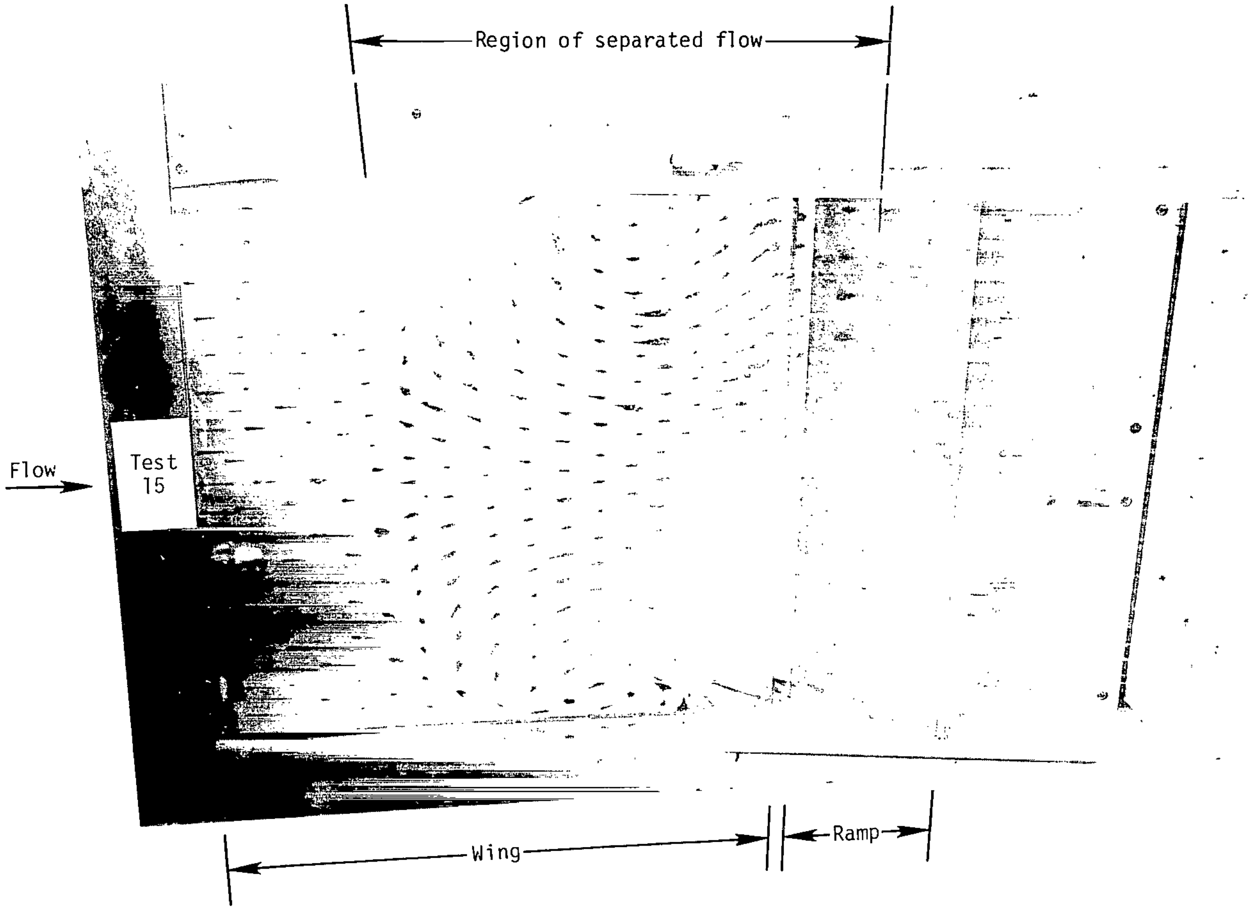

L-80-8963.1

(c) Separated flow on wing and ramp for $\delta = 35^\circ$ and $A_l/A_e = 0.13$.

Figure 9.- Continued.

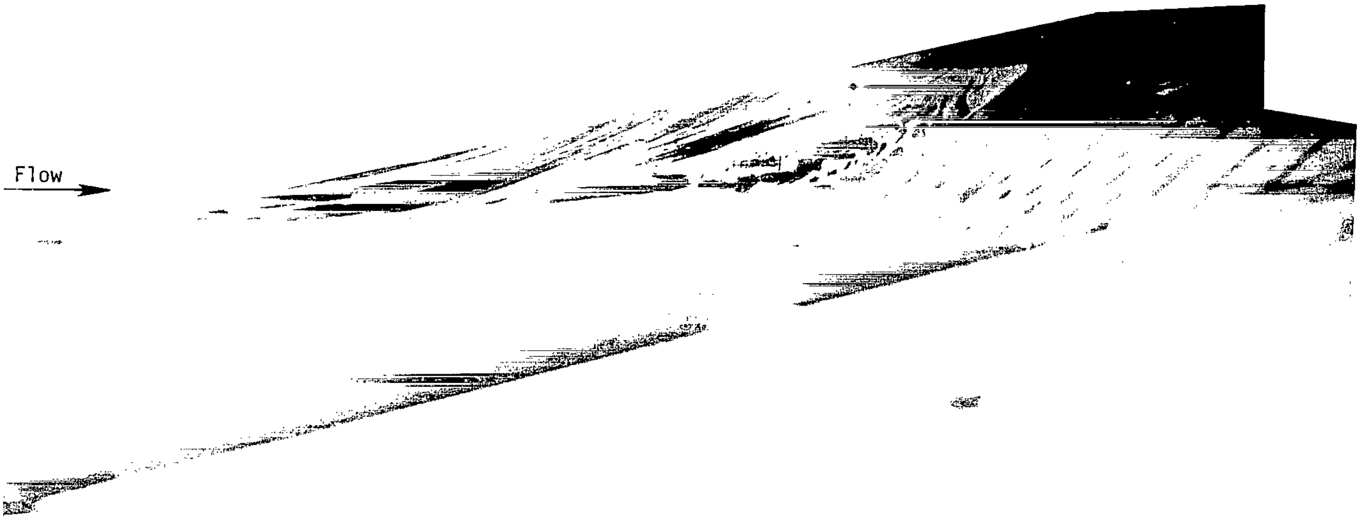

L-80-8965.1

(d) Separated flow on fence for $\delta = 35^{\circ}$ and $A_l/A_e = 0.13$.

Figure 9.- Concluded.

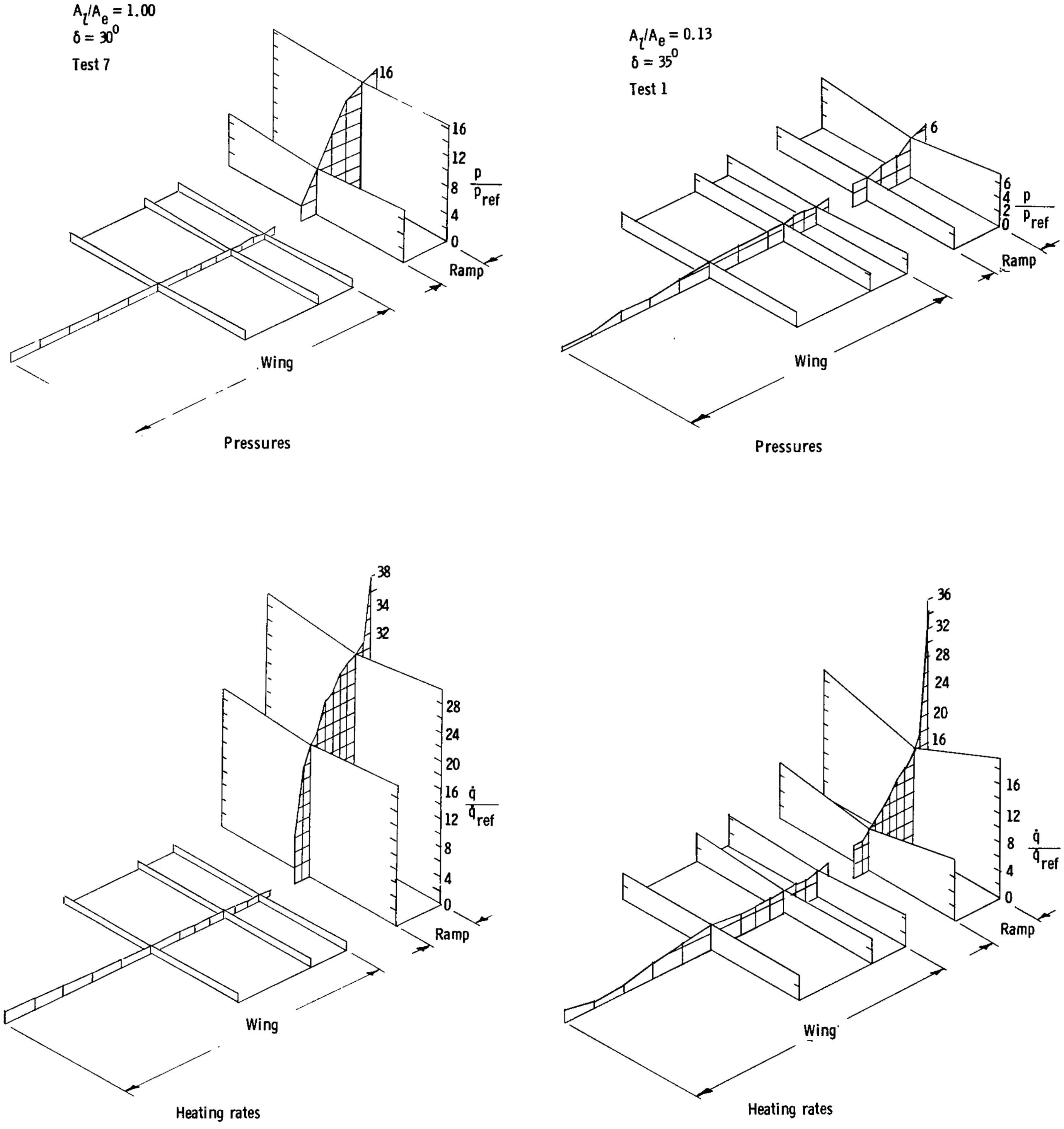

(a) Attached flow.

(b) Separated flow.

Figure 10.- Typical surface distributions of pressures and cold-wall heating rates on wing and ramp for attached and separated boundary layers. $\alpha = 5^{\circ}$; $\delta = 35^{\circ}$; $M_{\infty} = 6.9$; $N_{Re,\infty} \approx 0.35 \times 10^6 \text{ ft}^{-1}$.

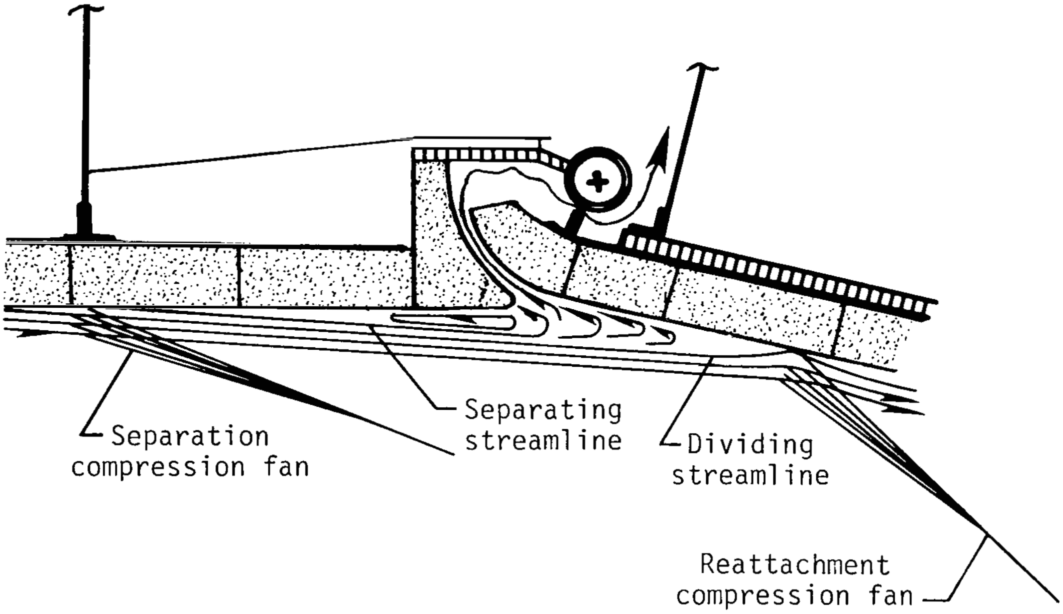

Figure 11.- Simplified flow details across cove entrance for separated flow.

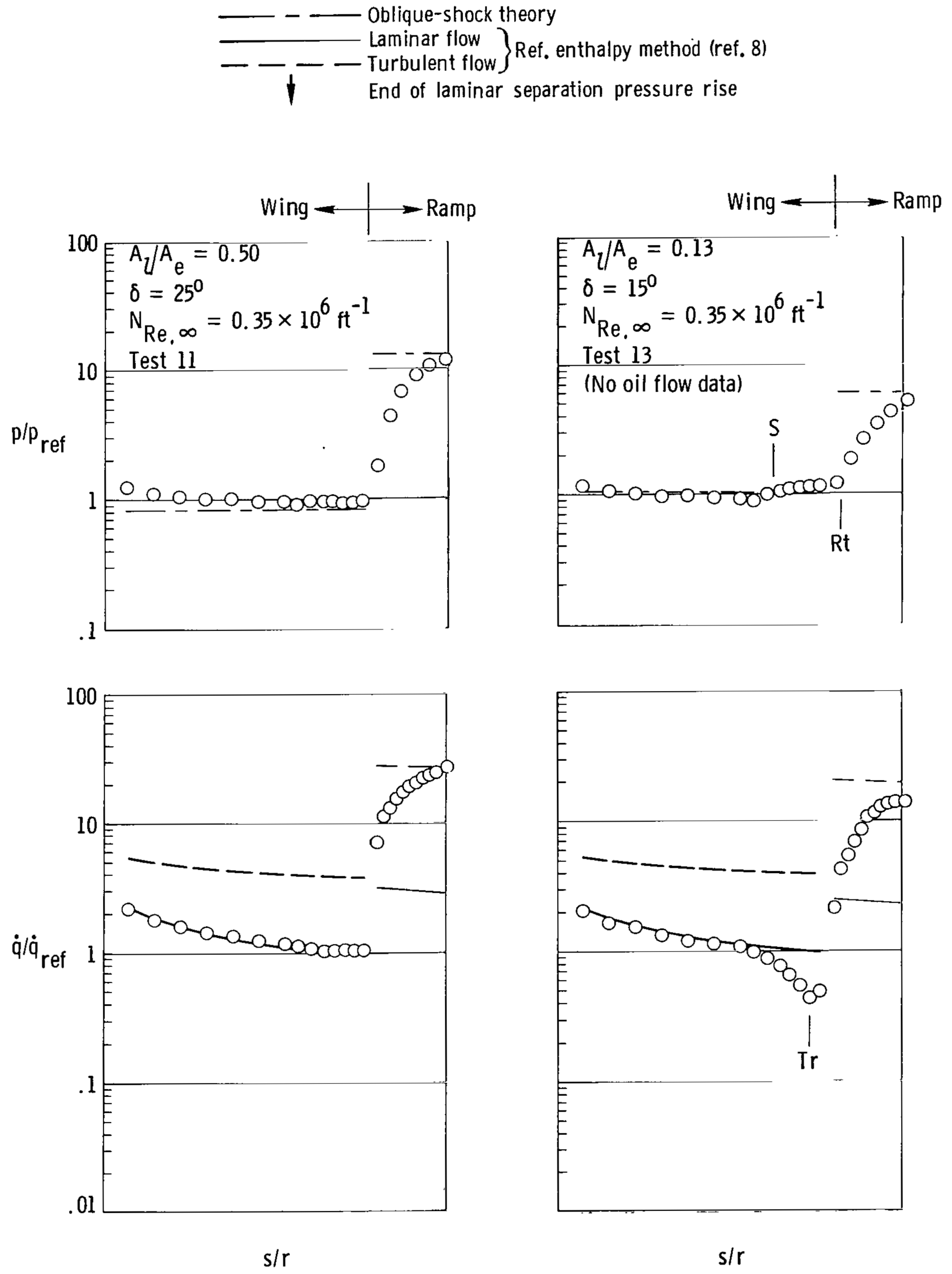

(a) Laminar attached flow.

(b) Quasi-laminar separated flow.

Figure 12.- Typical flow characteristics on wing and ramp surfaces. $M_\infty = 6.9$; $T_t \approx 3360^\circ R$; $\alpha = 5^\circ$.

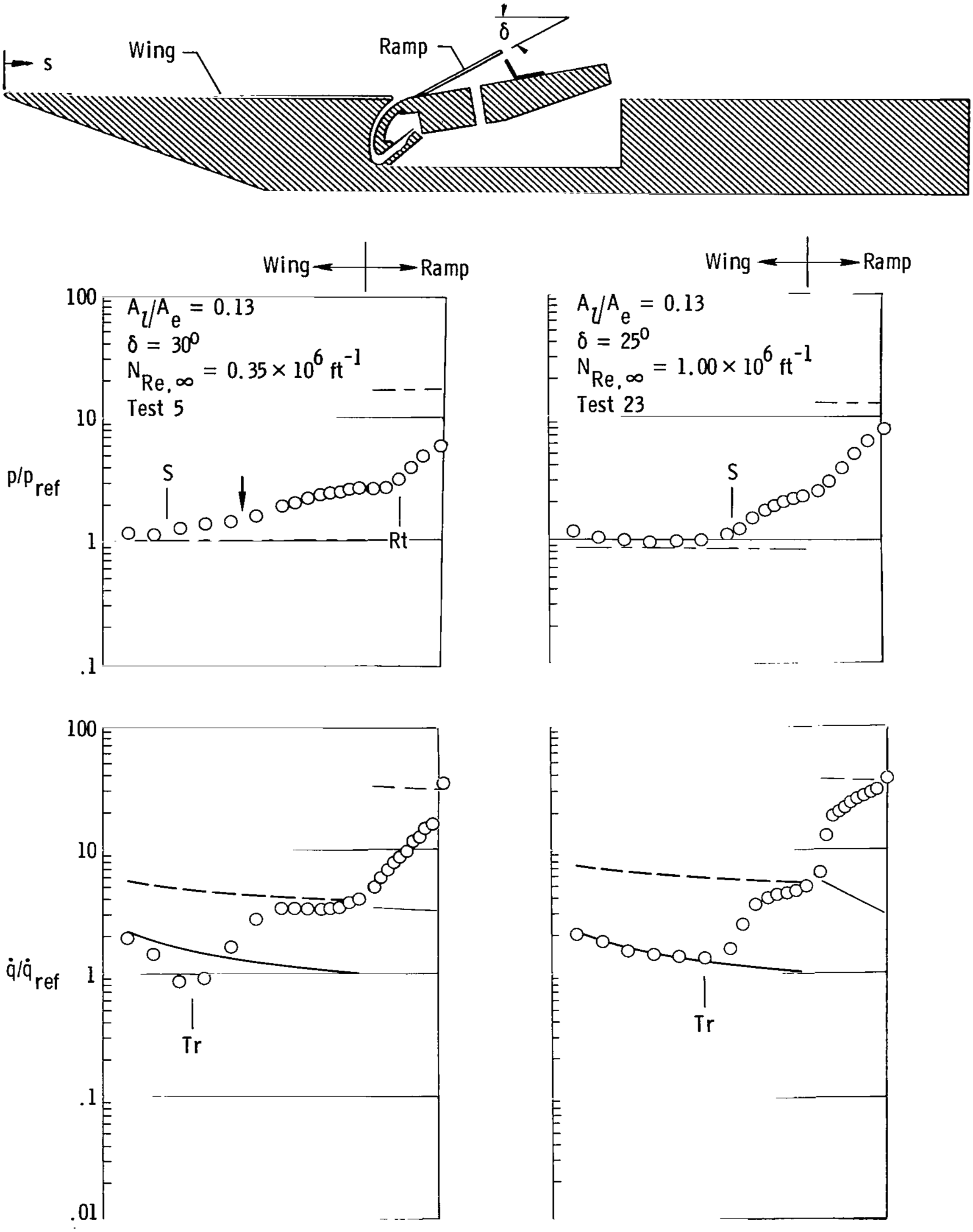

s/r

s/r

(c) Transitional separated flow (transition starts downstream of separation).

(d) Turbulent separated flow (transition starts upstream of separation).

Figure 12.- Concluded.

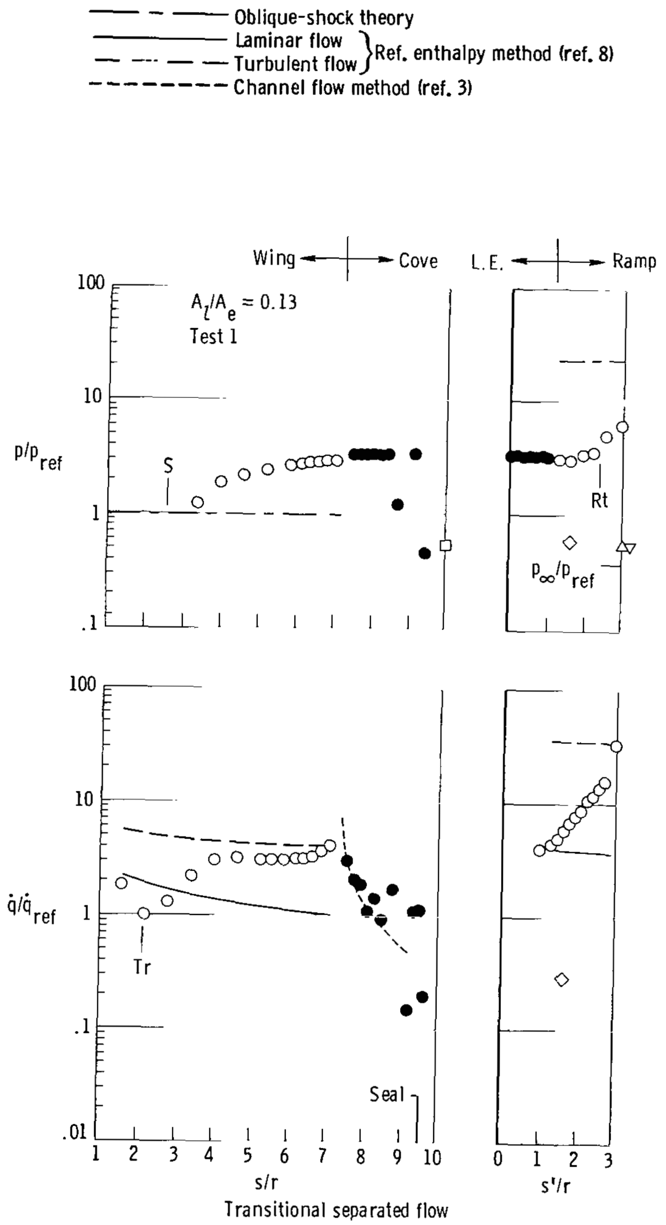

(a) $\delta = 35^\circ$.

Figure 13.- Centerline pressure and cold-wall heating-rate distributions at $N_{Re,\infty} \approx 0.35 \times 10^6$ ft^{-1} for various cove seal leak area ratios and ramp angles. $M_\infty \approx 6.9$; $T_t \approx 3360^\circ R$; $\alpha = 5^\circ$.

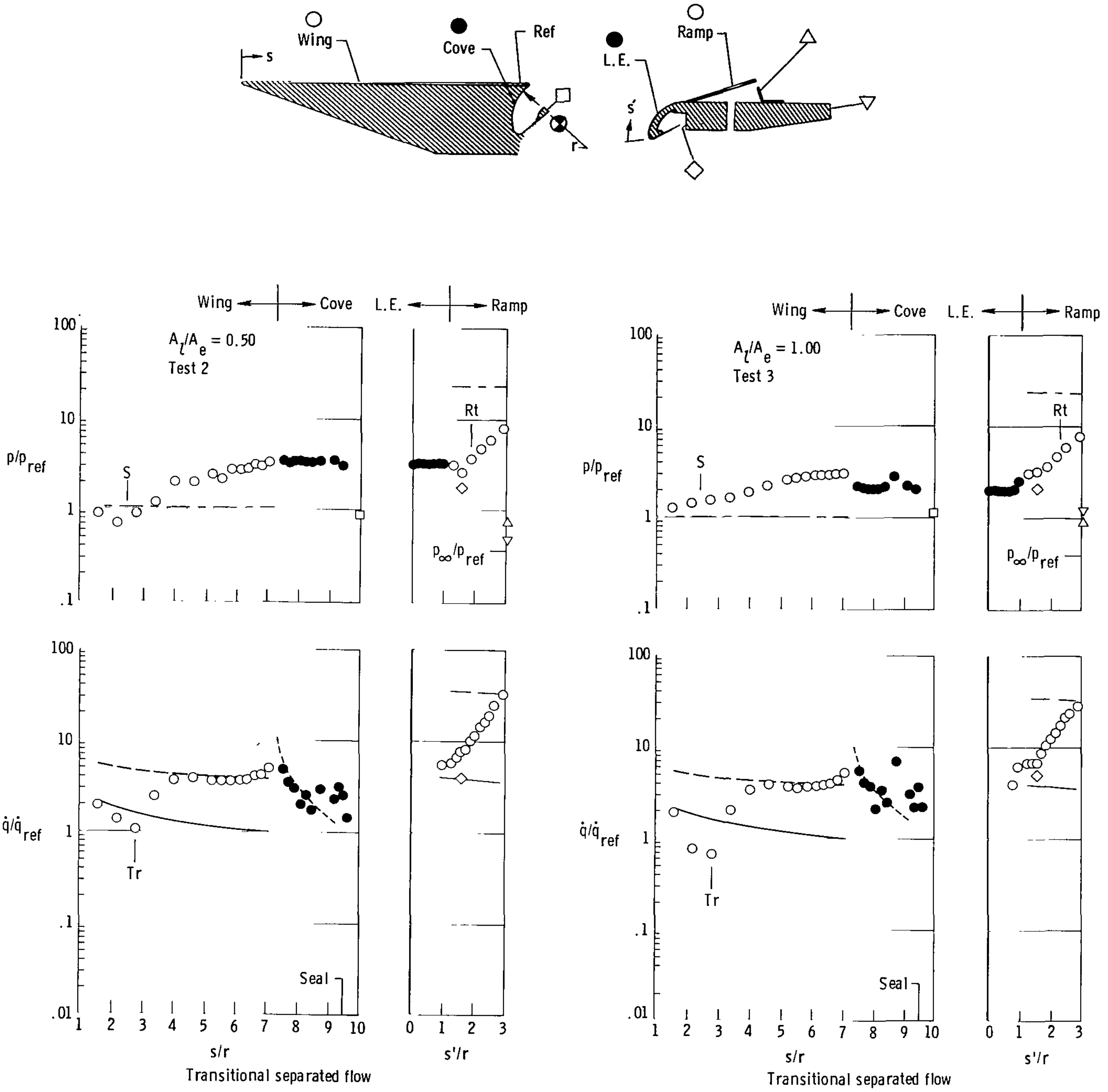

(a) δ = 35°.

Figure 13.- Continued.

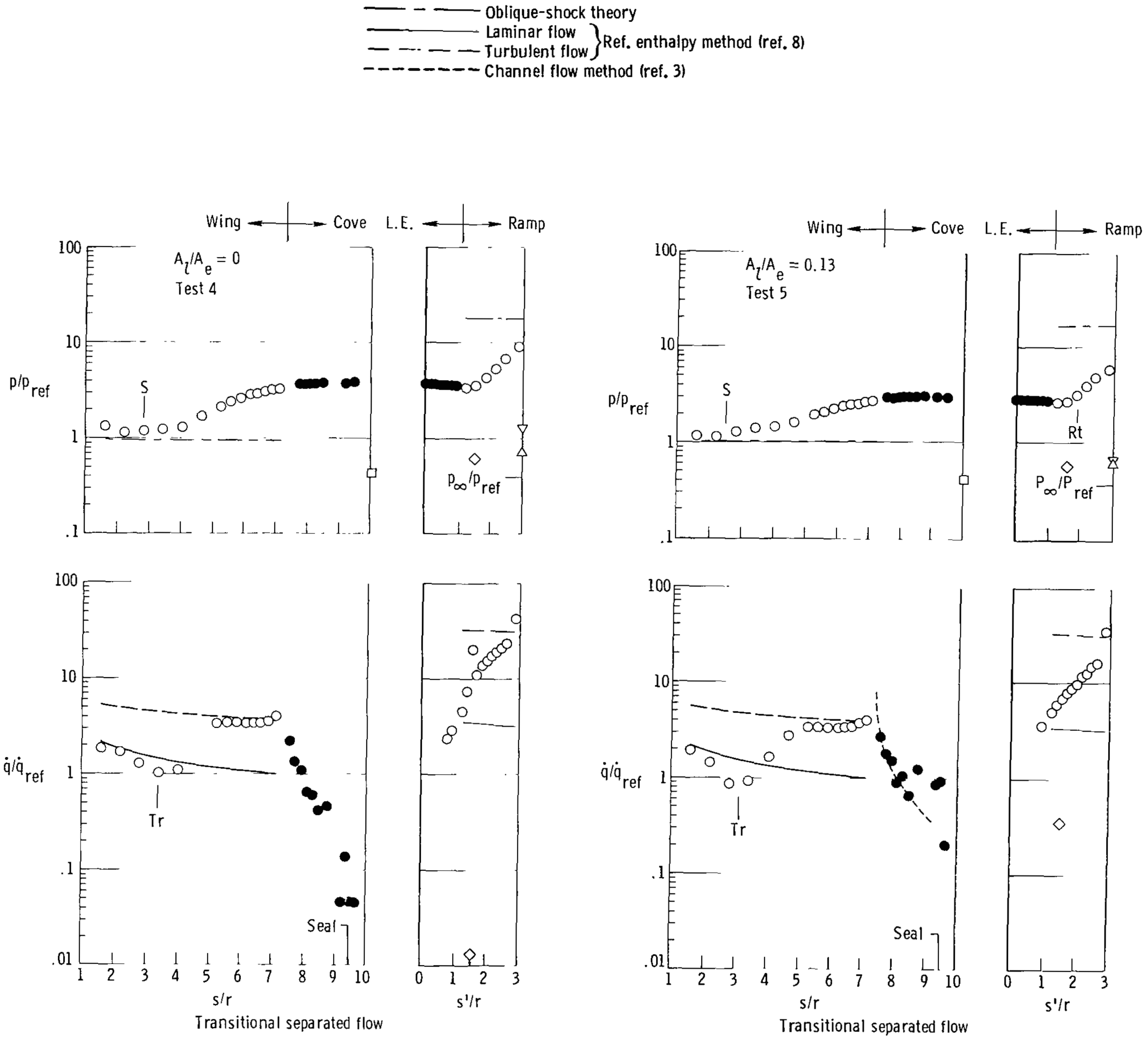

(b) $\delta = 30^\circ$.

Figure 13.- Continued.

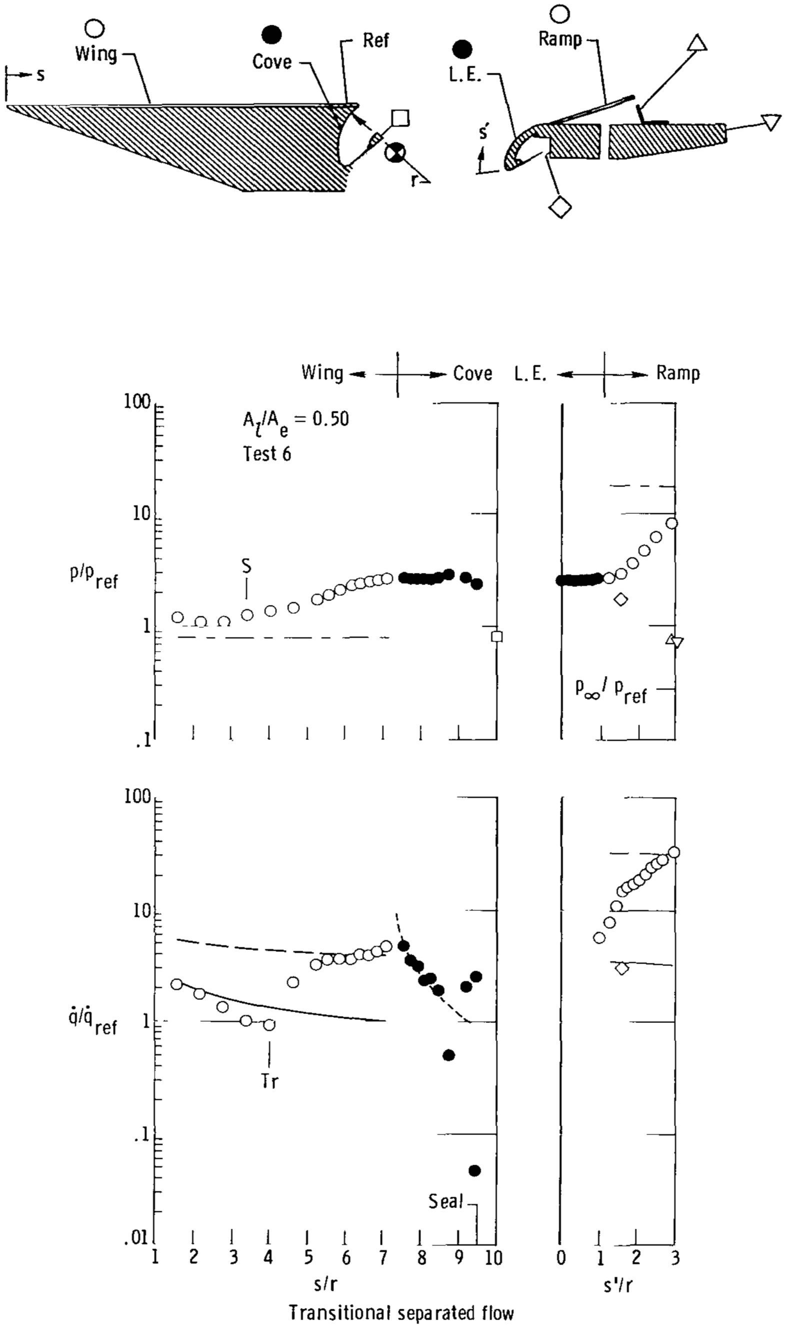

(b) $\delta = 30^\circ$.

Figure 13.- Continued.

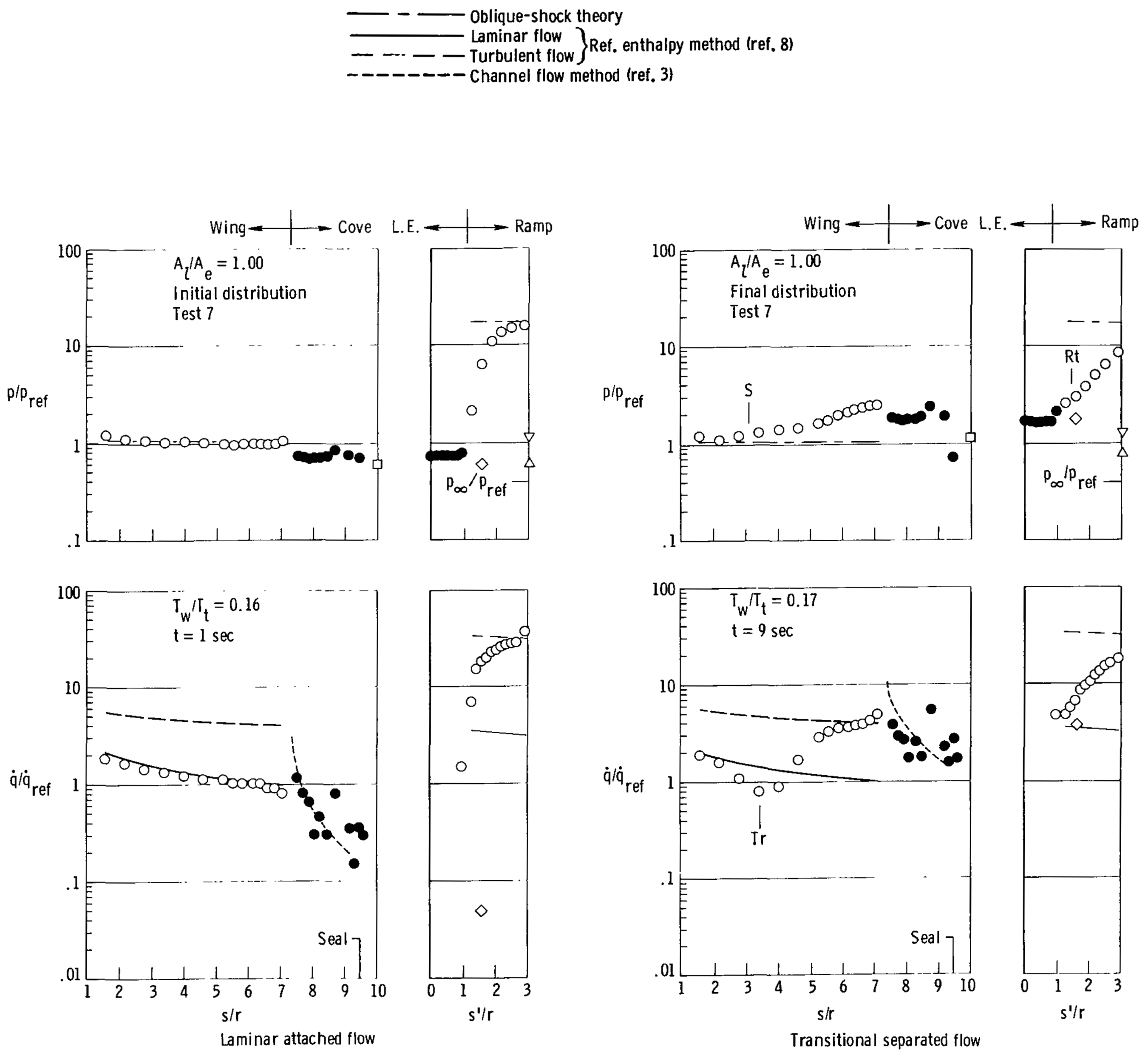

(b) $\delta = 30^\circ$.

Figure 13.- Continued.

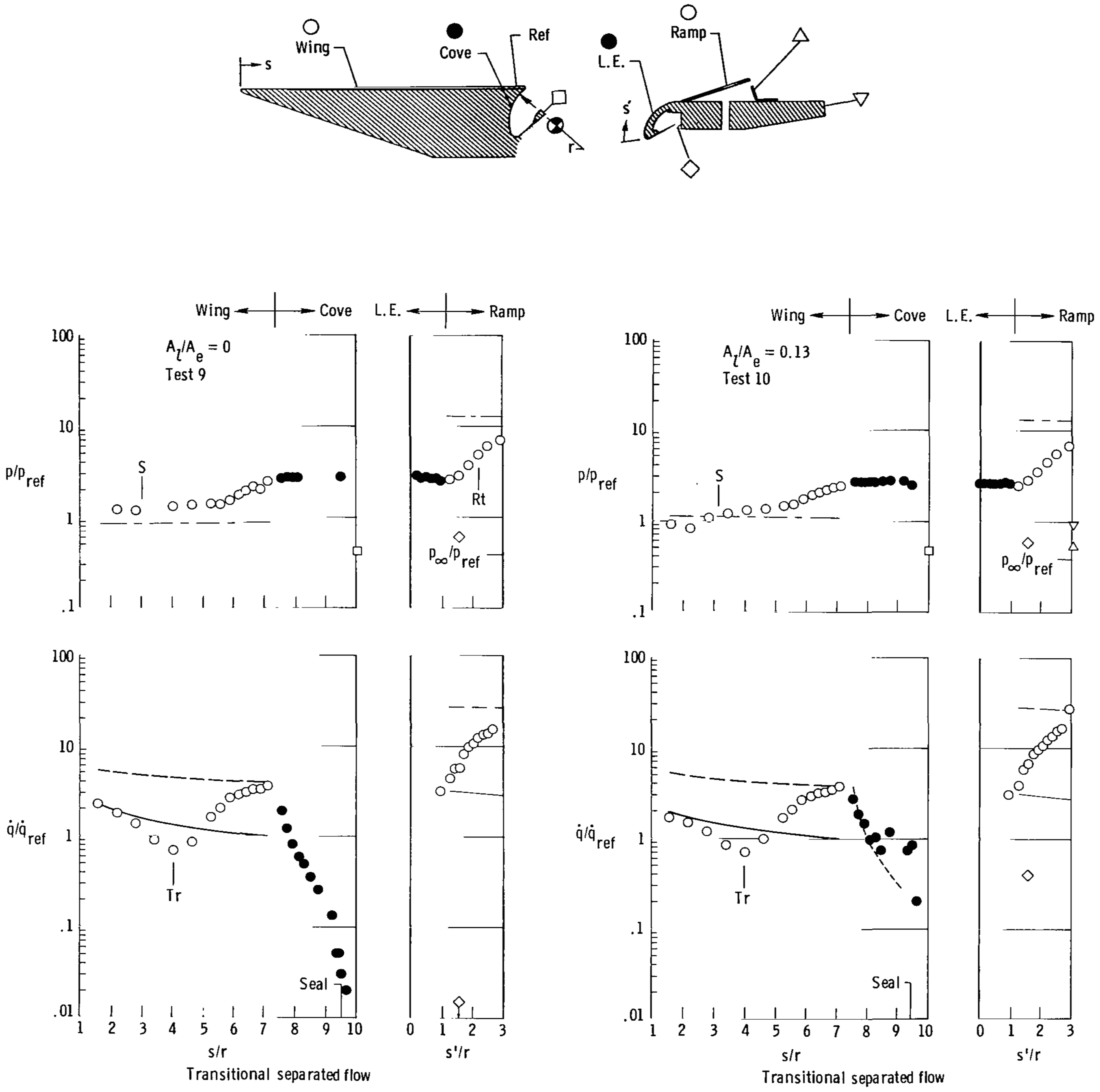

(c) $\delta = 25^{\circ}$.

Figure 13.- Continued.

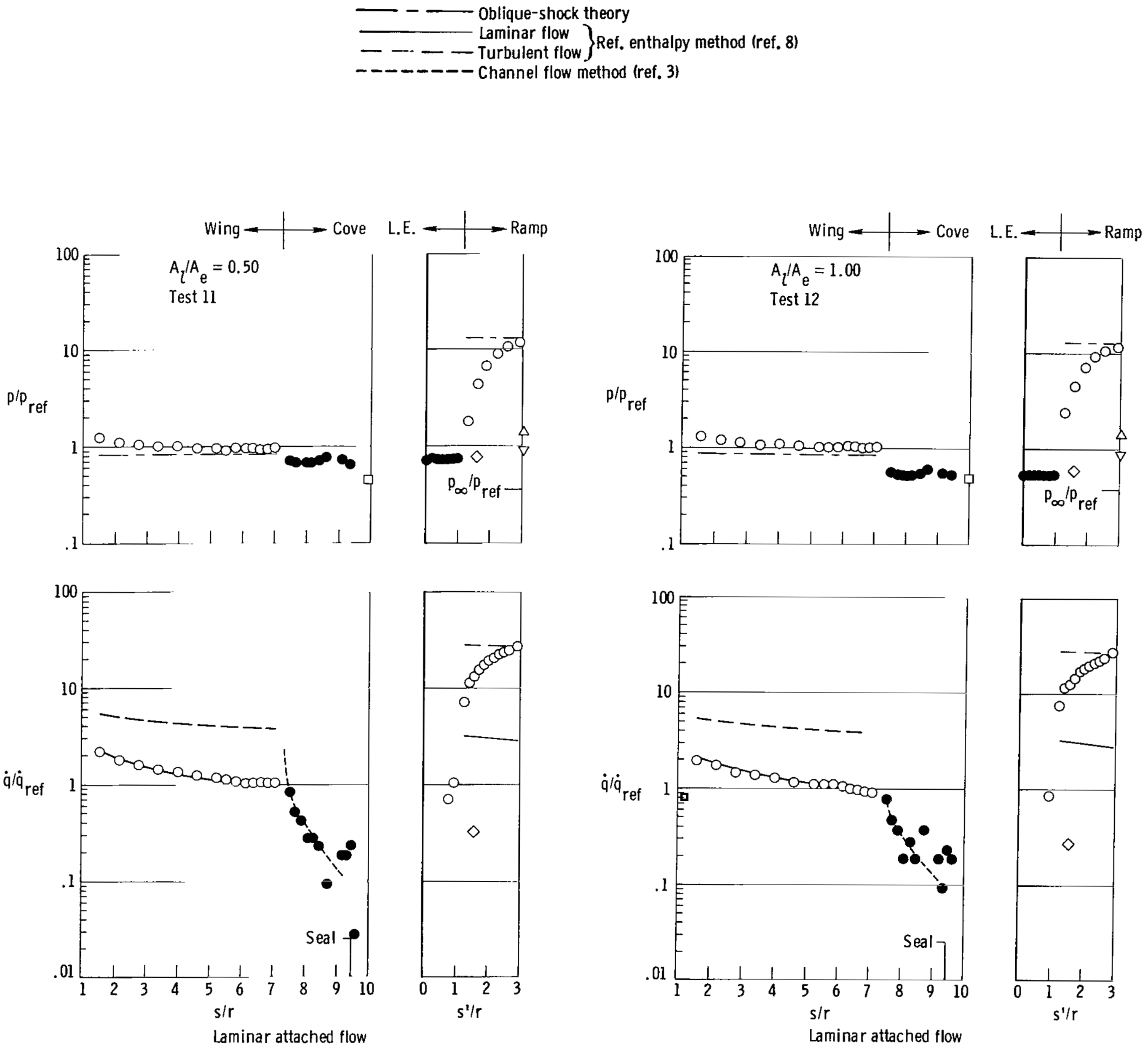

(c) $\delta = 25^\circ$.

Figure 13.- Continued.

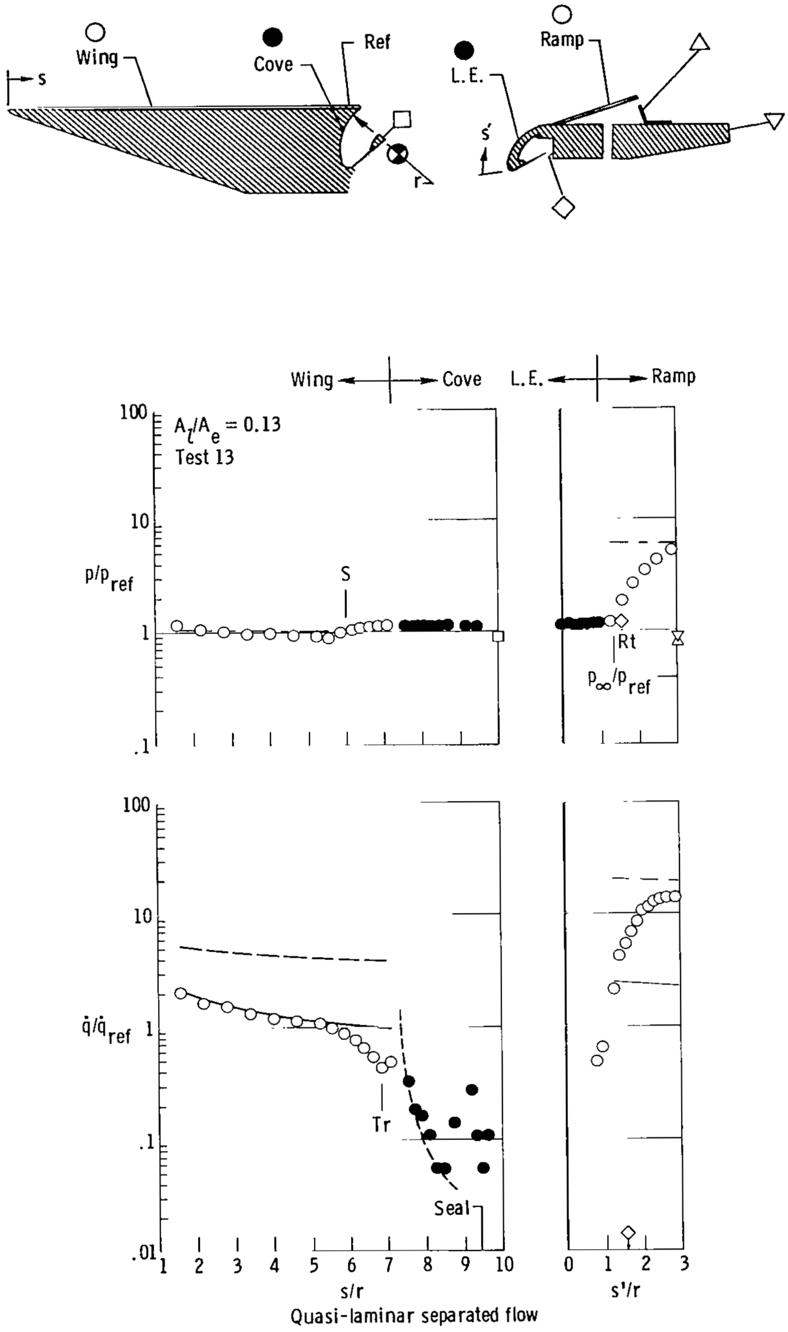

(d) δ = 15°.

Figure 13.- Concluded.

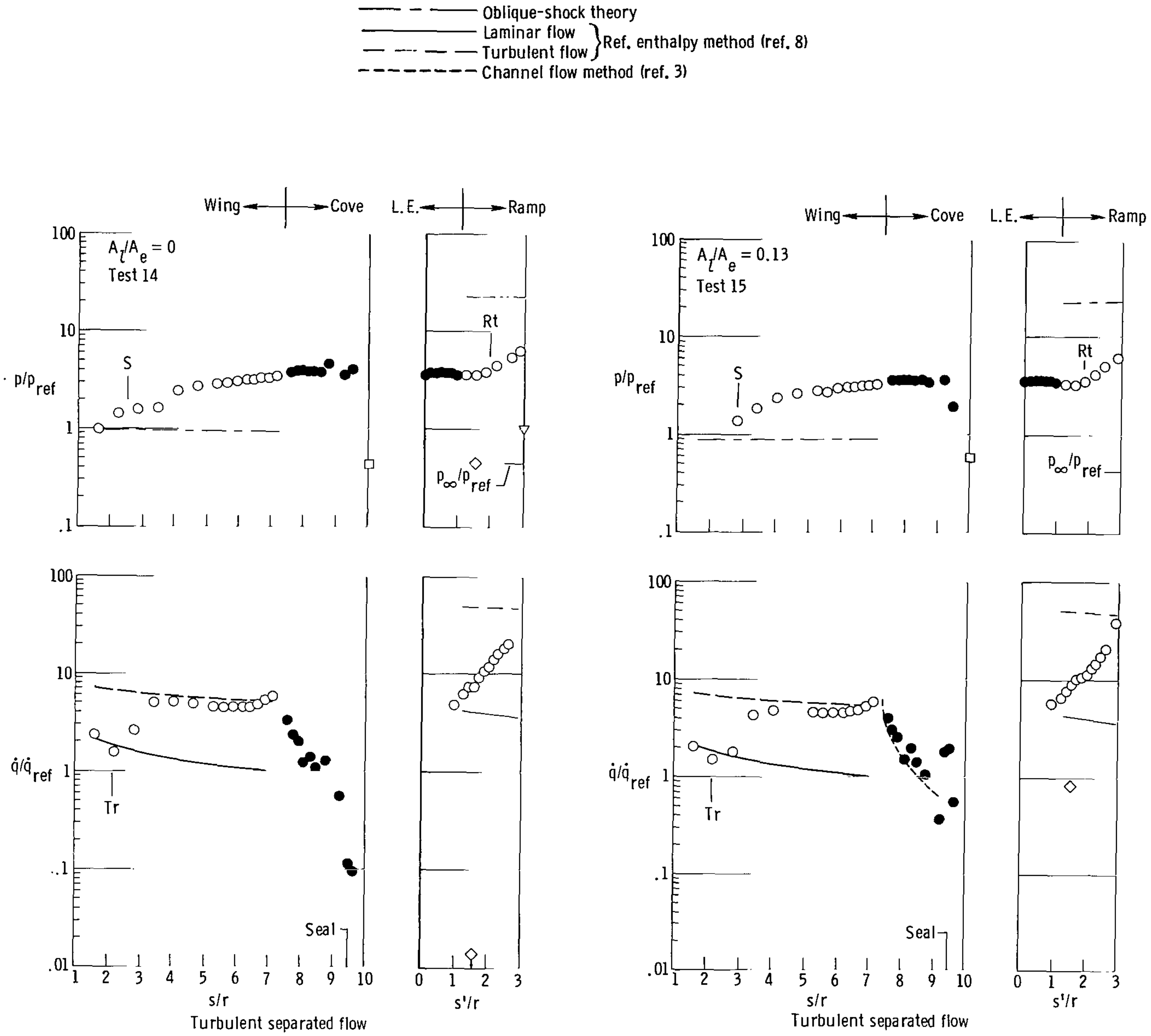

(a) $\delta = 35^\circ$.

Figure 14.- Centerline pressure and cold-wall heating-rate distributions at $N_{Re,\infty} \approx 1.00 \times 10^6$ ft^{-1} for various cove seal leak area ratios and ramp angles. $M_\infty \approx 6.9$; $T_t \approx 3360^\circ R$; $\alpha = 5^\circ$.

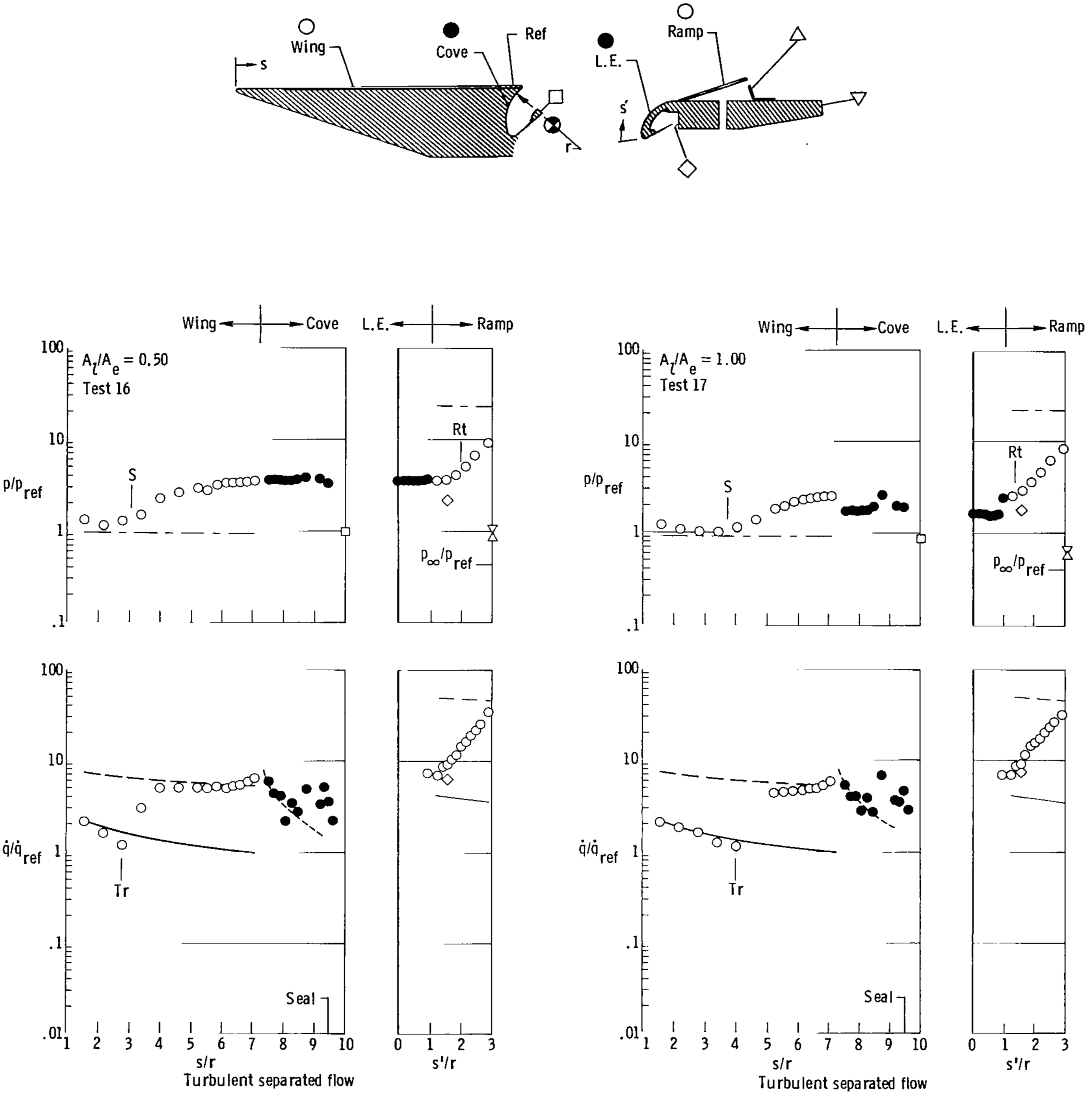

(a) δ = 35°.

Figure 14.- Continued.

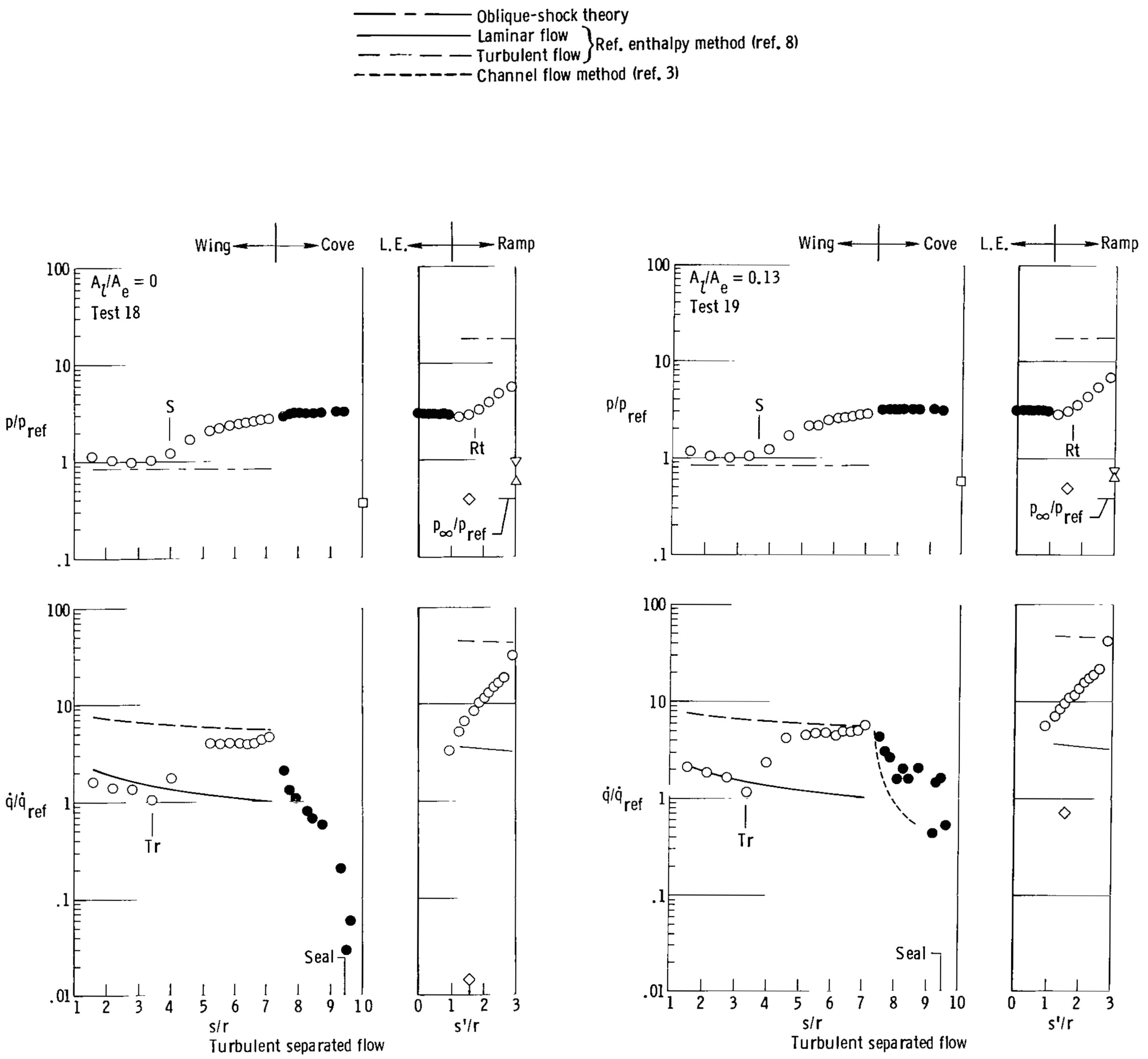

(b) $\delta = 30^{\circ}$.

Figure 14.- Continued.

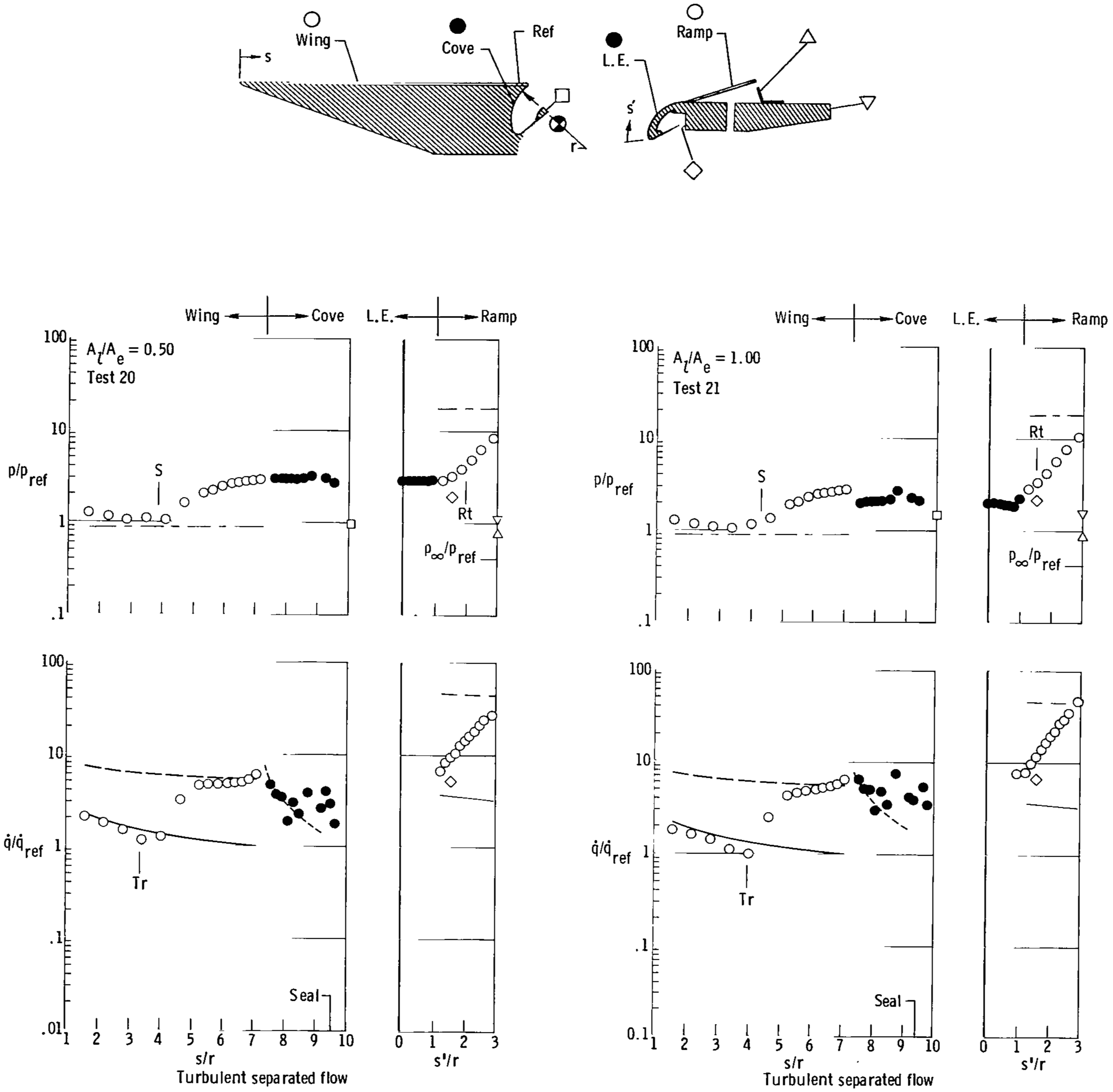

(b) $\delta = 30^\circ$.

Figure 14.- Continued.

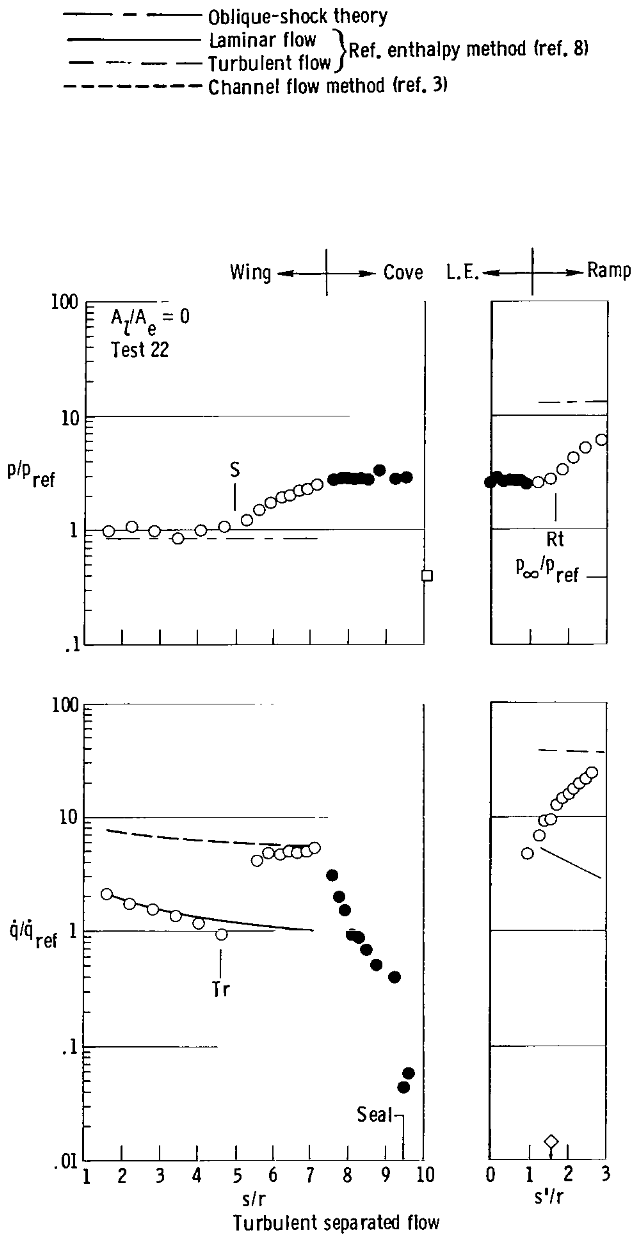

(c) $\delta = 25^\circ$.

Figure 14.- Continued.

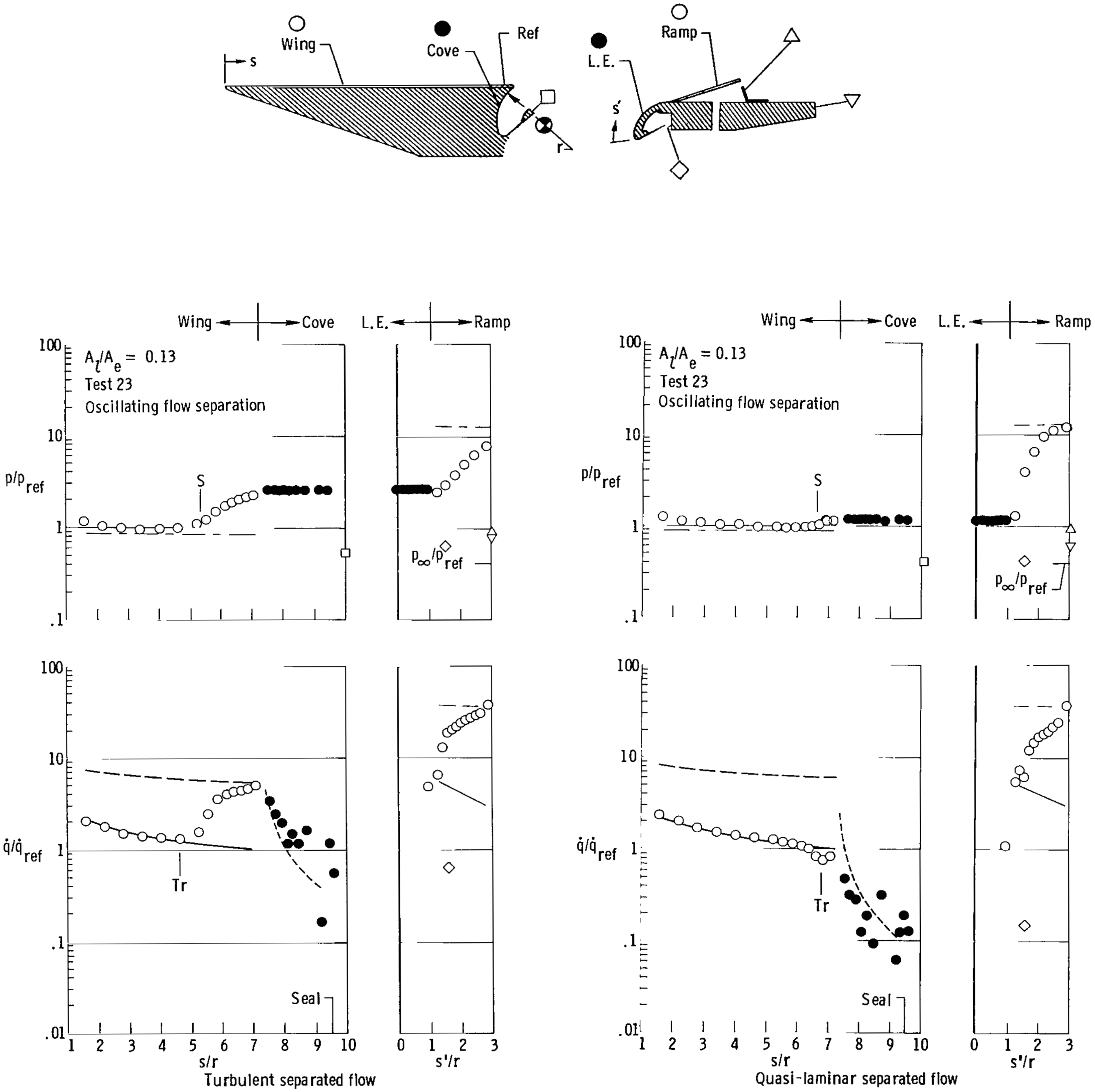

(c) $\delta = 25^\circ$.

Figure 14.- Continued.

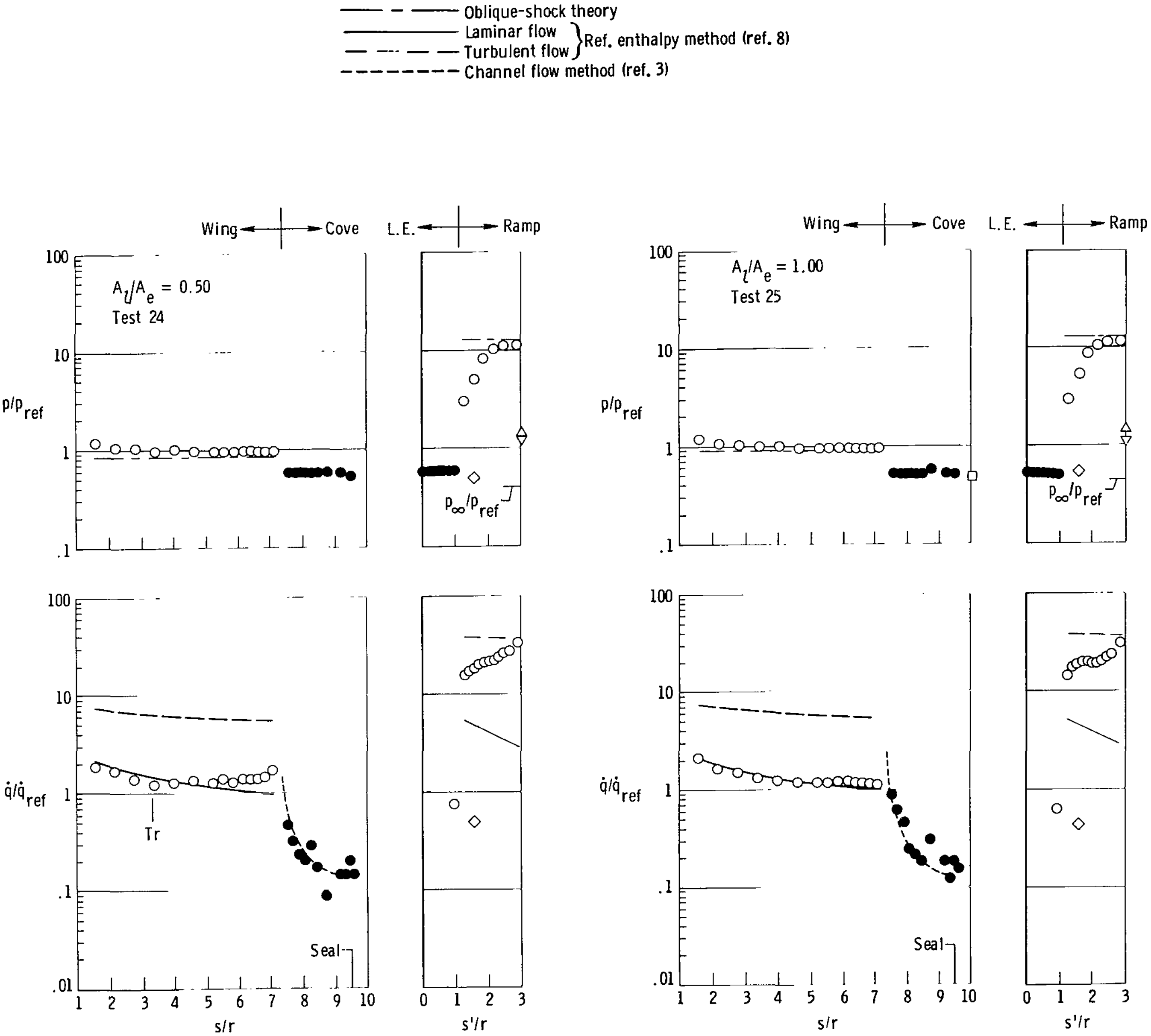

Transitional attached flow

Laminar attached flow

(c) $\delta = 25^{\circ}$.

Figure 14.- Continued.

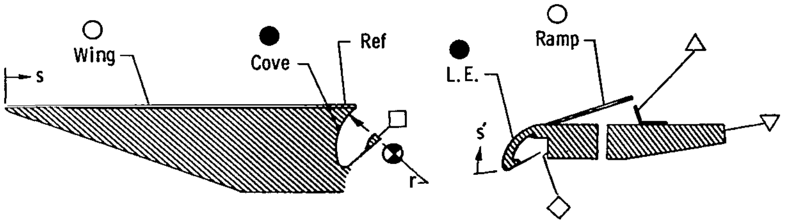

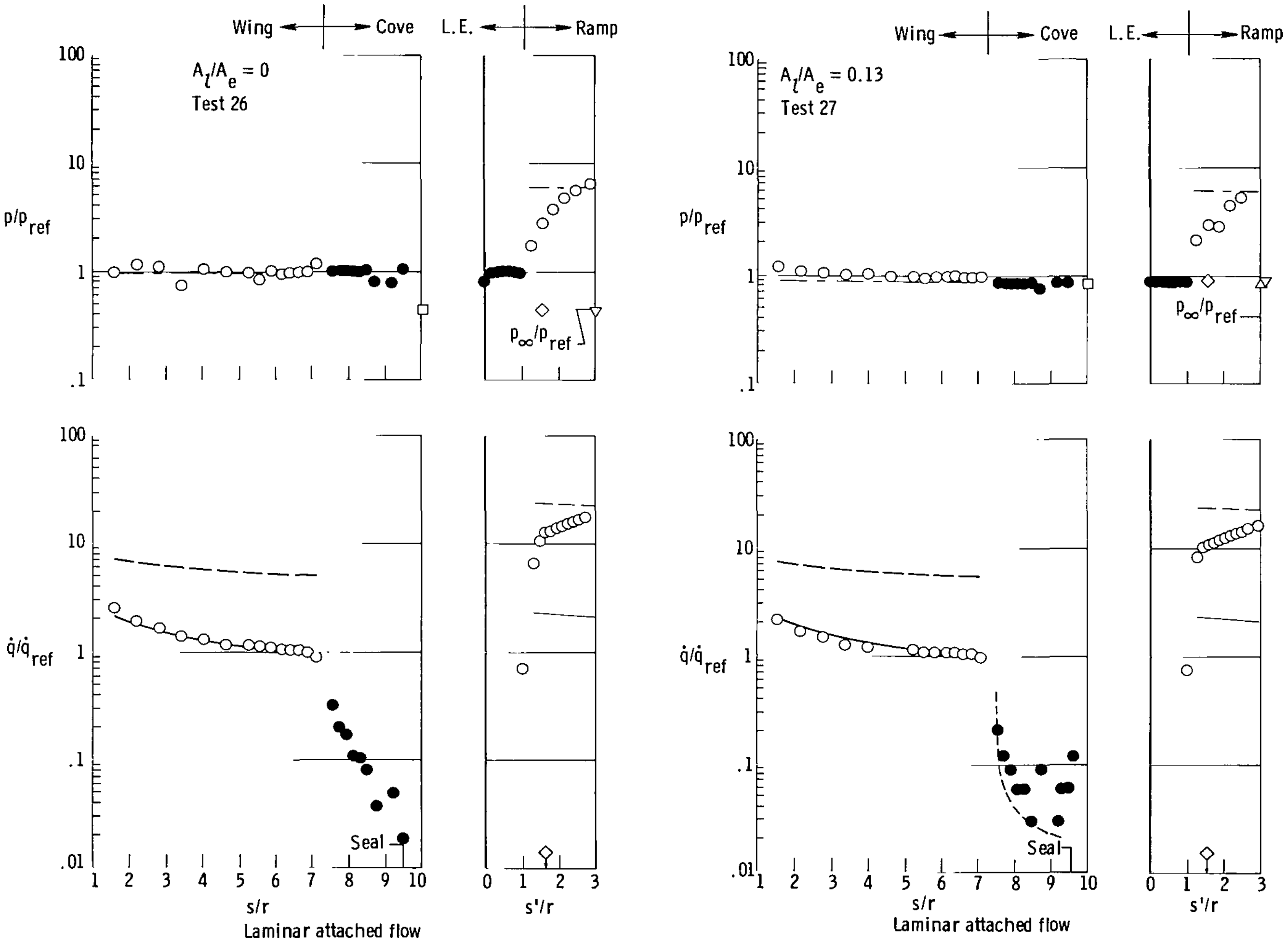

(d) $\delta = 15^{\circ}$.

Figure 14.- Concluded.

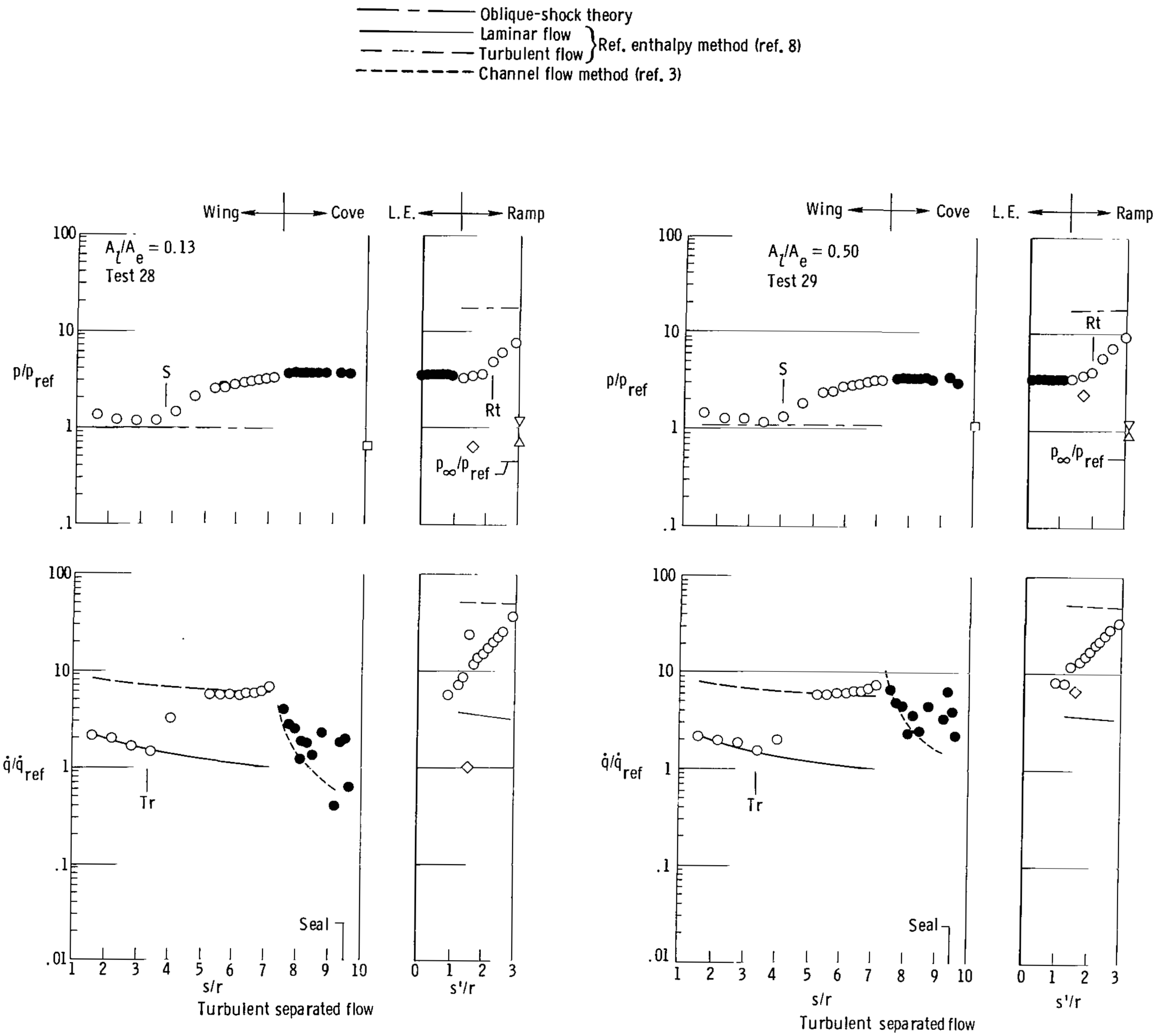

(a) $\delta = 30^\circ$.

Figure 15.- Centerline pressure and cold-wall heating-rate distributions at $N_{Re,\infty} \approx 1.38 \times 10^6$ ft^{-1} for various cove seal leak area ratios and ramp angles. $M_\infty \approx 6.9$; $T_t \approx 3360^\circ$R; $\alpha = 5^\circ$.

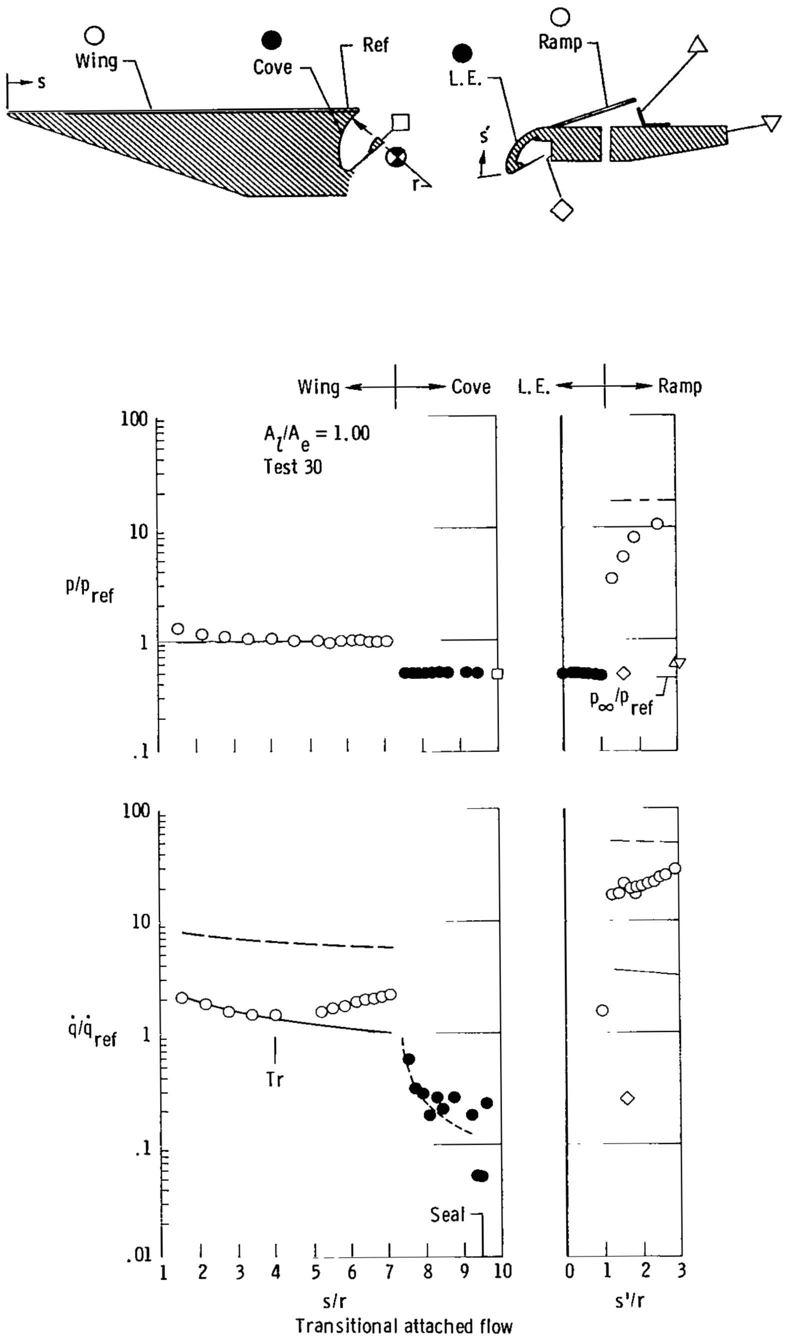

(a) δ = 30°.

Figure 15.- Continued.

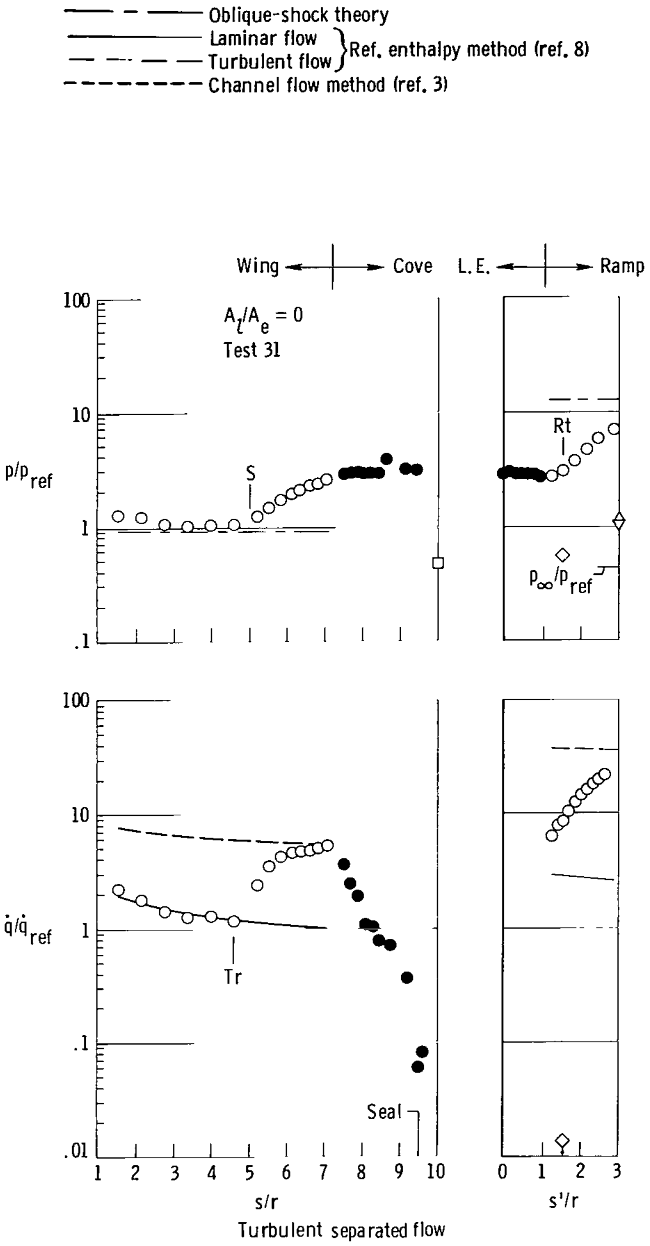

(b) $\delta = 25^\circ$.

Figure 15.- Continued.

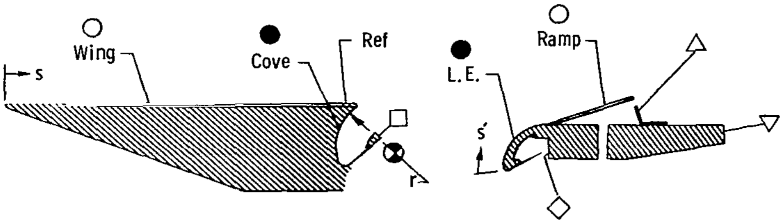

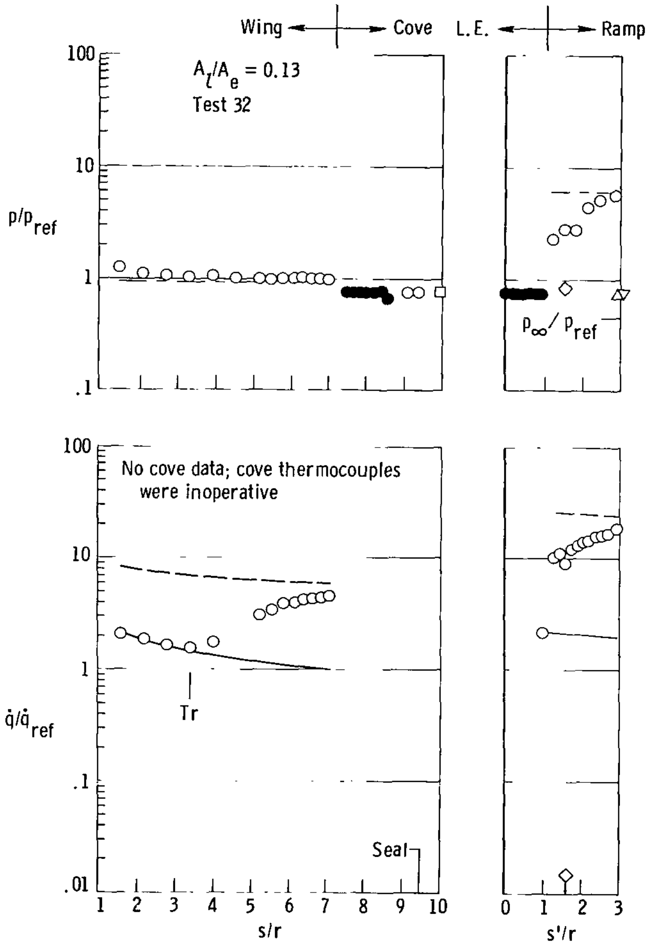

Transitional attached flow

(c) $\delta = 15^\circ$.

Figure 15.- Concluded.

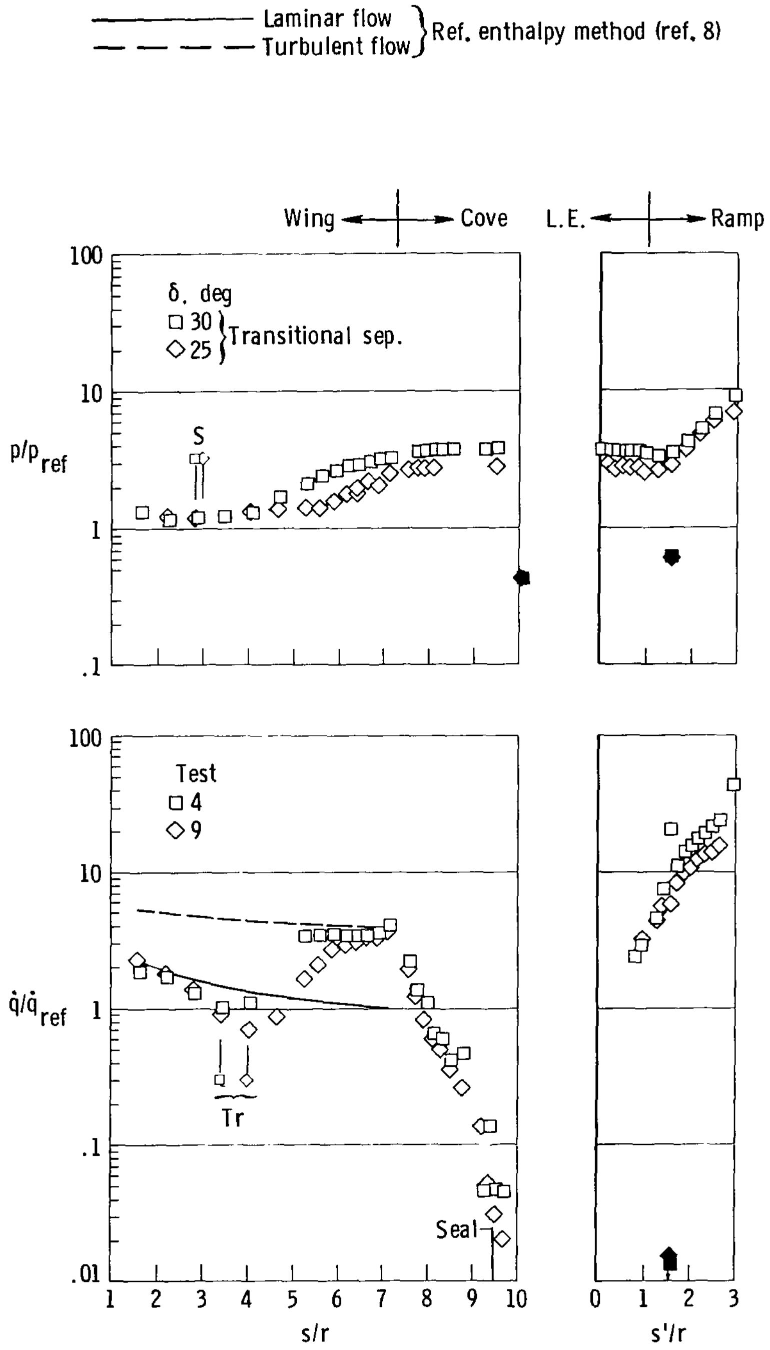

(a) $A_l/A_e = 0$.

Figure 16.- Effect of ramp angle on centerline pressures and cold-wall heating rates. $M_\infty \approx 6.9$; $T_t \approx 3360^\circ R$; $N_{Re,\infty} \approx 0.35 \times 10^6 \text{ ft}^{-1}$; $\alpha = 5^\circ$.

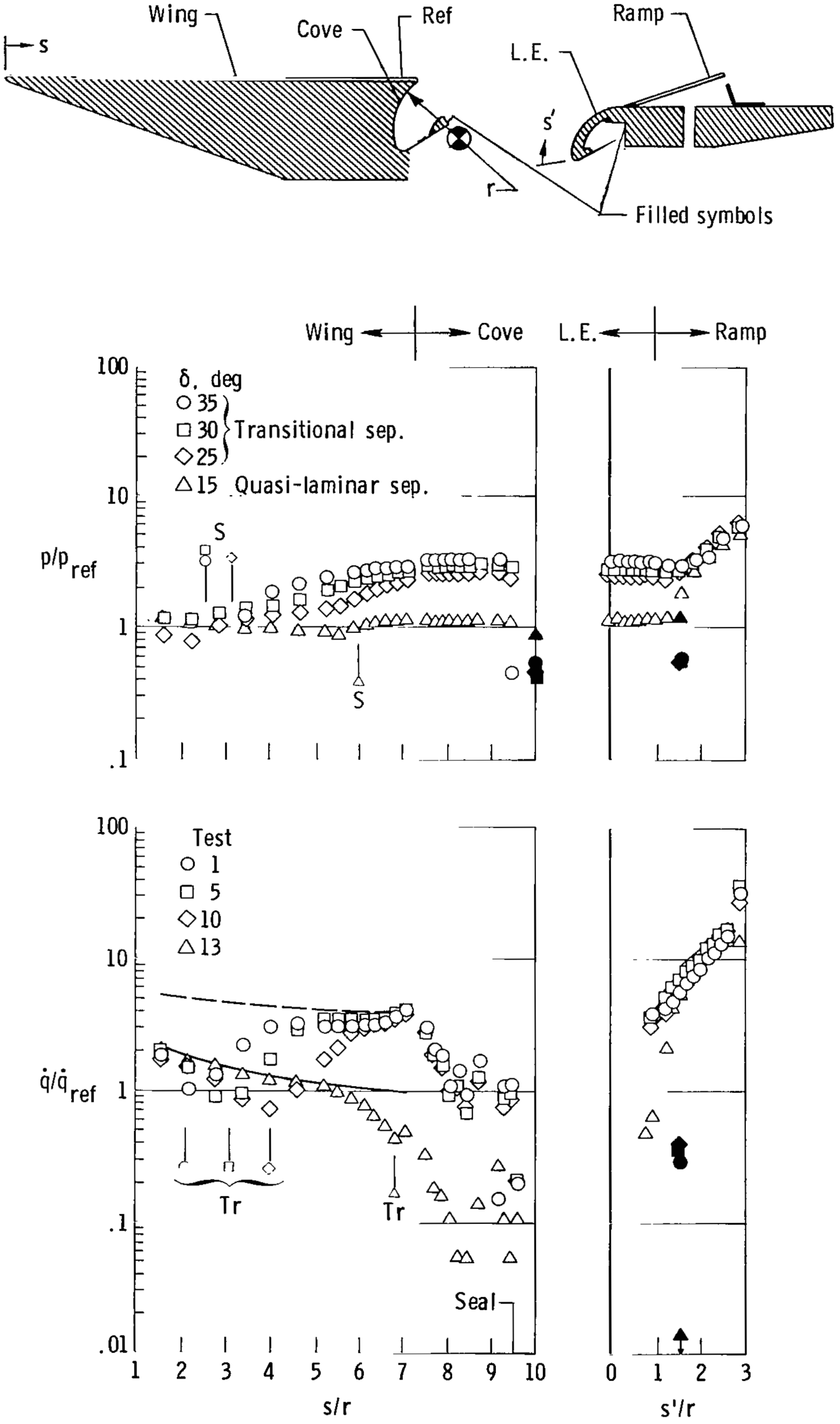

(b) $A_l/A_e = 0.13$.

Figure 16.- Continued.

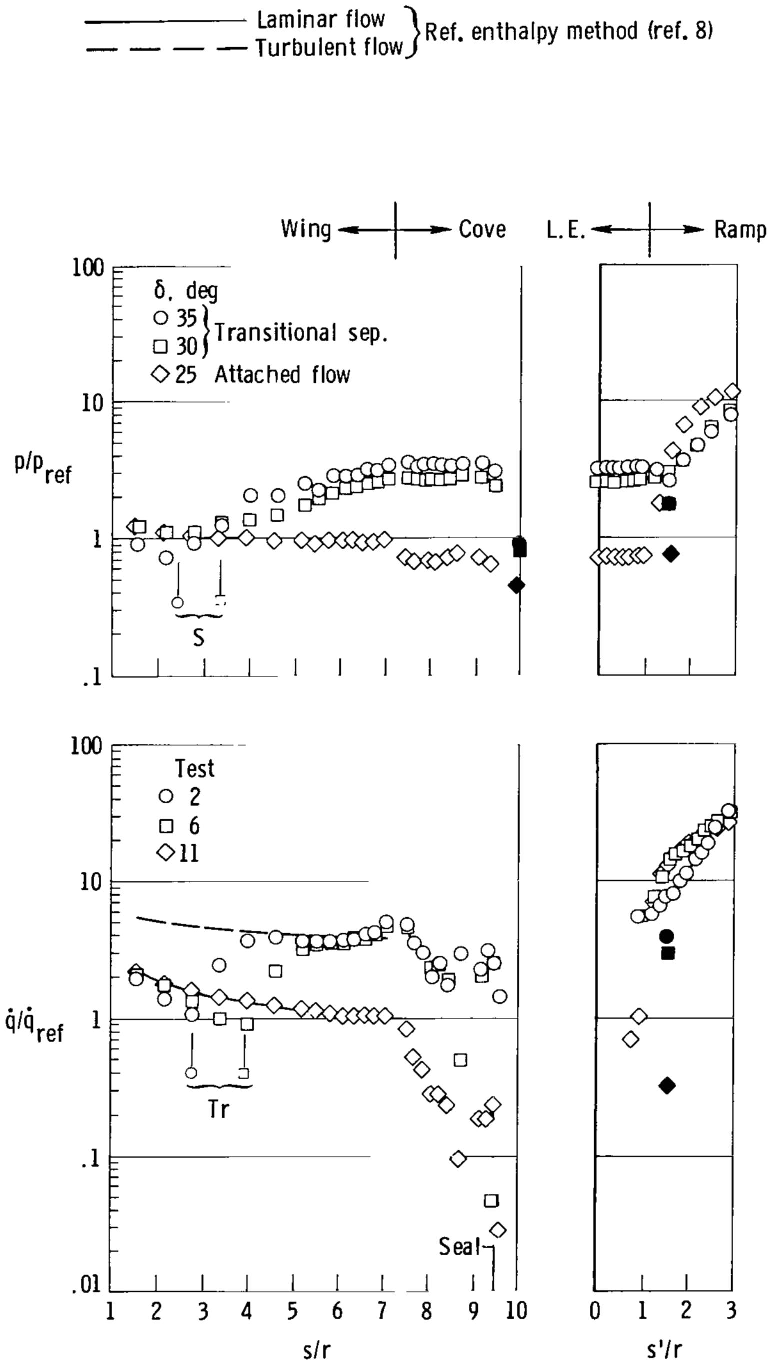

(c) $A_l/A_e = 0.50$.

Figure 16.- Continued.

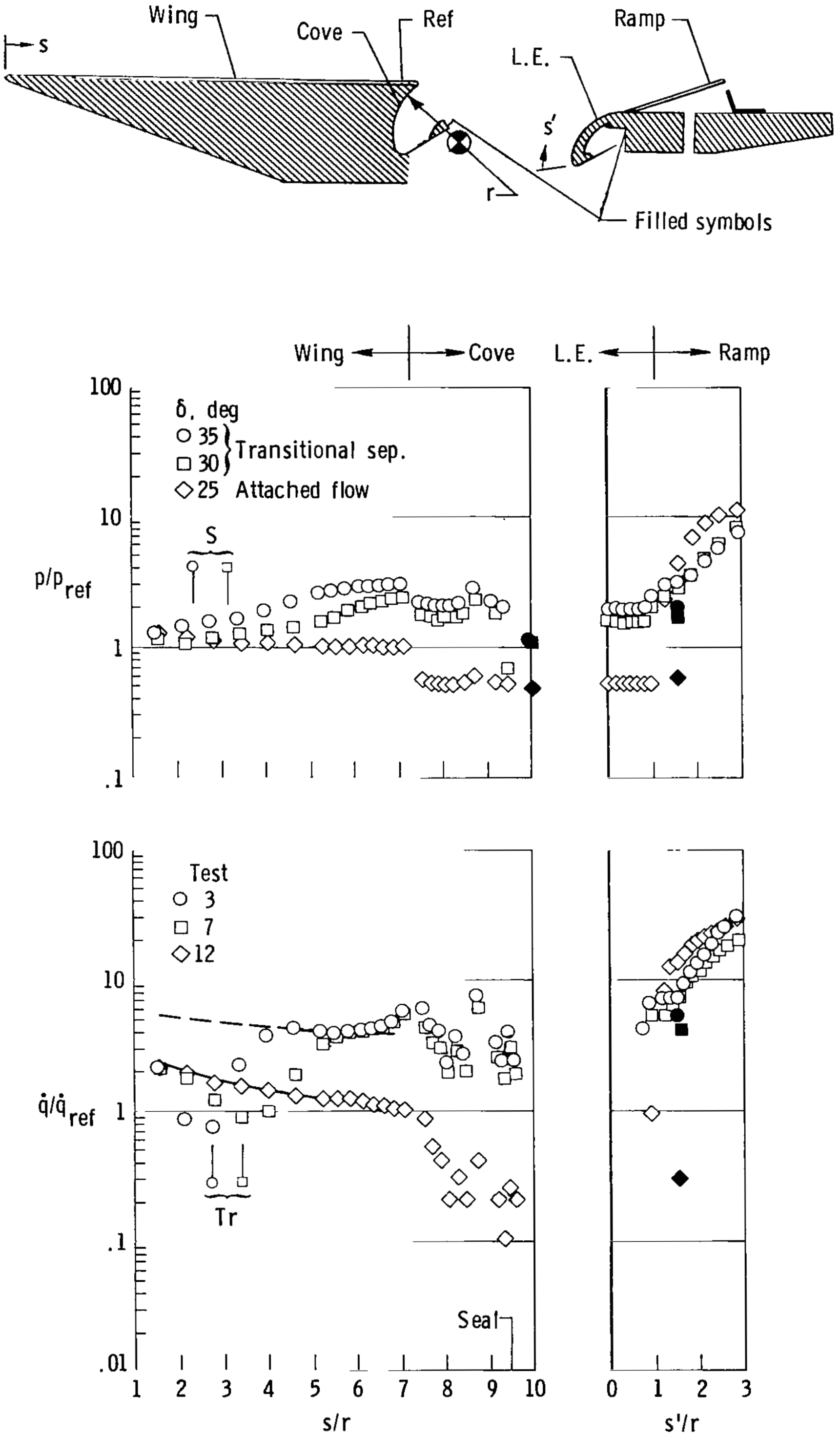

(d) $A_l/A_e = 1.00$.

Figure 16.- Concluded.

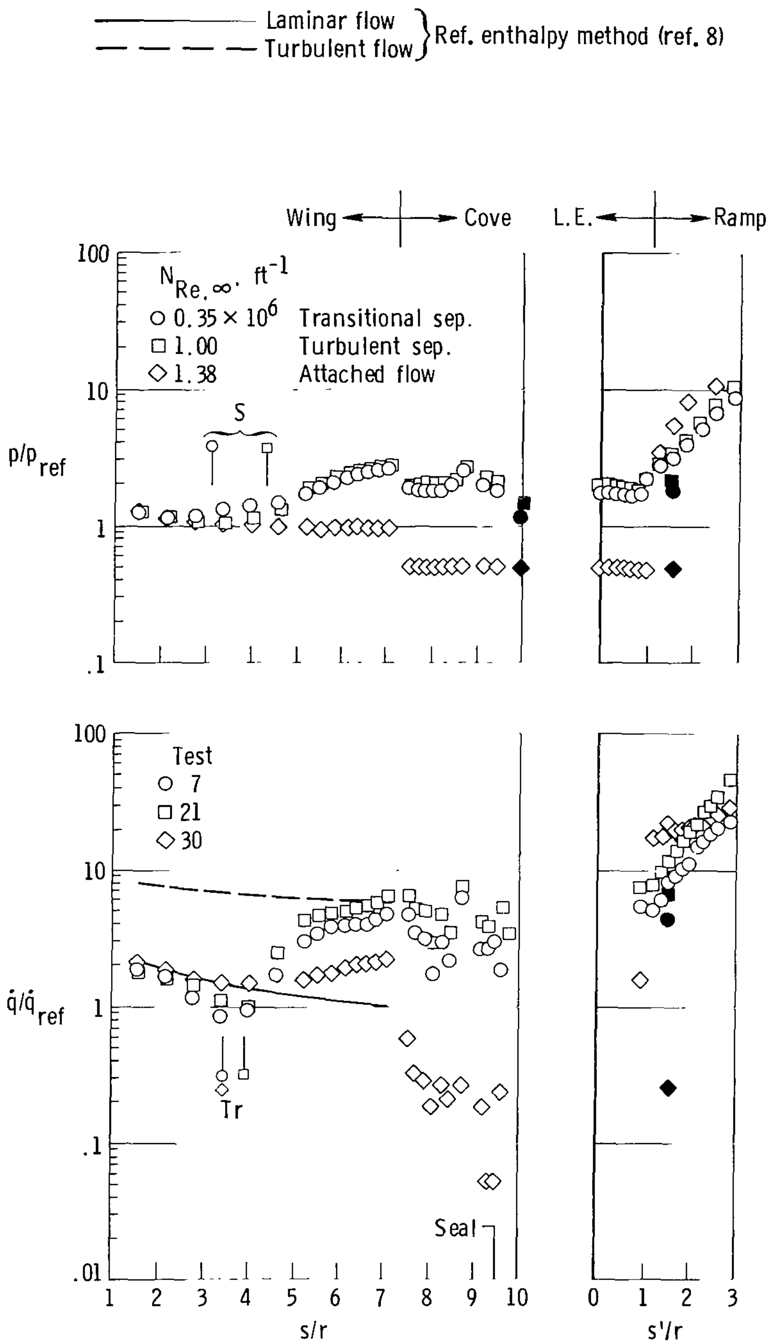

Figure 17.- Effect of free-stream unit Reynolds number on centerline pressures and cold-wall heating rates. $M_{\infty} \approx 6.9$; $T_t \approx 3360^{\circ}R$; $\alpha = 5^{\circ}$; $\delta = 30^{\circ}$; $A_l/A_e = 1.00$.

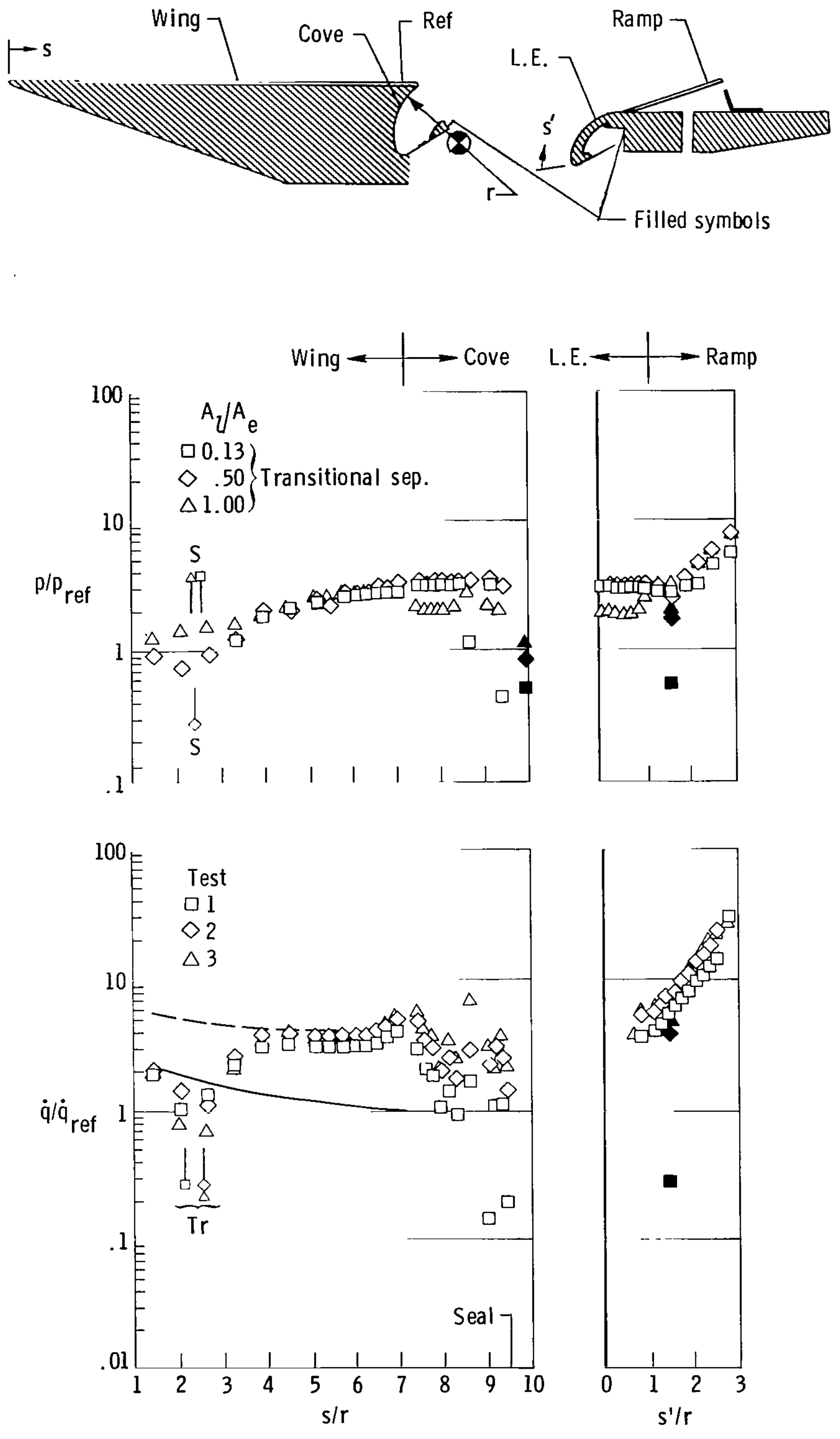

(a) $\delta = 35^{\circ}$.

Figure 18.- Effect of cove seal leak area ratio on centerline pressures and cold-wall heating rates. $M_{\infty} \approx 6.9$; $T_t \approx 3360^{\circ}R$; $N_{Re,\infty} \approx 0.35 \times 10^{6}\ ft^{-1}$; $\alpha = 5^{\circ}$.

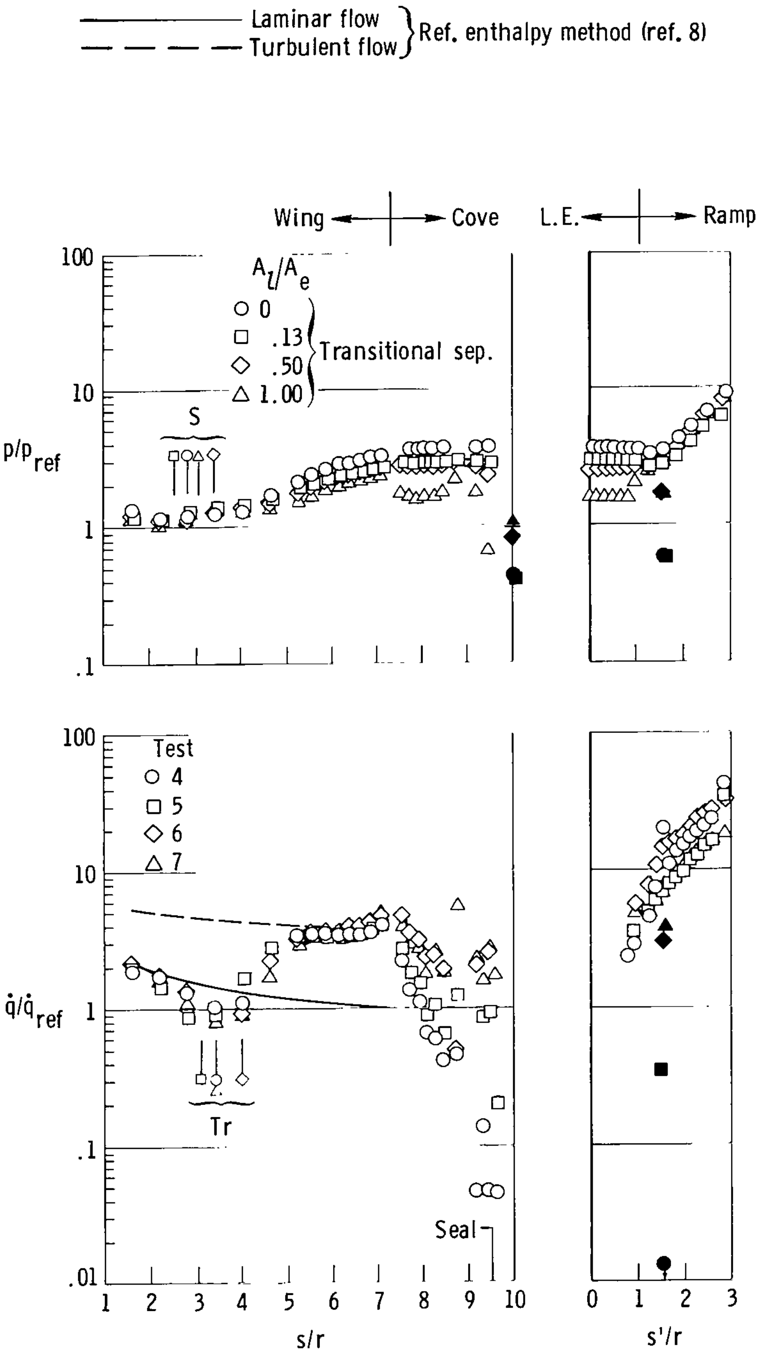

(b) $\delta = 30^{\circ}$.

Figure 18.- Continued.

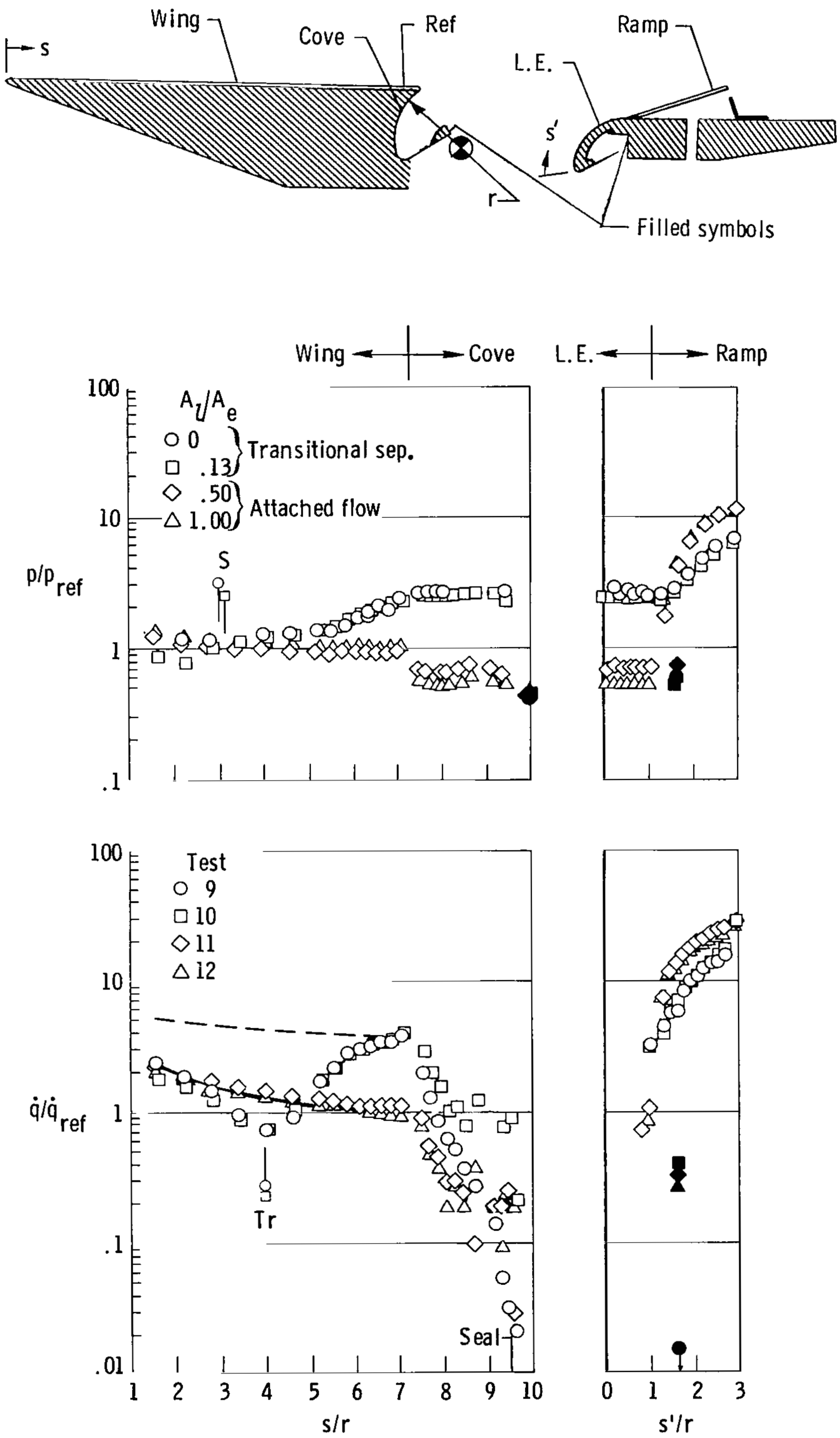

(c) $\delta = 25^{\circ}$.

Figure 18.- Concluded.

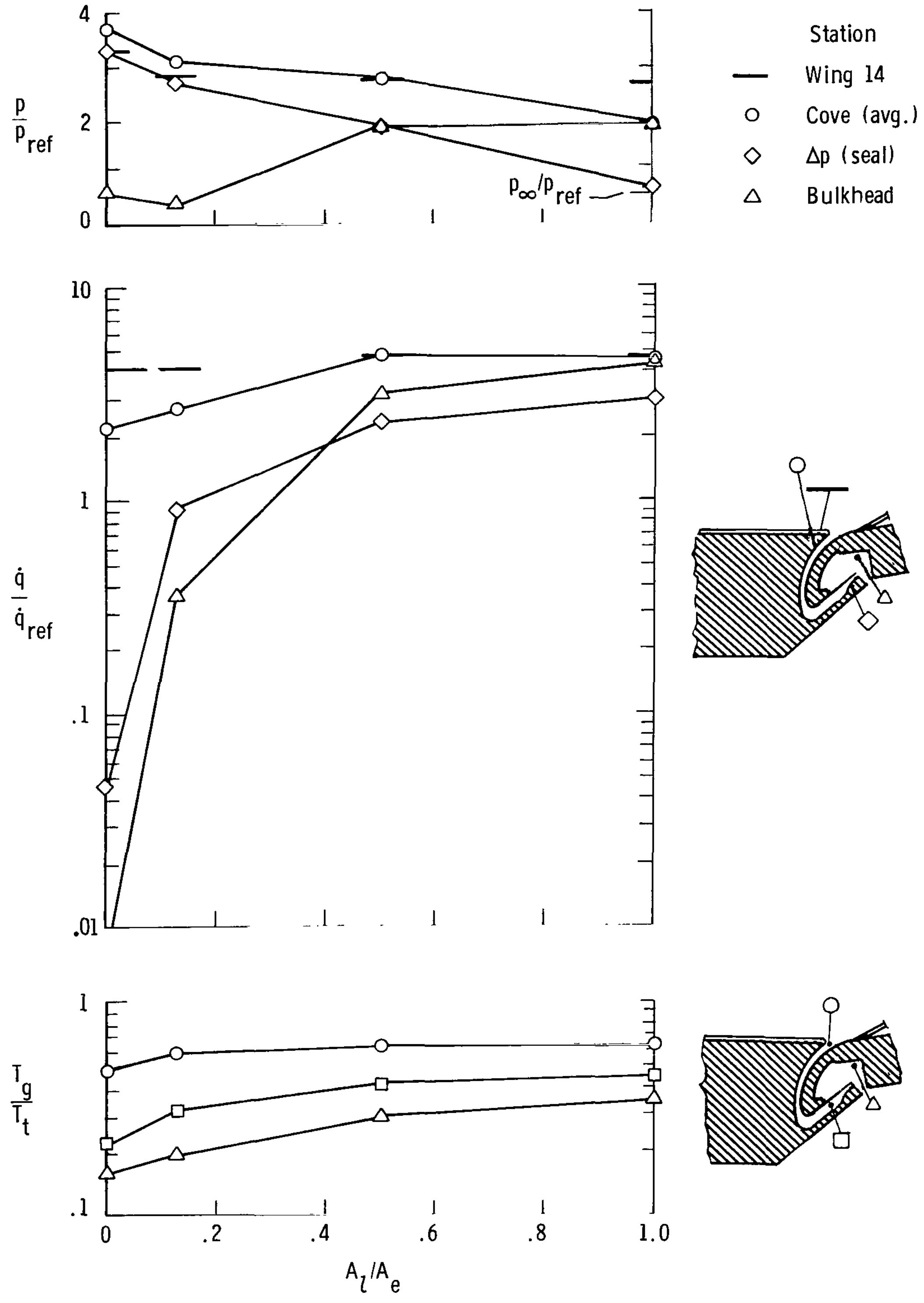

(a) $\delta = 30^{\circ}$.

Figure 19.- Effect of cove seal leak area ratio on pressures, cold-wall heating rates, and gas temperatures in the cove and at the bulkhead. $M_{\infty} \approx 6.9$; $T_t \approx 3360^{\circ}R$; $\alpha = 5^{\circ}$; $N_{Re,\infty} \approx 0.35 \times 10^6$ ft^{-1}.

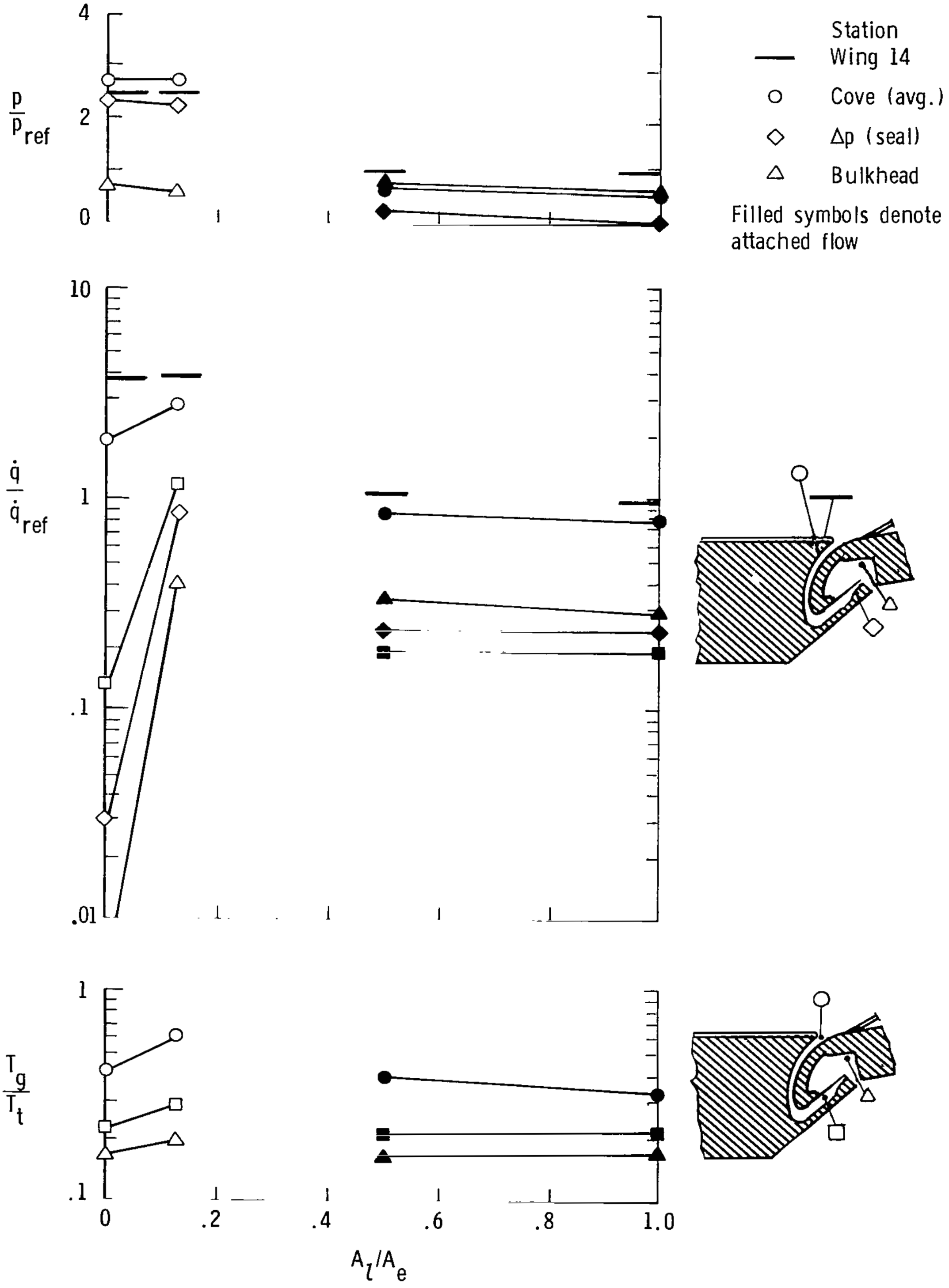

(b) $\delta = 25^{\circ}$.

Figure 19.- Concluded.

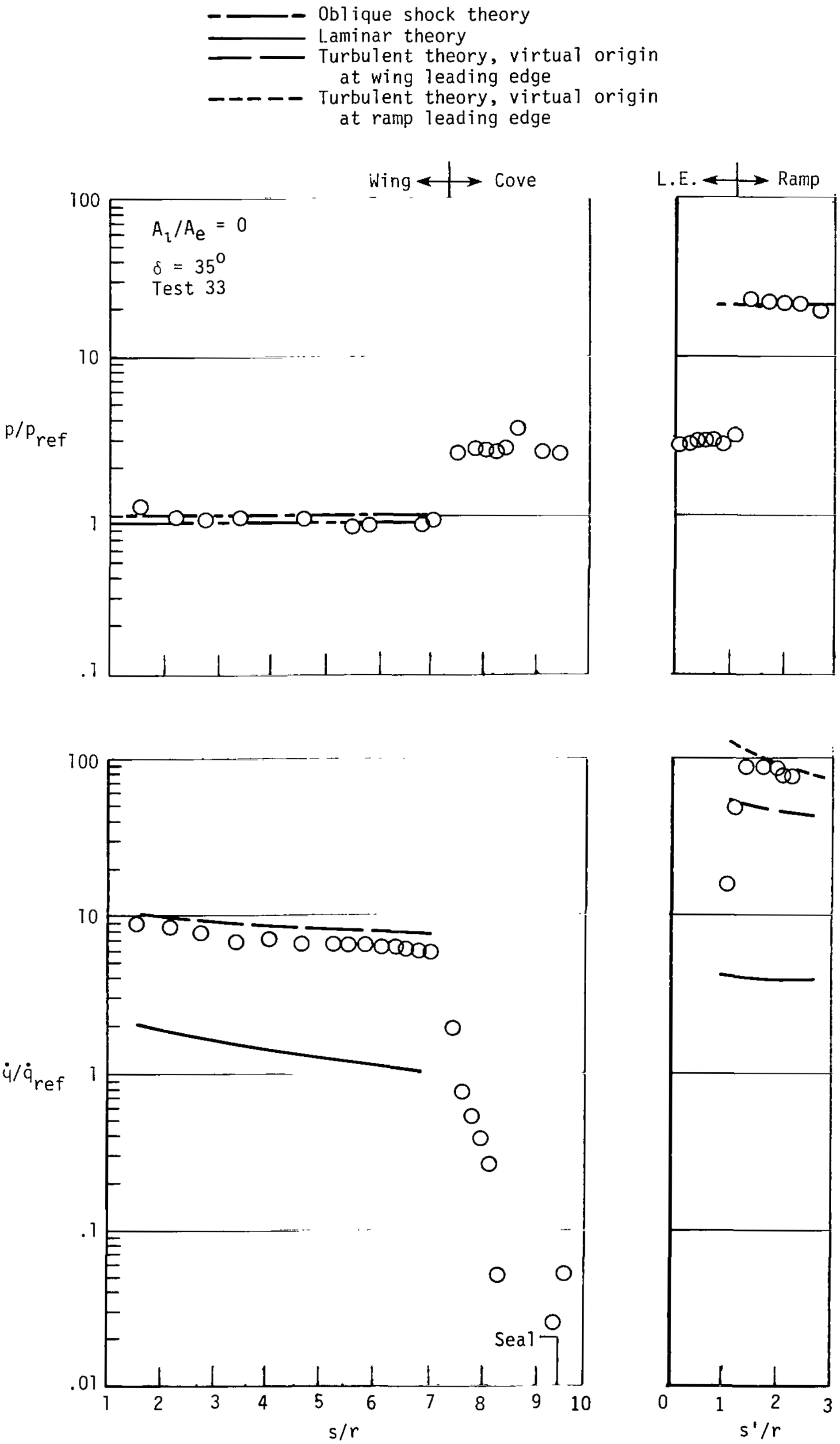

Figure 20.- Centerline pressure and cold-wall heating-rate distributions for a sharp, tripped leading edge with a turbulent boundary layer. $A_l/A_e = 0$; $M_\infty \approx 6.7$; $N_{Re,\infty} \approx 1.40 \times 10^6$ ft^{-1}; $T_t = 3264^oR$; $\alpha = 5^o$; $\delta = 35^o$.

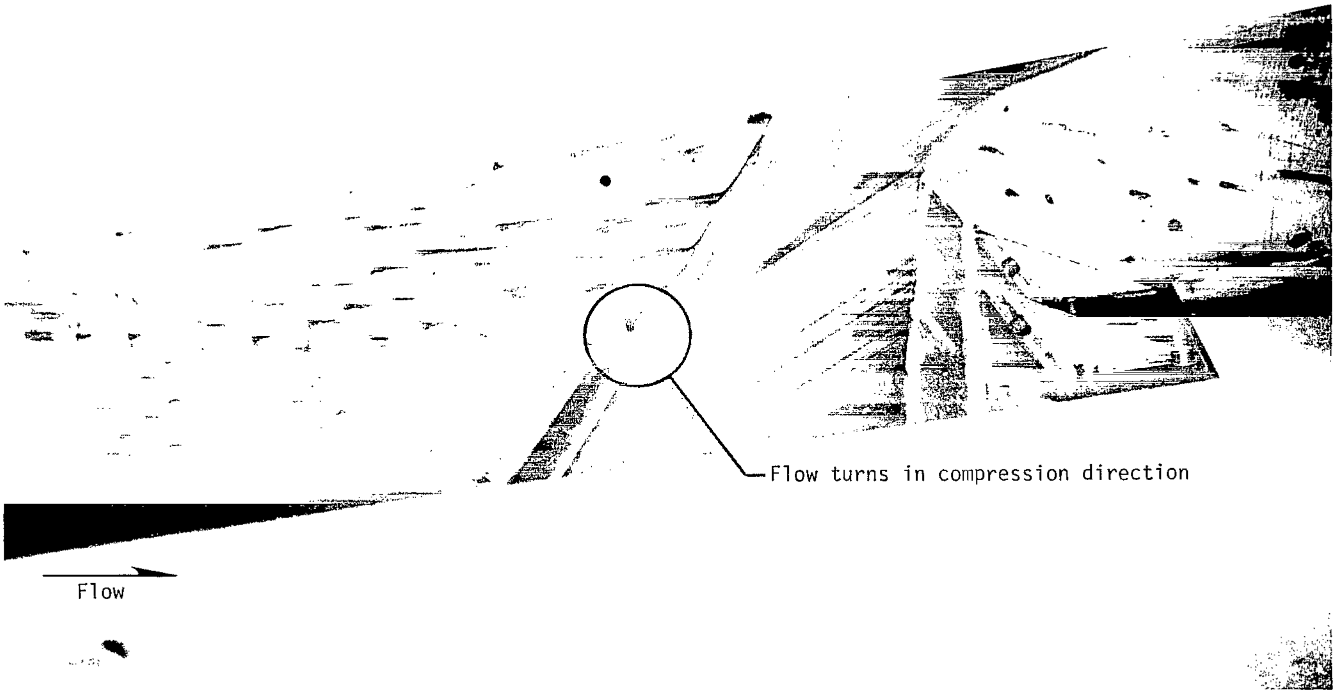

L-79-8073.1

Figure 21.- Oil-flow pattern on aerodynamic fence for turbulent attached flow on wing. $\alpha = 5^\circ$; $\delta = 35^\circ$; $M_\infty \approx 6.7$; $N_{Re,\infty} \approx 1.40 \times 10^6 \text{ ft}^{-1}$; $A_l/A_e = 0$.

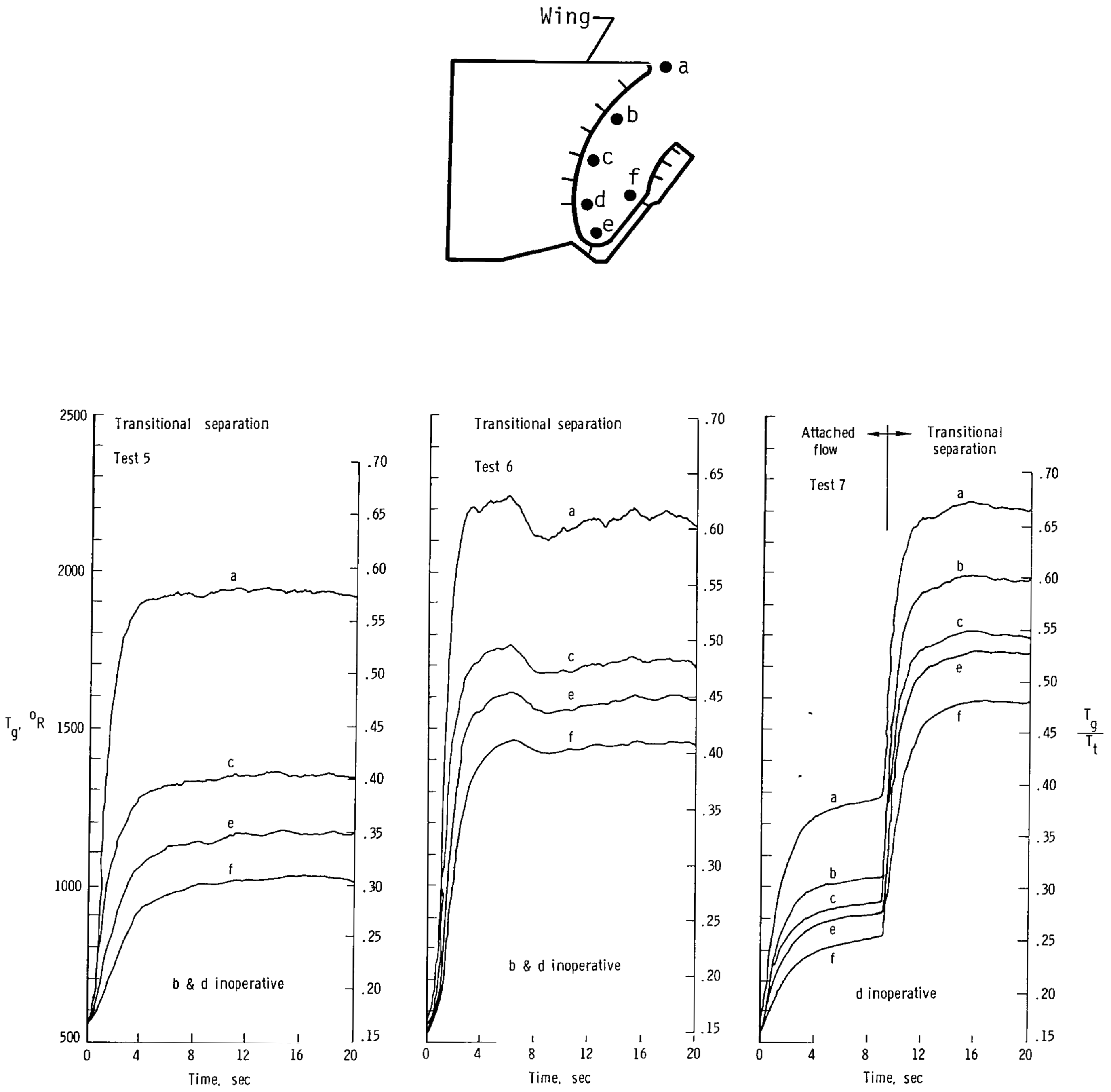

(a) $A_l/A_e = 0.13$. (b) $A_l/A_e = 0.50$. (c) $A_l/A_e = 1.00$.

Figure 22.- Cove gas temperature response to separated and attached flow conditions on wing at cove entrance. $M_\infty \approx 6.9$; $N_{Re,\infty} \approx 0.35 \times 10^6$ ft^{-1}; $\alpha = 5^\circ$; $\delta = 30^\circ$.

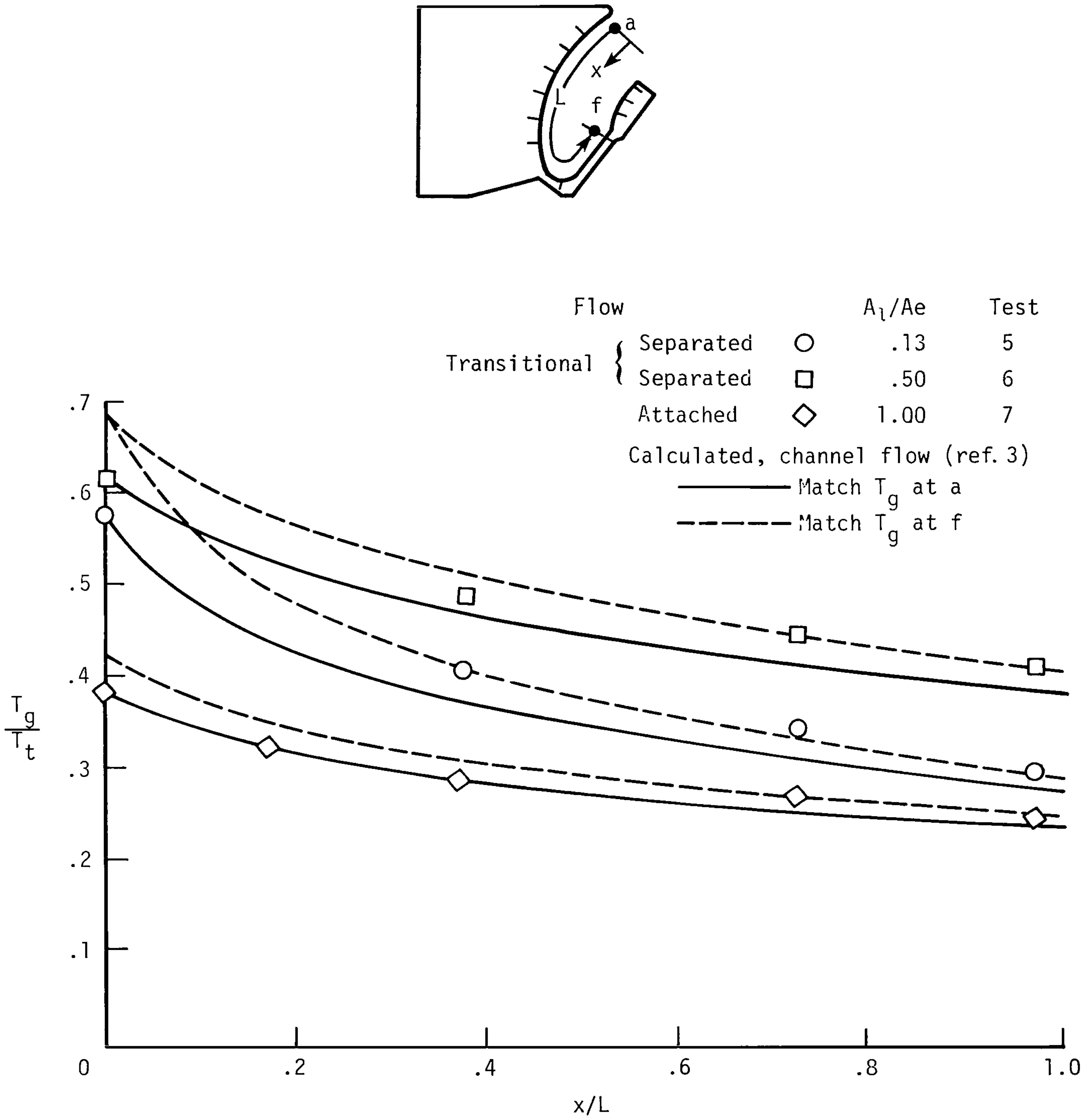

Figure 23.- Experimental and calculated cove gas temperature distributions. $M_\infty \approx 6.9$; $N_{Re,\infty} \approx 0.35 \times 10^6$ ft^{-1}; $\alpha = 5^\circ$; $\delta = 30^\circ$.

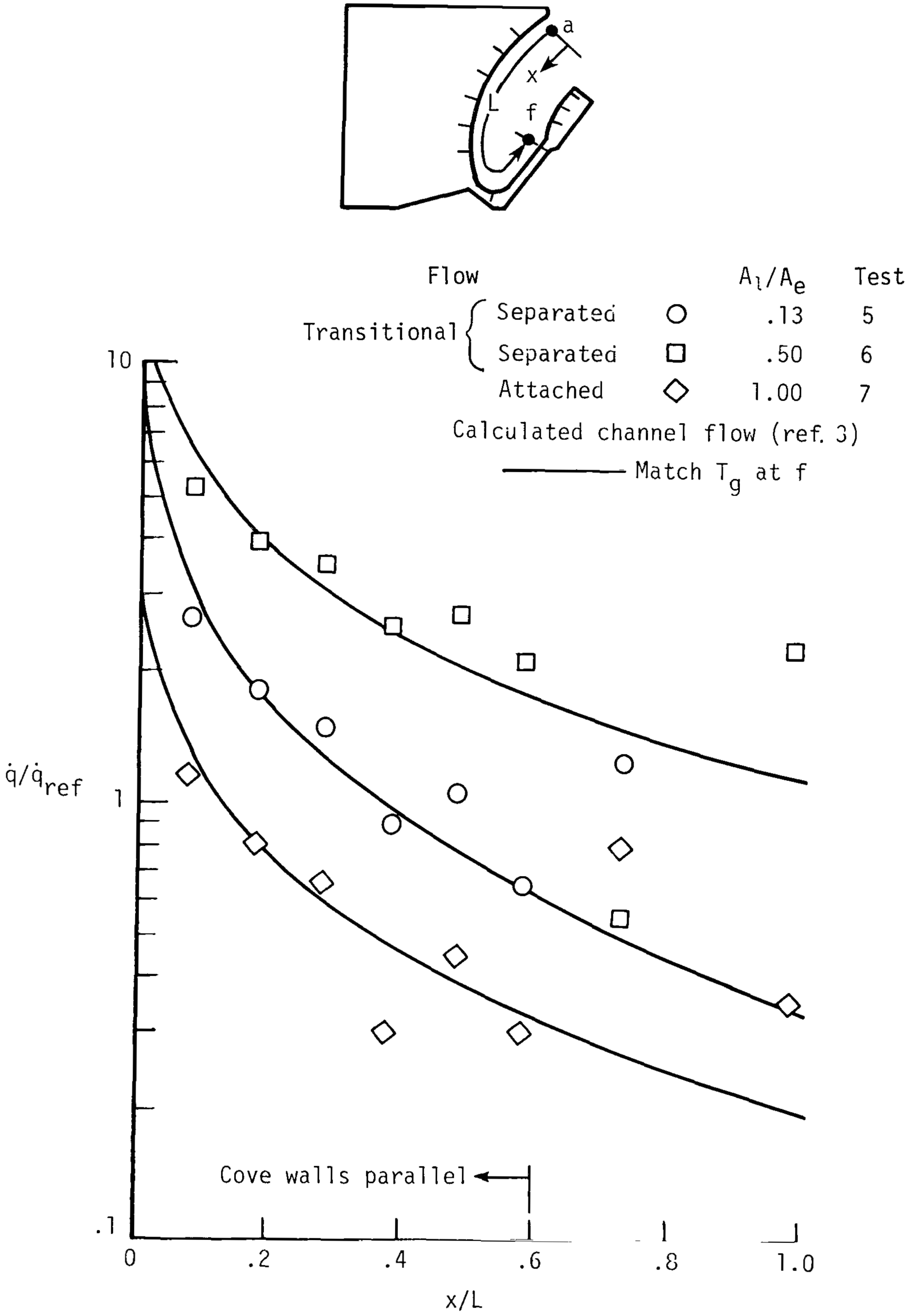

Figure 24.- Experimental and calculated cove cold-wall heating-rate distributions. $M_\infty \approx 6.9$; $T_t \approx 3360^\circ R$; $N_{Re,\infty} \approx 0.35 \times 10^6 \text{ ft}^{-1}$; $\alpha = 5^\circ$; $\delta = 30^\circ$.

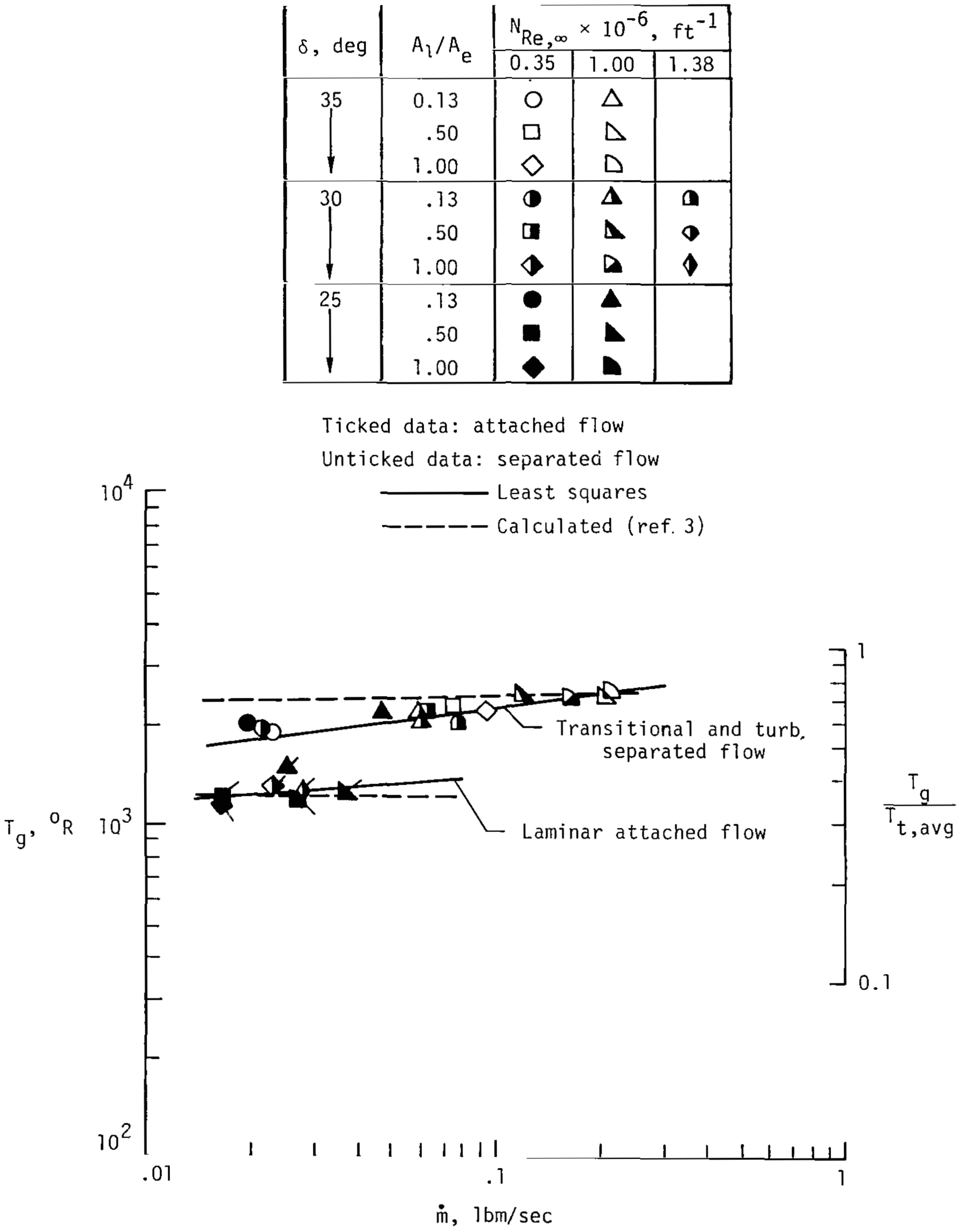

(a) At cove entrance.

Figure 25.- Cove gas temperature as a function of cove mass-flow rate. $M_\infty \approx 6.9$; $T_t \approx 3360^\circ R$; $\alpha = 5^\circ$.

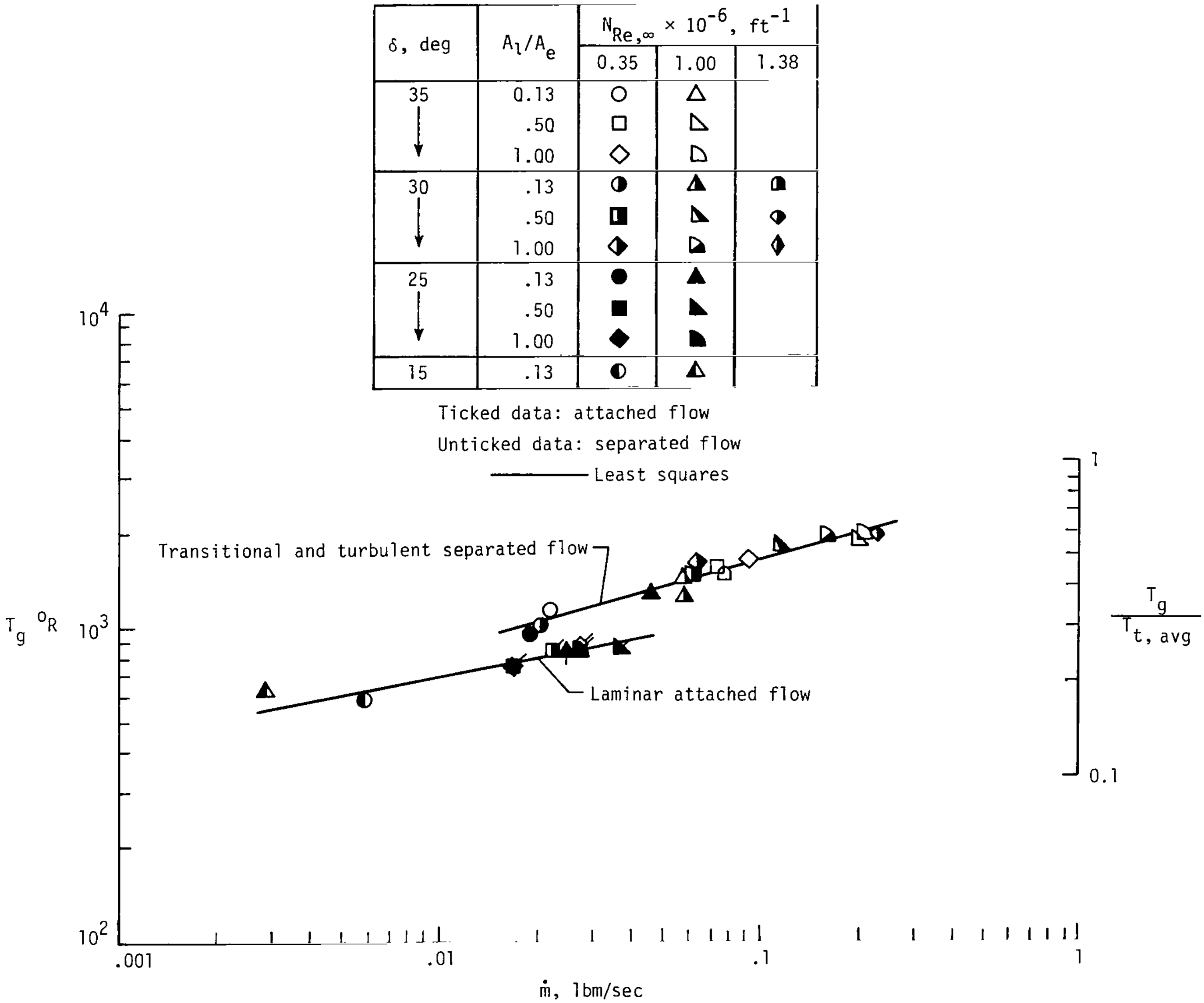

(b) Near seal.

Figure 25.- Concluded.

1. Report No. NASA TP-2127	2. Government Accession No.	3. Recipient's Catalog No.

4. Title and Subtitle EFFECTS OF FLOW SEPARATION AND COVE LEAKAGE ON PRESSURE AND HEAT-TRANSFER DISTRIBUTIONS ALONG A WING-COVE-ELEVON CONFIGURATION AT MACH 6.9	5. Report Date June 1983 6. Performing Organization Code 506-53-63-05
7. Author(s) William D. Deveikis	8. Performing Organization Report No. L-15513
9. Performing Organization Name and Address NASA Langley Research Center Hampton, VA 23665	10. Work Unit No. 11. Contract or Grant No.
12. Sponsoring Agency Name and Address National Aeronautics and Space Administration Washington, DC 20546	13. Type of Report and Period Covered Technical Paper 14. Sponsoring Agency Code

15. Supplementary Notes

16. Abstract

External and internal pressure and cold-wall heating-rate distributions were obtained in hypersonic flow on a full-scale heat-sink representation of the Space Shuttle orbiter wing-elevon-cove configuration. The purpose of the wind-tunnel experiments was to define effects of flow separation on cove aerothermal environment as a function of cove seal leak area (0, 13, 50, and 100 percent of cove entrance area), ramp angle (15°, 25°, 30°, and 35°), and free-stream unit Reynolds number (0.35×10^6, 1.00×10^6, and 1.38×10^6 per foot). Average free-stream Mach number from all tests was 6.9; average total temperature from all tests was 3360°R; free-stream dynamic pressure ranged from about 2 to 9 psi; and wing angle of attack was 5° (flow compression). For transitional and turbulent flow separation, increasing cove leakage progressively increased heating rates in the cove. When ingested mass flow was sufficient to force large reductions in extent of separation, increasing cove leakage reduced heating rates in the cove to those for laminar attached flow. Cove heating-rate distributions calculated with a method that assumed laminar developing channel flow agreed with experimentally obtained distributions within root-mean-square differences that varied between 11 and 36 percent where cove walls were parallel for leak areas of 50 and 100 percent.

17. Key Words (Suggested by Author(s)) Control-surface cove leakage Attached and separated flow Heat transfer Pressure Laminar and turbulent flow Aerothermal analysis	18. Distribution Statement Unclassified - Unlimited Subject Category 34

19. Security Classif. (of this report) Unclassified	20. Security Classif. (of this page) Unclassified	21. No. of Pages 93	22. Price A05

For sale by the National Technical Information Service, Springfield, Virginia 22161

NASA-Langley, 1983

National Aeronautics and
Space Administration

Washington, D.C.
20546

Official Business
Penalty for Private Use, $300

THIRD-CLASS BULK RATE

Postage and Fees Paid
National Aeronautics and
Space Administration
NASA-451

U.S.MAIL

1 1 1U,D, 830620 S00903DS
DEPT OF THE AIR FORCE
AF WEAPONS LABORATORY
ATTN: TECHNICAL LIBRARY (SUL)
KIRTLAND AFB NM 87117

S

NASA

POSTMASTER: If Undeliverable (Section 158
Postal Manual) Do Not Return